Article:

Hirohata, Atsufumi orcid.org/0000-0001-9107-2330, Yamada, Keisuke, Nakatani, Yoshinobu et al. (4 more authors) (2020) Review on Spintronics:Principles and Device Applications. Journal of Magnetism and Magnetic Materials. ISSN: 0304-8853

https://doi.org/10.1016/j.jmmm.2020.166711

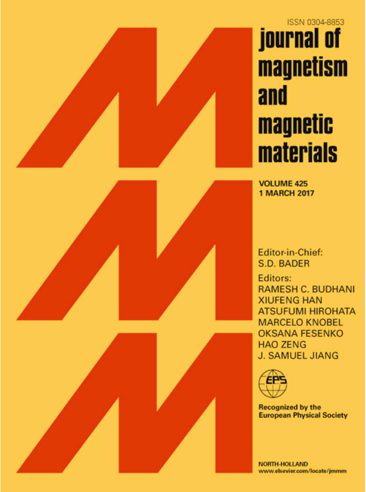

Review on Spintronics: Principles and Device Applications

Atsufumi Hirohata, Keisuke Yamada, Yoshinobu Nakatani, Lucian Prejbeanu, Bernard Diény, Philipp Pirro, Burkard Hillebrands

PII: S0304-8853(20)30235-3
DOI: https://doi.org/10.1016/j.jmmm.2020.166711
Reference: MAGMA 166711

To appear in: *Journal of Magnetism and Magnetic Materials*

Received Date: 28 January 2020
Revised Date: 4 March 2020
Accepted Date: 7 March 2020

Please cite this article as: A. Hirohata, K. Yamada, Y. Nakatani, L. Prejbeanu, B. Diény, P. Pirro, B. Hillebrands, Review on Spintronics: Principles and Device Applications, *Journal of Magnetism and Magnetic Materials* (2020), doi: https://doi.org/10.1016/j.jmmm.2020.166711

Review on Spintronics: Principles and Device Applications

Atsufumi Hirohata,[1)] Keisuke Yamada,[2)] Yoshinobu Nakatani,[3)] Lucian Prejbeanu,[4)] Bernard Diény,[4)] Philipp Pirro [5)] and Burkard Hillebrands [5)]

[1)] *Department of Electronic Engineering, University of York, York YO10 5DD, United Kingdom*
[2)] *Department of Chemistry and Biomolecular Science, Gifu University, Gifu 501-1112, Japan*
[3)] *Graduate School of Informatics and Engineering, University of Electro-Communications, Chofu 182-8585, Japan*
[4)] *Spintec, CEA, 17 rue des Martyrs, 38054 Grenoble Cedex 9, France*
[5)] *Fachbereich Physik and Landesforschungszentrum OPTIMAS, Technische Universität Kaiserslautern, 67663 Kaiserslautern, Germany*

Abstract

Spintronics is one of the emerging fields for the next-generation nanoelectronic devices to reduce their power consumption and to increase their memory and processing capabilities. Such devices utilise the spin degree of freedom of electrons and/or holes, which can also interact with their orbital moments. In these devices, the spin polarisation is controlled either by magnetic layers used as spin-polarisers or analysers or via spin-orbit coupling. Spin waves can also be used to carry spin current. In this review, the fundamental physics of these phenomena is described first with respect to the spin generation methods as detailed in Sections 2 ~ 9. The recent development in their device applications then follows in Sections 10 and 11. Future perspectives are provided at the end.

List of Abbreviations

1D	one-dimensional
2D	two-dimensional
2DEG	two-dimensional electron gas
3D	three-dimensional
AB	Aharonov-Bohm
AEE	anomalous Ettingshausen effect
AF	antiferromagnetic, antiferromagnet
Alq_3	tris(8-hydroxyquinolinato) aluminium
AMR	anisotropic magnetoresistance
ANE	anomalous Nernst effect
ARPES	angle-resolved photoemission spectroscopy
ASS	Altshuler-Aronov-Spivak
BLS	Brillouin light scattering
CIMS	current-induced magnetisation switching
CIP	current in the plane
CPP	current perpendicular to the plane
CuPc	copper phthalocyanine
DMI	Dzyaloshinskii-Moriya interaction
DMS	dilute magnetic semiconductor
DOS	density of states
DRAM	dynamic random access memory
DW	domain wall
EDL	electric double layer
EL	electroluminescence
F	fabrication rule
FET	field effect transistor
FM	ferromagnetic, ferromagnet
FMR	ferromagnetic resonance
GMR	giant magnetoresistance
HAMR	heat-assisted magnetic recording
HDD	hard disk drive
HM	heavy metal
HMF	half-metallic ferromagnet
LED	light emitting diode
LLG	Landau-Lifshitz-Gilbert
LSMO	$La_xSr_{1-x}MnO_3$
MAMR	microwave-assisted magnetic recording
MCD	magnetic circular dichroism
MO	magneto-optical
MOS	metal-oxide-semiconductor
MRAM	magnetic random access memory
MTJ	magnetic tunnel junction
MWCNT	multi-walled carbon nanotube
NM	non-magnetic, non-magnet
NOL	nano-oxide layers
p-MTJ	perpendicularly-magnetised magnetic tunnel junction
PSA	perpendicular shape anisotropy
Py	permalloy
QW	quantum well
RA	resistance-area product
ReRAM	resistive random access memory

RM	racetrack memory
RT	room temperature
SAW	surface acoustic wave
SC	semiconducting, semiconductor
SET	single electron transistor
SOT	spin-orbit-torque
SP-STM	spin-polarised scanning tunnelling microscopy
SQUID	superconducting quantum interference device
SRAM	static random access memory
SOT	spin-orbit torque
STO	spin-torque oscillator
STT	spin-transfer torque
TAMR	tunnelling anisotropic magnetoresistance
TI	topological insulator
TMR	tunnelling magnetoresistance
TR-MOKE	time-resolved magneto-optical Kerr effect
VCMA	voltage induced change of magnetic anisotropy
VCSEL	vertical cavity surface emitting laser
YIG	yttrium iron garnets

1. Introduction

For nano- and microscale devices and systems, the magnetics community has benefitted from the development of nanofabrication techniques in the semiconductor area, such as electron-beam lithography and Ar-ion milling. Even so, these two worlds have different advantages and disadvantages as listed in Fig. 1. As an example of magnetic devices and systems utilising a spin quantum number, a hard disk drive (HDD) has been invented by IBM in 1956, which currently has a global market revenue of approximately \$11bn in 2018 (376m units shipped in 2018) [1]. Another field of applications is the one of magnetic field sensors, with a market revenue of ~ \$19b in 2018 [2]. On the other hand, the field of semiconductor devices has a much larger market of ~ \$469b in 2018 [3] which has been originally proposed by Lilienfeld and demonstrated [4] by the invention of the transistor (transport resistor) by the Bell Laboratory in 1947 [5].

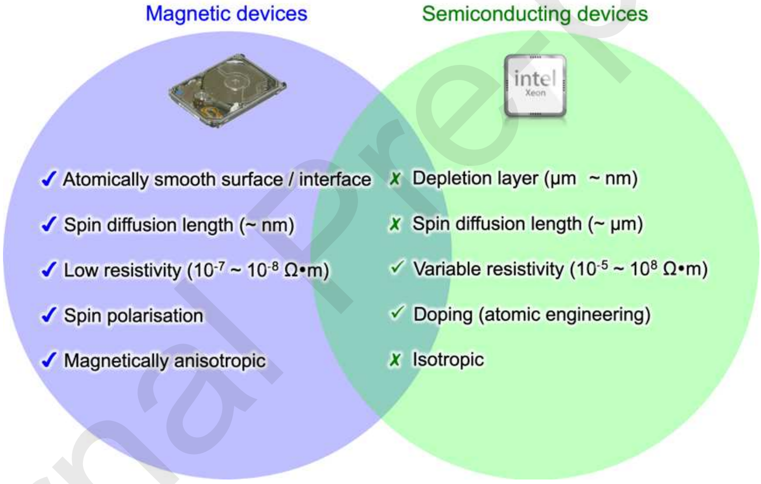

Fig. 1 Comparison between magnetic and semiconducting materials.

For magnetic devices and systems, their electron transport properties are strongly dependent on the atomic smoothness of their surfaces and interfaces, while for semiconducting devices and systems, their transport properties are controlled by a depletion layer, which can be intrinsically formed at their interfaces against a metallic layer with the thickness between a few nm (*e.g.*, InAs) and a few μm (*e.g.*, Si and GaAs) for moderate doping without a gate bias application. For a ferromagnetic (FM), non-magnetic (NM) and semiconducting (SC) material, spin diffusion lengths are typically ~ 5, ~ 300 and ~ 1,000 nm.

For electron transport, the magnetic materials have a low resistivity of the order of (10^{-7} ~ 10^{-8}) Ω·m, while semiconductors with moderate doping or undoped have a higher resistivity of the order of (10^{-5} ~ 10^{8}) Ω·m at room temperature (RT). The key parameters to characterise the device and system performance are spin polarisation and doping density. The spin polarisation determines the efficiency of the spin-polarised electron transport, while the doping density controls the resistivity and spin diffusion length. Spin-transport can also be achieved using magnons, the elementary quanta of spin waves [6],[7]. This can be realized using magnetic insulators, such as yttrium iron garnets (YIG), with lower losses than in metallic systems where electron current always generate Joule dissipation (see Section 5.3 for more details).

1.1. Magnetic length scale

The typical length scales of magnetic devices and systems are listed in Fig. 2. Spin polarisation is transferred either by conduction electrons in a conductor or spin-wave propagation across local magnetic moments in an insulator. In bulk magnets, the dipolar (demagnetising) field from the edges of the sample plays an important role, which quite frequently causes the breaking up of the magnetisation into domains [8]. The size d_{domain} of the domains can range between tens of nanometres and micrometres or even millimetres depending on the materials. These domains are separated by domain walls whose width results from a tradeoff between exchange energy (characterised by the stiffness constant: A) and anisotropy energy (characterised by anisotropy energy per unit volume). The domain wall width can range from tens of nanometres to microns. When the size of the system is sufficiently reduced, the exchange interaction plays a dominant role and results in a single-domain state. The whole magnetisation is then aligned along the global easy axis defined by the magnetic anisotropy, including the shape anisotropy. Magnetic distortions may still exist at the edges of the device on a length scale called the exchange length which results from the trade-off between exchange energy (A) and magnetostatic energy ($\mu_0 M_s^2$). This exchange length is typically of the order of a few nm in materials such as Co or NiFe. From electronic transport point of view, two main length scales exist: the elastic mean free path which is the distance over which an electron can travel without being scattered. This length is spin-dependent in magnetic material and can range from a fraction of nanometre to several tens of nanometres. Another important length is the spin diffusion length which is the distance over which an electron can keep the memory of its spin. This length can vary from a nanometre in material with high spin orbit to a few hundred of nanometres or even more in non-magnetic materials with weak spin orbit.

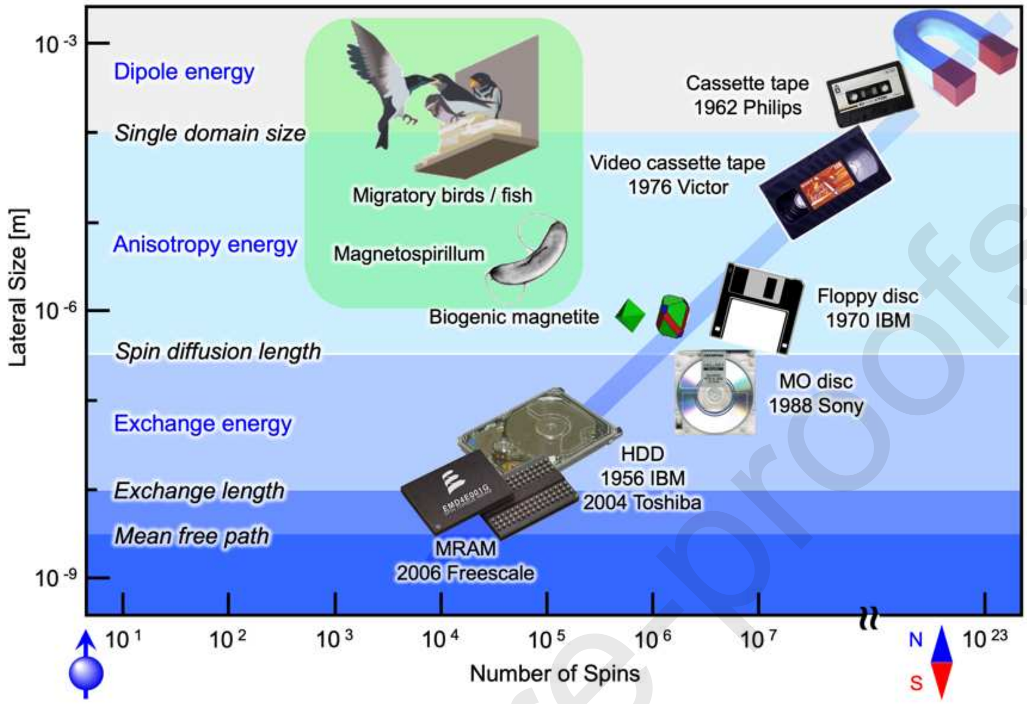

Fig. 2 Typical magnetic length scales and development of magnetic storage devices. After Ref. [9].

It is interesting to correlate these length scales with characteristic length scales encountered in the development of magnetic storage and non-volatile memory technology. Magnetic media from tapes to hard disk drives are made of granular ferromagnetic materials in which the grains are single domain and essentially uncoupled. The information (0 or 1) is written in the form of magnetic domains (the bits) magnetised in one direction or the opposite one along the easy axis of anisotropy. These domains involve bunch of tens or hundreds of grains. Increasing the areal storage density in these media has consisted in reducing the grain size from microns in audio tapes to a few nanometres in state-of-the-art hard disk drives. This required increasing the media magnetic anisotropy to maintain thermal stability of the magnetization of the individual grains. Magnetic random access memory (MRAM) is a solid state memory. They are made of patterned magnetic tunnel junctions. Each bit is an individual tunnel junction. The storage layer does not have then to be granular as in recording media. In state of the art MRAM, the storage layer of each magnetic tunnel junction (MTJ) has a typical thickness between 1.4 and 2nm and the MTJ is patterned in the form of a cylinder of diameter in the range 20 ~ 50 nm.

If the device considered lenthscale is smaller than the spin diffusion length, the electron spin is preserved. In the regime where the considered length scale is much smaller than the mean free path of the electrons (in mesoscopic systems), the electron momentum is also preserved during transport (ballistic regime). One of the ultimate goals of spintronics is to realise quantum functionalities using the long spin coherence length in a SC. For the first step, spin-polarised three-terminal devices, which eventually lead to a single electron transistor (SET) [10], providing fundamental data processing with a single electron, have also been widely studied.

1.2. Spin generation

Spin-polarised electrons can be generated in NM materials using the following methods [9]: spin injection from a FM, a magnetic field, an electric field, electromagnetic wave introduction, Zeeman splitting, spin motive force, a thermal gradient and mechanical rotation (see Fig. 3). One of the most common methods is spin injection from a FM material, *e.g.*, conventional FM metals (Fe, Co, Ni and Gd), half-metallic ferromagnets (HMF) and dilute magnetic semiconductors (DMS), attached to a NM metal or SC through an ohmic contact or a tunnel barrier. A stray field at the edge of a FM can also be used to induce a population difference in spin-polarised electrons in a NM material. Electromagnetic wave, *e.g.*, circularly polarised light and microwave, excites spin-polarised electrons in SC, dependent upon an optical selection rule. The reverse effect generates circularly polarised light emission by a spin-polarised electron current. This can be extended further to spin generation by electromagnetic waves, including spin pumping and high-frequency spin induction. In addition, a thermal gradient has been found to produce spin-polarised carrier flow due to the spin Seebeck and Nernst effects etc., which can be useful for energy harvesting.

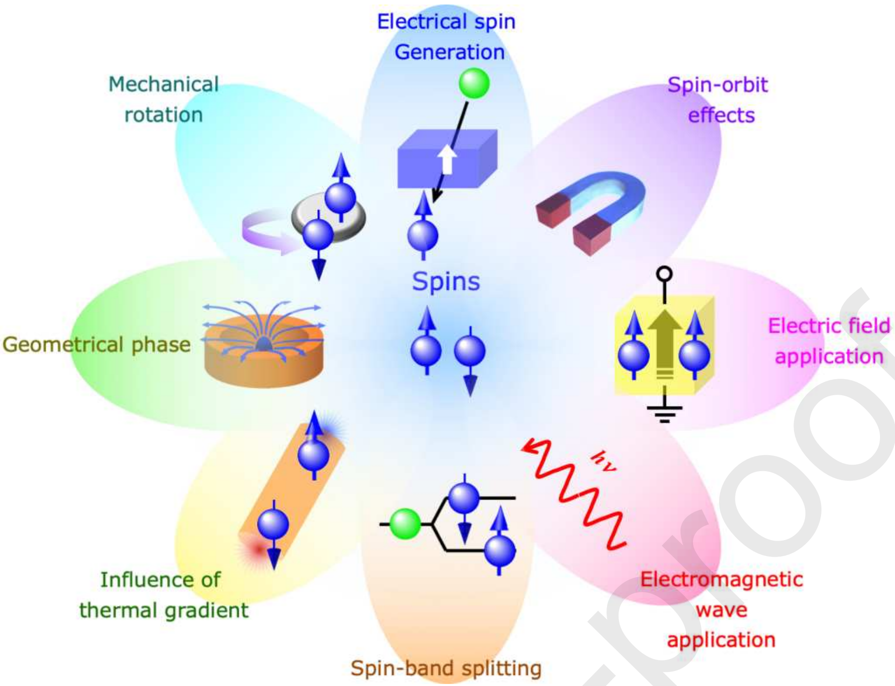

Fig. 3 Schematic diagram of major methods to generate a spin-polarised current. After Ref. [9].

In spintronics [9],[11], the spin-current generation efficiency is the most critical figure of merit for device applications [12]. The generation efficiency (η) can typically be defined as the generated spin current per unit energy introduced. For instance, when the spin current is produced from a charge current by spin Hall effect, a charge to spin current conversion efffencieny is defined by the ratio between the electron-spin-current density generated (j_s) divided by the electron-charge-current density introduced (j_c): $\eta = j_s / j_c$ [13]. Here, j_s is commonly deduced from a measured voltage and its magnitude is dependent upon the theoretical model exploited to interpret it. In some devices with a current flowing in the plane, *e.g.*, devices used for spin-orbit torque, spin-torque ferromagnetic resonance and spin Hall measurements, it is very difficult to measure j_s and is widely known that j_s is assumed using models, such as parallel conduction, leading to overestimation of η. As can be seen in Table 1, a series of spin-current generation methods without using systems including interfaces have much higher efficiency than those with interfaces, which is favourable for device applications. For example, an interface between a FM and a NM for spin generation by spin-orbit effects and electromagnetic wave applications is limited by their efficiency to be ~ 20% [17],[21] although η is expected to reach ~100% in a magnetic tunnel junction with coherent tunnelling across a MgO barrier in theory. Note that in Ref. [21], the efficiency is calculated as a ratio between the absorbed and introduced microwave power, which can provide an indicative efficiency. This is predominantly due to the interfacial spin scattering by the presence of defects and contaminations. By utilising a highly spin-polarised FM, such as a half-metallic Heusler alloy, the efficiency can be increased up to almost 30% to date [14]. However, scattering asymmetry can increase the effective spin polarisation in FM, *e.g.*, 94% reported at a Co/Ni interface [25]. Further increase in efficiency up to 100% using coherent tunnelling with a MgO barrier has been theoretically predicted [15],[16].

Table 1 List of spin-current generation efficiency using various methods. After Ref. [12].

Method	System	Efficiency (η)	Reference
Electrical spin generation	Lateral spin-valve: $Co_2FeSi/Cu/Co_2FeSi$	27%	[14]
	(Coherent tunnelling in a magnetic tunnel junction)	100% (theory)	[15],[16]
Spin-orbit effects	Spin Hall: $Pt_{0.85}Hf_{0.15}$ (5.5)/Pt (0.5)/Co (1) (nm)	(23 ± 2)%	[17]
	Topological insulator: $(Bi_{1-x}Sb_x)_2Te_3$ thin films	45 ~ 57% (max)	[18]
	Quantum spin Hall: HgTe/(Hg,Cd)Te	100%	[19]
Electric field application	(Interfacial band changes under a field)	N/A	[20]
Electromagnetic wave application	Spin pumping: $Y_3Fe_5O_{12}/Pt$	~ 20%	[21]
Spin-band splitting	(Intrinsic Zeeman splitting at low temperature)	N/A	[22]
Influence of thermal gradient	$Pt/Ni_{0.2}Zn_{0.3}Fe_{2.5}O_4$ film	10^{-3}%	[23]
Geometrical phase	(Geometrical phase introduced by a field)	100% (theory)	[24]
Mechanical rotation	(Electrical motor for mechanical rotation)	N/A	[11]

On the other hand, 100% generation efficiency of spin currents is predicted to occur in NM materials under certain conditions [23]. For example, a topological insulator is experimentally demonstrated to generate a spin current with η to be up to ~ 60% [18]. This is the maximum value reported to date but it is under debate [24]. A mechanically-induced spin current to be generated in a NM with a large spin-orbit coupling is also expected to have a high efficiency of up to 100% in theory [11], which is governed by the efficiency of the electrical motor to rotate an object [26]. It is therefore important to discuss the spin-current generation efficiency of each method in details. Some of the systems may be difficult to be realised experimentally but they may hold the key for the future design of spintronic applications. These developments in spintronic phenomena and devices are listed in Fig. 4.

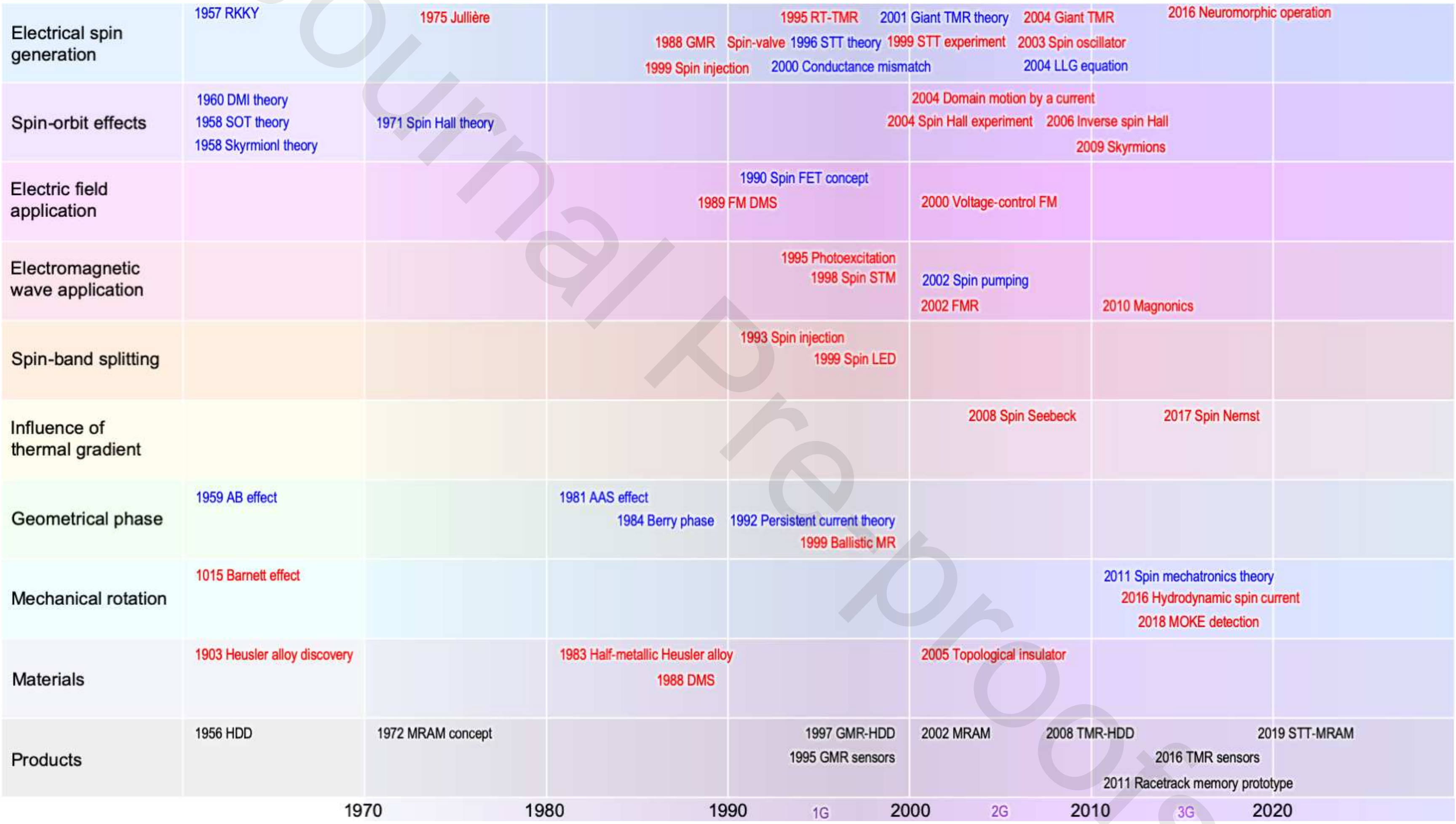
Electrical spin generation
1957 RKKY
1975 Jullière
1988 GMR
1999 Spin injection
1995 RT-TMR
Spin-valve
1996 STT theory
2000 Conductance mismatch
2001 Giant TMR theory
1999 STT experiment
2004 Giant TMR
2003 Spin oscillator
2004 LLG equation
2016 Neuromorphic operation
Spin-orbit effects
1960 DMI theory
1958 SOT theory
1958 Skyrmionl theory
1971 Spin Hall theory
2004 Domain motion by a current
2004 Spin Hall experiment
2006 Inverse spin Hall
2009 Skyrmions
Electric field application
1990 Spin FET concept
1989 FM DMS
2000 Voltage-control FM
Electromagnetic wave application
1995 Photoexcitation
1998 Spin STM
2002 Spin pumping
2002 FMR
2010 Magnonics
Spin-band splitting
1993 Spin injection
1999 Spin LED
Influence of thermal gradient
2008 Spin Seebeck
2017 Spin Nernst
Geometrical phase
1959 AB effect
1981 AAS effect
1984 Berry phase
1992 Persistent current theory
1999 Ballistic MR
Mechanical rotation
1015 Barnett effect
2011 Spin mechatronics theory
2016 Hydrodynamic spin current
2018 MOKE detection
Materials
1903 Heusler alloy discovery
1983 Half-metallic Heusler alloy
1988 DMS
2005 Topological insulator
Products
1956 HDD
1972 MRAM concept
1997 GMR-HDD
1995 GMR sensors
2002 MRAM
2008 TMR-HDD
2016 TMR sensors
2011 Racetrack memory prototype
2019 STT-MRAM
1970
1980
1990
1G
2000
2G
2010
3G
2020

Fig. 4 Historical development of spintronic phenomena and devices.

2. Electrical Spin Generation

Spin-polarised electrons (and/or holes) can be injected into a NM material by flowing an electrical current from a FM material. This is the most commonly used method for spin generation demonstrated by tunnelling magnetoresistance (TMR) in 1975 [27], giant magnetoresistance (GMR) in 1988 [28],[29] and Johnson transistor in 1993 [30], initiating the research on magnetotranport. The magnetotransport is categorised as the first generation of spintronics, which has been invented by abbreviating spin electronics in 2001 [31]. The injection efficiency depends on the spin polarisation of the FM and the spin scattering at the FM/NM interface. It is also important to eliminate any other effects, namely a stray field from a FM, which distorts the estimation of the injection efficiency.

2.1. Tunnelling magnetoresistance

Resistance changes associated with the magnetic configuration have been demonstrated in MTJ at low temperature as schematically shown in Fig. 5 [27]. TMR at RT has then be achieved by Miyazaki [32] and Moodera [33] independently. Since then, the TMR ratio has been improved very rapidly to 81% in a MTJ consisting of $Co_{0.4}Fe_{0.4}B_{0.2}$ (3)/Al (0.6)-Ox/$Co_{0.4}Fe_{0.4}B_{0.2}$ (2.5) (thickness in nm) at RT [34]. Here, the TMR ratio can be defined as [27]

$$\text{TMR ratio} = 2P_1P_2/(1-P_1P_2), \qquad (1)$$

where P_{FM1} and P_{FM2} are the spin polarisation of the FM1 and FM2 layers, respectively which are defined as:

$$P = \frac{N_{\text{majority}} - N_{\text{minority}}}{N_{\text{majority}} + N_{\text{minority}}}, \qquad (2)$$

By replacing amorphous AlO_x with epitaxial MgO, theoreticians have predicated over 1,000% TMR ratios due to coherent tunnelling at an Fe/MgO interface [15],[16]. The Fe/MgO (and CoFeB/MgO as later discovered) interface connects their Δ_1 bands smoothly but not the other bands, *e.g.*, Δ_2 and Δ_5. Since the Δ_1 bands are 100% spin polarised in Fe and CoFe alloys, this allows the electrons to tunnel through the MgO barrier with an almost half metallic character yielding the very high TMR amplitude observed in MgO-based MTJs. For the coherent tunnelling, $P_{1(2)}$ can be 100%, leading to the TMR ratio of infinity. Experimentally, giant TMR ratios have been reported by Parkin [35] and Yuasa [36] independently. Accordingly, a TMR ratio as large as 604% has been achieved in a MTJ consisting of $Co_{0.2}Fe_{0.6}B_{0.2}$ (6)/MgO (2.1)/$Co_{0.2}Fe_{0.6}B_{0.2}$ (4) (thickness in nm) at RT [37]. Such drastic increase in the TMR ratio has been implemented in spintronic devices quickly with increasing the areal density of HDD by almost four times over the last decade as well as recent development in Gbit-scale MRAM, for example (see Section 11.2 for more details).

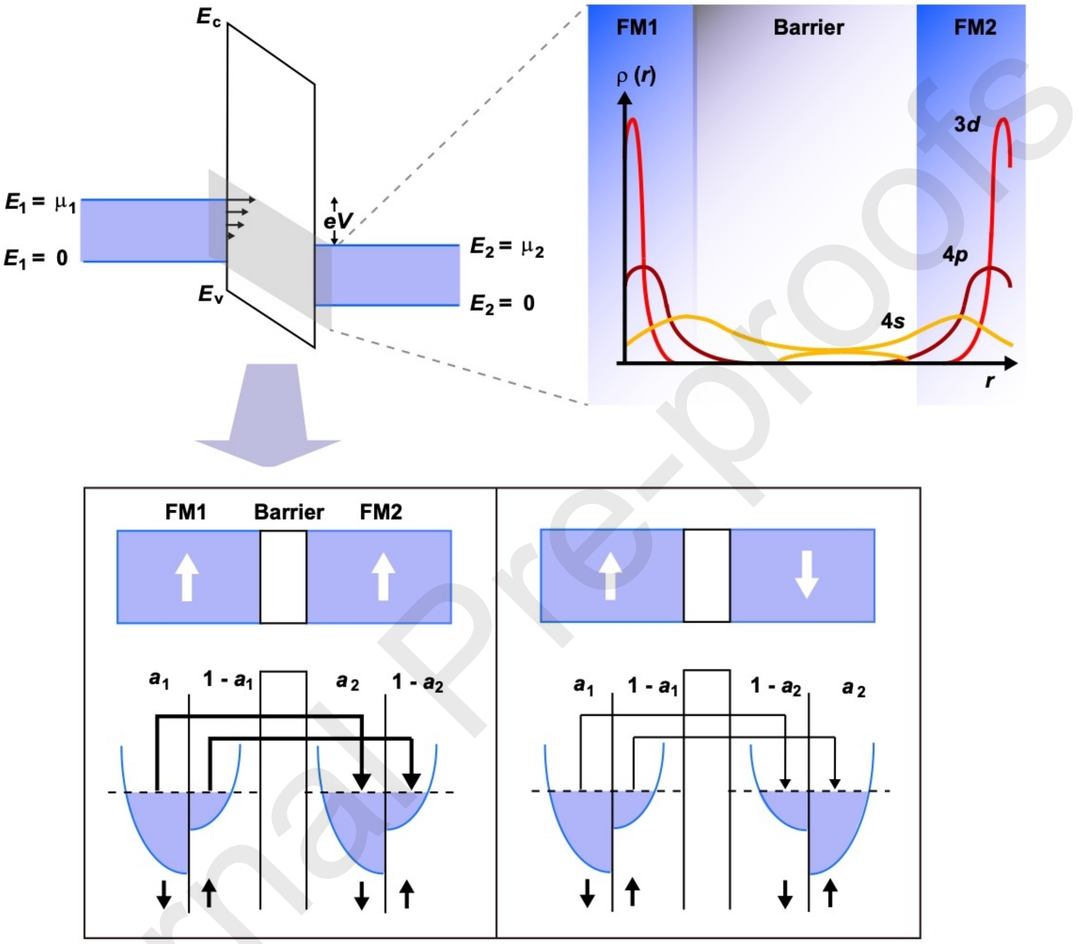

Fig. 5 Schematic diagram of spin-polarised electron tunnelling.

2.2. Giant magnetoresistance

Another key discovery in magnetotransport is the GMR of metallic magnetic multilayers by Fert [28] and Grünberg [29] independently. A $[\mathrm{Fe}\ (3)/\mathrm{Cr}\ (0.9)]_{60}$ (thickness in nm) structure shows a resistance change of 50% by the application of a magnetic field at 4.2K [28]. The GMR effect depends on spin-dependent scattering of electrons as discussed below. The critical measure of efficient magnetic transport in these devices is a MR ratio, which is defined by

$$\text{MR ratio} = \Delta R / R = (R_{\mathrm{AP}} - R_{\mathrm{P}}) / R_{\mathrm{P}}, \qquad (3)$$

where R_P and R_{AP} represent the resistance measured for parallel and antiparallel configurations of the FM magnetisations, respectively. Low field GMR sensors called spin-valves were introduced by IBM in 1998. The larger signal changes provided by these sensors as compared to the previously existing magnetoresistive sensors based on anisotropic magnetoresistance (AMR) allowed larger margin for reading out stored data in hard disk drives. Later, the GMR ratio has been increased up to be 65% at 300K in a [Co (0.8)/Cu (0.83)]$_{60}$ (thickness in nm) junction [38]. By replacing the FM with a half-metallic FM $Co_2FeGa_{0.5}Ge_{0.5}$, the maximum GMR ratio has been reported to be 82% at RT [39].

A voltage application gives rise to an electron flow in the direction opposite to the electric field either in the layer plane (CIP; current-in-plane) or perpendicular to the plane (CPP) geometry [40],[25]. It should be noted that the GMR effect depends on the FM thickness t_{FM} and NM interlayer thickness t_{NM}. In the CIP geometry, the critical length scales are given by the mean free paths, both in the FM layer where they are spin-dependent and in the interlayer material (typically ~ 20 nm in Cu). The CIP-GMR decreases rapidly as a function of t_{NM} due to both electron scattering reducing the electron flow traversing the spacer layer and due to current shunting in this layer. In the CPP geometry, the critical thickness is given by the spin diffusion length, which is around 100 nm ~ 1 μm for the NM interlayer materials [41].

Theoretically, the most commonly accepted model to explain the CPP-GMR behaviour is the Valet-Fert model [42]. Based on the two-current model, R_P and R_{AP} have the following relationship:

$$R_{\mathrm{P}} = R_{\mathrm{AP}} - \frac{\left[\beta \rho_{\mathrm{FM}}{}^{*} \left\{{}^{t}\mathrm{FM} / \left(t_{\mathrm{FM}} + t_{\mathrm{NM}}\right)\right\} L + 2\gamma r_{\mathrm{b}}{}^{*} n\right]^{2}}{R_{\mathrm{AP}}}, \tag{4}$$

where β is the bulk asymmetry coefficient defined as $\rho_{\uparrow(\downarrow)} = 2\rho_{\mathrm{FM}}{}^{*}[1 - (+)\beta]$. Here, $\rho_{\mathrm{FM}}{}^{*} = t_{\mathrm{FM}}(\rho_{\uparrow} + \rho_{\downarrow})/2$ is the effective resistance of both up (↑) and down (↓) spins, where t_{FM} is the thickness of a FM layer. For NM, the effective resistance can be determined as $\rho_{\uparrow(\downarrow)} = 2\rho_{\mathrm{NM}}{}^{*}$ and the thickness of a NM layer is t_{NM}. $L = n(t_{\mathrm{FM}} + t_{\mathrm{NM}})$ is the total thickness of a GMR multilayer with n time repeats. γ is the interfacial spin asymmetry coefficient determined as $r_{\uparrow(\downarrow)} = 2r_{\mathrm{b}}{}^{*}[1 - (+)\gamma]$, where $r_{\mathrm{b}}{}^{*}$ is the spin-dependent interfacial resistance per unit area. Therefore, the larger $\rho_{\mathrm{FM}}{}^{*}$, γ and $r_{\mathrm{b}}{}^{*}$ are required for the larger the CPP-GMR ratio.

2.3. Spin injection

The spin injection into a SC has been originally proposed to form a spin-polarised field effect transistor (spin FET) by Datta and Das [43]. The spin-polarised electrons are then demonstrated to be injected from the first FM (source) in NM Au and detected electrically by the second FM (drain) [30]. The drain can also be replaced with a quantum well (QW) to detect the injected spin-polarised electrons (and/or holes) as circularly-polarised electroluminescence (EL), *i.e.*, a spin-polarised light emitting diode (spin LED).

For efficient spin injection, the conductance matching at the FM/NM interfaces have been investigated by Schmidt *et al.* [44], identifying a fundamental obstacle to achieving efficient spin transmission across the interfaces via a diffusive process with spin-polarised electrons flowing in the vicinity of the Fermi level. Their calculations suggest that a few electrons with different spin polarisation from the majority spins at the Fermi level may reduce the spin polarisation in the semiconductor due to the conductance mismatch between them. Ideally 100% spin polarisation needs to be used for the source and drain to achieve highly efficient spin injection as described in Section 10.1.

Such an obstacle can be overcome by using either ballistic electrons [45] or very thin tunnelling barriers between the FM and the SC [46]. If the tunnel resistance is larger than the resistance in a SC or NM, which is much larger than that in a FM, spin injection with up to 100% efficiency can be achieved.

2.3.1. Spin-polarised transistor

As originally proposed by Datta and Das [43], a two dimensional electron gas (2DEG) in a SC has been widely exploited as a possible medium for spin-polarised electron transport due to its high in-plane mobility. Using InAs with almost negligible depletion layer thickness formed at the interfaces and edges, successful spin injection has been demonstrated with almost 1% change at 75K [47]. To exclude a Hall voltage induced by a strong magnetic field, a multi-terminal geometry has been proposed [48] and used [49] but without success. The magnetic-field-induced spin generation (see Section 3) can also be avoided by patterning into an asymmetric multi-terminal geometry.

Using GaAs, detailed spin transport in *n*-GaAs has been investigated by focused cross-sectional Kerr imaging [50]. The image in Ref. [50] verifies the exponential decay of spin-polarised electrons injected from a $Co_{0.68}Fe_{0.32}$ electrode, which agrees with the spin relaxation in GaAs. Theoretical calculations reveal that the Fe/GaAs(001) as well as Fe/ZnSe(001) interfaces can achieve coherent tunnelling with a spin polarisation of 99% [51]. Crooker *et al.* measured the spin polarisation of 32% at an Fe/GaAs Schottky junction [52]. In Fe/GaAs/Fe junctions, more up spin electrons can be injected on one side and more down spins can be ejected from the other end by flowing current across the junction. This indicates that positive spin polarisation is achieved in reversed bias, while negative polarisation is achieved in forward bias. Experimentally, however, the reversal of spin-polarisation has been reported with respect to the applied bias, which can be caused by spin transport through an interfacial resonant state [53]. An abrupt Fe/GaAs interface is the only way to avoid such reversal. Fleet *et al.* have succeeded to grow epitaxially abrupt Fe/GaAs(001) interface by cold deposition at ~ 173K, confirming reproducible spin-polarised current injection without bias-dependent reversal [54]. This may be very promising systems for future spin-injection devices.

2.3.2. Spin-polarised light emission

A FM/SC Schottky diode, consisting of an Fe (20 nm)/GaAs/InGaAs QW LED structure, has been used to measure circularly-polarised EL [55]. Spin injection from the Fe to the GaAs is achieved with an efficiency of about 2% at 25K but the right and left circularly polarised EL intensity does not show a clear difference. Later, Hanbicki *et al.* have performed a similar experiment with an Fe (12.5 nm)/AlGaAs/GaAs QW LED and have observed a spin injection efficiency of 30% [56]. They clearly observed a significant difference between the right and left circular EL intensity. The spin polarisation is estimated to be 13% at 4.5K (8% at 240K). Taking the spin relaxation time in the QW into account, they reported a small temperature dependence in the spin injection efficiency, which is consistent with spin-polarised electron tunnelling theory. Successful spin injection from epitaxial Fe into *n*-GaAs(001) has been demonstrated by detecting circularly-polarised EL at 4K [57].

Jonker's group in the Naval Research Laboratory has then inserted a tunnelling barrier at the FM/SC interface to achieve ballistic spin injection. Spin polarisation of 30% at 4.5K has been measured in an Fe/Al_2O_3/GaAs system [58]. By using coherent tunnelling with an epitaxial MgO(001) barrier, spin polarisation of 55% has been achieved [59]. This leads a spin injection efficiency of 32% at 290K [60]. However, atomic mixing across the MgO barrier during the annealing required to crystallise the barrier needs to be prevented.

As an indirect bandgap SC, poor spin injection has been expected for Si [61]. It has also long been believed that intrinsic spin polarisation in Si is typically a few percent at RT and hence spin injection into Si is very difficult. However, nanoelectronic devices predominantly depend on Si-based technology, requiring spin injection into Si with high efficiency. A junction of Co/Al_2O_3/Si has been used to demonstrate that the resistance-area product (*RA*) product can be tuned over eight orders of magnitude for the conductance matching by inserting an ultrathin Gd layer, which has a lower work function against Si [62]. Such tunability in the *RA* product is very useful to realise a spin metal-oxide-semiconductor (MOS) FET, which requires a narrow *RA* window against the Si doping density. Recently, spin injection into Si has been successfully demonstrated by Jonker *et al.* in an Fe/Al_2O_3/*n*-Si with an LED structure underneath [63]. Circular light polarisation of 5.6% has been reported at 20K (2.8% at 125K), indicating an injected spin polarisation of approximately 30% in Si. This experiment has opened a door to Si spintronics, which possesses a significant advantage for implementation of spintronics into current Si-based nano-electronics, *e.g.*, spin-polarised MOSFET. Recently, a microwave-induced spin current has been reported to be introduced in *p*-Si through $Ni_{0.8}Fe_{0.2}$, demonstrating a spin diffusion length of 150 nm [64].

2.3.3. Lateral spin-valve

A pioneering work on spin injection into a NM metal has been carried out by Johnson [30], followed by many studies without success. In 2000, Jedema *et al.* re-energised spin-injection studies by using a non-local geometry (see Fig. 6) [65]. They have successfully demonstrated diffusive spin injection from a FM $Ni_{0.8}Fe_{0.2}$ nanowire electrode, spin accumulation in a NM Cu nanowire and spin detection by another NiFe nano-electrode. Spin polarisation of the injected current is measured to be a few % and the corresponding spin diffusion length in Cu is estimated to be 350 nm at RT. They have further extended their study onto ballistic spin injection by inserting an Al-O tunnelling barrier at the FM/NM interface with increasing the spin signals [66].

A spin current $\vec{\boldsymbol{J}}_{\mathrm{s}}$ and a charge current $\vec{\boldsymbol{J}}_{\mathrm{c}}$ can be expressed as

$$\vec{\boldsymbol{J}}_{\mathrm{s}} = -\frac{\hbar}{2e}\left(\vec{\boldsymbol{j}}_{\uparrow} - \vec{\boldsymbol{j}}_{\downarrow}\right), \tag{5}$$

$$\vec{\boldsymbol{J}}_{\mathrm{c}} = \vec{\boldsymbol{j}}_{\uparrow} + \vec{\boldsymbol{j}}_{\downarrow}. \tag{6}$$

These currents follow the diffusion equation. For the spin current, the spin diffusion equation is written as

$$\nabla^2(\mu_\uparrow - \mu_\downarrow) = \frac{1}{D\tau_{\mathrm{sf}}}(\mu_\uparrow - \mu_\downarrow) \equiv \frac{1}{\lambda^2}(\mu_\uparrow - \mu_\downarrow), \tag{7}$$

where λ is the spin diffusion length (= $\sqrt{D\tau_{\mathrm{sf}}}$) and τ_{sf} is the spin flip time.

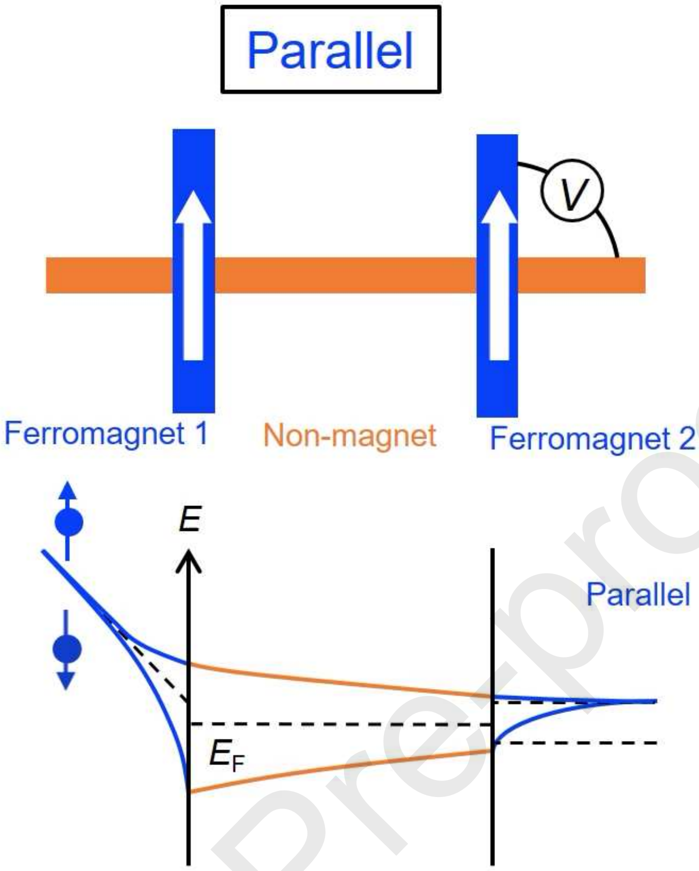

Fig. 6 Schematic movie of a lateral spin-valve with pure spin and charge currents (animation).

Non-local spin-valve systems have been extensively employed to investigate efficient spin injection by minimising interfacial scattering in both diffusive [67] and ballistic contacts [68], and also by optimising the junction area [69]. A 185 nm wide Ag nanowire has been employed to increase the spin-valve signals due to its longer spin diffusion length [70]. For the 300 nm separation between two FM wires (NiFe), ΔR as large as 8.2 mΩ at 79K has been reported. In these devices, the junction resistance is a key parameter to control interfacial spin polarisation. Later, 24% spin polarisation at a NiFe/Ag interface at 79K and 25% at a Co/Au interface at 4K are the best values achieved. By replacing FM with a half-metallic FM, Co_2FeSi, the largest injection efficiency of 27% has been reported at RT [71]. This is still only the half of the expected value from FM spin polarisation.

2.3.4. Organic junction

Spin-current injection into organic (namely carbon-based) matrerials is called as organic (carbon-based) spintronics, which has been attracting intensive studies recently. One of the pioneering works has demonstrated successful spin-current injection into a multi-walled carbon nanotube (MWCNT) using ferromagnetic Co electrodes by achieving 9% MR at 4.2K [72]. Highly spin-polarised currents have then been injected into the MWCNTs using $La_{0.7}Sr_{0.3}MnO_3$ electrodes [73]. A large GMR ratio of up to 61% is observed and the spin diffusion length of a MWCNT is estimated to be ~ 50 μm at 5K. In parallel, spin injection into graphene has also been demonstrated at RT in a non-local spin-valve structure [74]. In order to improve the spin injection efficiency into graphene, a high quality Al_2O_3 tunnelling barrier has been introduced on the epitaxial graphene grown on SiC in the local spin-valve [75]. The corresponding GMR ratio is reported to be 9.4% at 1.4K and the spin diffusion length is found to be over 100 μm, confirming the strong advantage of such carbon-based media as a spin-polarised electron career for device applications.

Vertical spin-valve devices have also been investigated intensively. By employing organic molecule tris(8-hydroxyquinolinato) aluminium (Alq_3) as the non-metallic spacer sandwiched between $La_xSr_{1-x}MnO_3$ (LSMO) and Co electrodes, the GMR ratio of 40% has been achieved at 11K [76]. By using an interface consisting of ferromagnetic cobalt and an organic semiconductor of copper phthalocyanine (CuPc), a very highly efficient spin injection has been demonstrated at RT, showing the spin injection efficiency of (85 ~ 90)% [77].

2.4. Spin-transfer torque

2.4.1. Landau-Lifshitz-Gilbert equation

The dynamics of the magnetisation $\vec{\boldsymbol{M}}$ upon application of an external field H_{eff} can be phenomenologically described by the Landau-Lifshitz-Gilbert (LLG) equation [78],[79]:

$$\frac{d\vec{\boldsymbol{M}}}{dt} = -\gamma\vec{\boldsymbol{M}} \times \vec{\boldsymbol{H}}_{\mathrm{eff}} + \frac{\alpha}{M}\vec{\boldsymbol{M}} \times \frac{d\vec{\boldsymbol{M}}}{dt}. \tag{8}$$

Here, the second term is the relaxation term with the Gilbert damping constant α. It describes essentially the coupling of the magnetisation precession to eventually the phonon bath, *i.e.*, how the magnetic excitation energy is transfered to the lattice. The relaxation term increases with increasing temperature as described by the *s-d* scattering model [80]. Here, conduction electrons (*s*) are scattered by localised spins (*d*) during the spin relaxation process, releasing the corresponding momentum into the lattice via the spin-orbit interaction at high temperature. This results in the spin relaxation, *i.e.*, α, to be proportional to the resistivity of the system ρ (resistivity like). At low temperature, on the other hand, α is proportional to the conductivity of the system σ (conductivity like).

The spin relaxation time τ can be approximated as

$\frac{1}{\tau} \sim \omega^2 \tau_p$ (D'yakonov-Perel model for large electron scattering probabilities [81]) or

$$\frac{1}{\tau} \propto \frac{1}{\tau_p} \text{ (Elliott-Yaffet model for strong spin-orbit interactions [82],[83]),} \tag{9}$$

where ω is the Lamor frequency and τ_p is the momentum relaxation time of an electron. To descrive the conductivity-like damping at low temperature, the breathing Fermi surface model has been proposed [84],[85],[86].

The spin-transfer torque (STT) can be described as $\frac{\gamma}{d}\boldsymbol{m} \times \left(\boldsymbol{m} \times \Delta\vec{\boldsymbol{J}}_{\mathrm{s}}\right)$ ($\vec{\boldsymbol{m}}$: the unit vector of the magnetisation) [87],[88]. By adding this term to the LLG equation, the magnetisation dynamics can be explained using the Landau-Lifshitz-Gilbert-Slonczewski equation Eq. (8):

$$\frac{d\vec{\boldsymbol{M}}}{dt} = -\gamma\vec{\boldsymbol{m}} \times \vec{\boldsymbol{H}}_{\mathrm{eff}} + \alpha\vec{\boldsymbol{m}} \times \frac{d\vec{\boldsymbol{m}}}{dt} - \frac{\gamma}{d}\vec{\boldsymbol{m}} \times \left(\vec{\boldsymbol{m}} \times \Delta\vec{\boldsymbol{J}}_{\mathrm{s}}\right). \tag{10}$$

For a particular direction of the spin current, STT is antiparallel to the Gilbert damping torque. Here, the Gauss law ($\frac{1}{\gamma}\frac{\partial}{\partial t}\vec{\boldsymbol{m}} \cdot V = -\int \vec{\boldsymbol{J}}_{\mathrm{s}} dS = -\Delta\vec{\boldsymbol{J}}_{\mathrm{s}}$, $V = S \cdot d$: volume of a FM layer with area S and thickness d) is applied to convert the second term. This equation indicates that the increase in the spin current $\vec{\boldsymbol{J}}_{\mathrm{s}}$ reduces the relaxation, leading to the precessional motion of magnetization yielding magnetisation switching or steady-state spin-torque oscillation. Equation (10) is used to simulate the motion of DW and skyrmions as presented in Figs. 7 and 18, respectively (see the detailed implementation as detailed in Ref. [89]).

Under the presence of STT, a shift in precession frequency occurs similar to the Doppler effect (spin Doppler effect). The shift of spin wave propagation in a NiFe wire under STT has been demonstrated at RT as the spin Doppler effect [90].

2.4.2. Giant magnetoresistive nanopillar

In a GMR junction, the effect of STT effect can be induced in FM1/NM/FM2 type of structures by flowing a CPP electrical current through it [87],[88]. Conduction electrons are spin-polarised by flowing through FM1 and exert a torque on the “localised” electrons, such as 3*d* electrons for transition metals, in FM2 after having traversed the NM spacer. This induces rotation of the spins of the “local” electrons in FM2. In a nanoscale junction, such STT can reverse the magnetisation of FM2 by flowing a current above a threshold (critical current density, j_{c}), which is typically of the order below 10^7 A/cm^2. The STT effect has first been demonstrated in a point contact [91] and later in CPP-GMR [92] and TMR nanopillars, which offer a key building block for the development of MRAM. Using a CPP-GMR nanopillar, an effective STT has been realised by combining two techniques, precise nanofabrication and atomically controlled film growth. A substantial decrease in j_{c} for current-induced magnetisation switching (CIMS) has been achieved in a CPP pseudo-spin-valve nanopillar by inserting a spin-scattering Ru ultrathin layer [93] and an additional FM layer [94]. This is an improved structure compared with a simple pseudo-spin-valve with a spin-scattering layer and has successfully achieved j_c of 2×10^6 A/cm^2. Further reduction in the critical current density has been achieved by modifying the shape of the nanopillar into a nanoring, where the magnetisation in each FM layer forms a vortex state at remanence for example [95]. These magnetisation directions are aligned to be either clockwise or anti-clockwise by carefully demagnetising the nanopillar, so that a vertical current assists CIMS by introducing an Ampère field without minor magnetic-moment curling or domains, *i.e.*, no stray field.

For further increase in CPP-GMR ratios, a spin-valve transistor has been developed by Monsma *et al.* in 1996 [96]. The spin-valve transistor utilises the difference in a magneto-current passing through a spin-valve in its hot-electron regime, which is typically < 1 eV above the Fermi energy. In their initial proposal, insulating MgO is inserted between an emitter electrode for spin injection and a base electrode to induce perpendicular magnetic anisotropy in the spin-valve, achieving the magneto-current chages of 85% at 60K [97].

2.4.3. Magnetic Tunnel junction nanopillar

A TMR nanopillar with an Al-O barrier has then been employed for CIMS showing a TMR ratio of ~ 30% and $J_c \leq 10^7$ A/cm^2 [98]. After the discovery of coherent tunnelling across an epitaxial MgO barrier, improved operation of a TMR nanopillar has been demonstrated with a TMR ratio of ~ 100% and $J_c \sim 6 \times 10^6$ A/cm^2 with a pulsed current of 100 ms duration [99]. This has been followed by a further improvement with a TMR ratio of 160% and J_c of 2.5×10^6 A/cm^2 [100].

In order to improve the downsize scalability of ultrasmall out-of-plane magnetized MTJs for STT-MRAM cells, it was proposed to increase the effective anisotropy by benefiting from an out-of-plane magnetic shape anisotropy [101],[102]. This is made possible by a significant increase in the FM thickness. The anisotropy stability factor Δ (= E / $k_B T$) is then enhanced thanks to the combined influence of the interfacial anisotropy at the magnetic electrode/MgO interface [103],[104] and of the vertical shape anisotropy. Concerning the TMR amplitude, the TMR ratio depends on the spin-dependent band configurations along the interface with the tunnel barrier. It can be modified by forming a QW formed at the interface between FM and tunnelling barrier layers. This can be achieved by the insertion of a very thin metallic Cr layer in the vicinity of the interface with realising a symmetric band configuration [105]. Recently, a resonant tunnelling junction through the QW state has been proposed by forming a double tunnelling barrier made of MgAlOx, *i.e.*, double MTJ, and has demonstrated the corresponding TMR oscillation for the FM layer thickness up to 12 nm [106]. A double MTJ including double QW has also shown quantum resonant tunnelling up to the FM thickness of 10 nm [107].

2.4.4. Ferromagnetic nanowire

By utilising the STT effect, magnetic moments in a domain can also be rotated by flowing an electrical current through DW. This can lead to the displacement of the magnetic DW in a micro- or nanoscale FM wires [108]. This offers the basis for a new magnetic solid-state storage device type, *i.e.*, the racetrack memory.

In 1970, DW motion by a magnetic field was studied for the development of the magnetic bubble memory [see Fig. 7(a)]. The DW motion velocity is proportional to the external magnetic field for the weak field case. However, for the strong field case, the averaged velocity decreases due to the change of the DW motion direction with time (Walker's breakdown). When Walker's breakdown occurs, the magnetisation rotates continuously and the direction of the magnetisation at the wall centre switches continuously. The critical field for the Walker breakdown (Walker's field H_W) can be defined as [109]

$$H_w = 2\pi M_S \alpha \tag{11}$$

Here, M_S is the saturation magnetisation and α is the Gilbert damping constant.

For the current induced case, the DW motion mechanism changes by the β term introduced by Thiaville *et al.* [89] and given by $\beta = \left(\lambda_J/\lambda_{sf}\right)^2 = \hbar/J \cdot \tau_{sf}$, with J: the *s-d* exchange interaction energy, τ_{sf}: the spin-flip time, λ_J and λ_{sf}: the associated diffusion lengths [see Fig. 7(b)]. For β = 0, the DW motion does not occur below a certain current threshold. In all cases, the DW is pinned by heterogeneity of the sample, the speed of the DW motion can be categorised into three regimes; creep, depinning and flow, as schematically shown in Fig. 7(c). A critical current J_c (or a field) is required for the DW displacement, depinning. DW then moves steadily. J_c is typically at the order of 10^{12} A/cm^2.

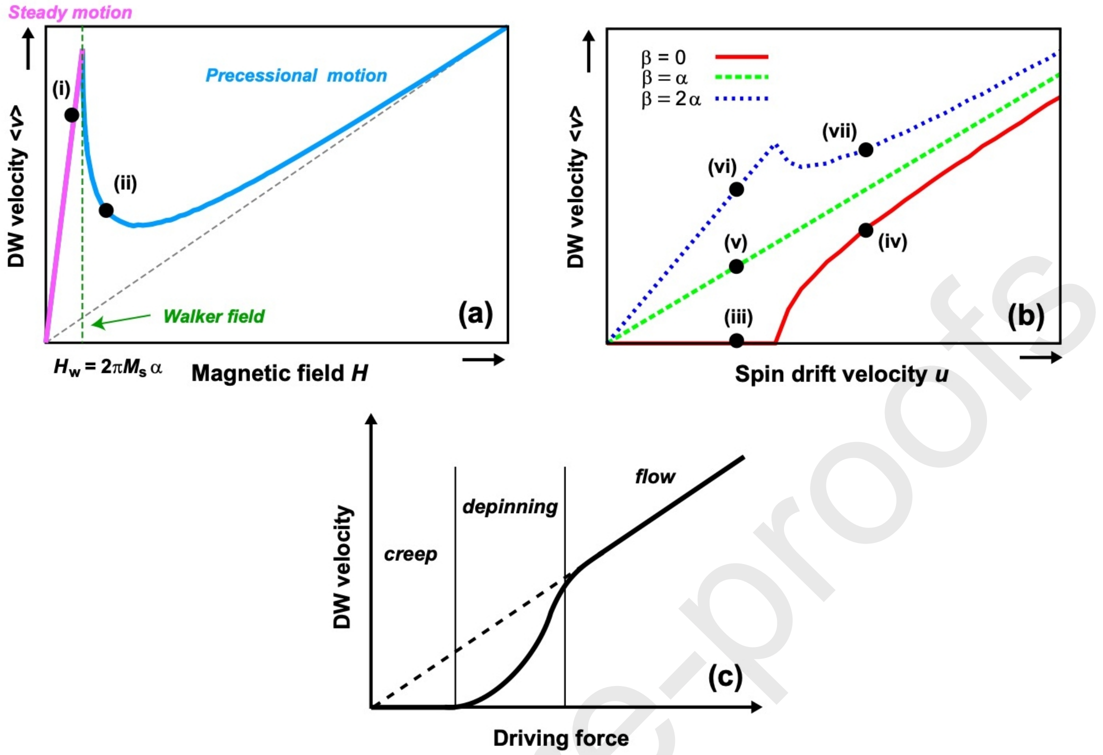
Steady motion
DW velocity <v>
(i)
(ii)
Precessional motion
Walker field
(a)
$H_w = 2\pi M_s \alpha$
Magnetic field H
DW velocity <v>
β = 0
β = α
β = 2α
(vii)
(vi)
(v)
(iv)
(iii)
(b)
Spin drift velocity u
DW velocity
creep
depinning
flow
(c)
Driving force

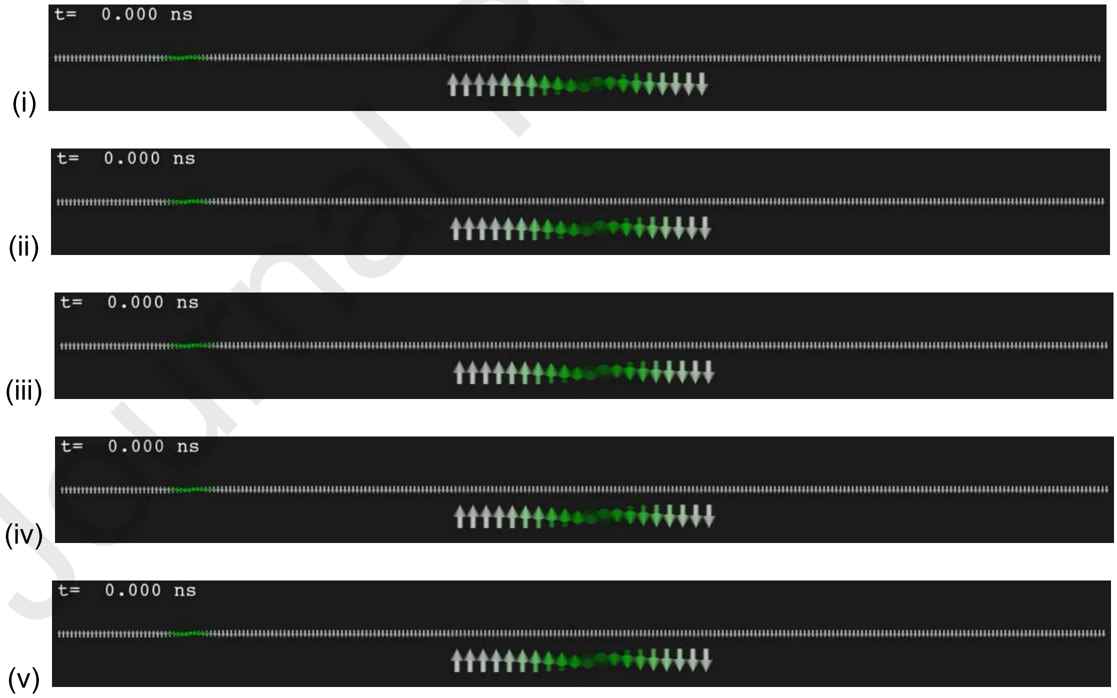
t= 0.000 ns
(i)
t= 0.000 ns
(ii)
t= 0.000 ns
(iii)
t= 0.000 ns
(iv)
t= 0.000 ns
(v)

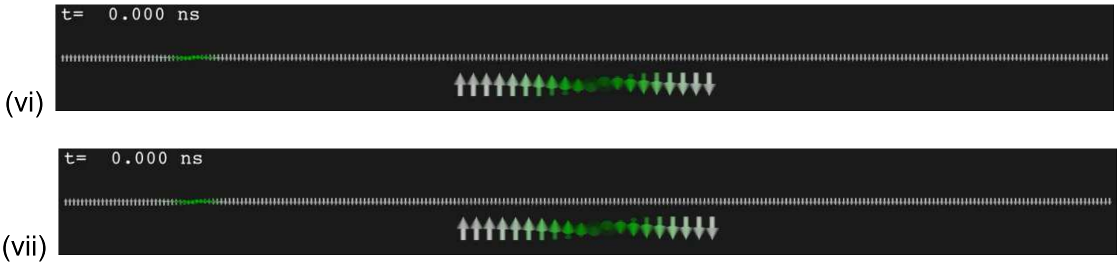

Fig. 7 DW can be moved by application of either an electrical current or a magnetic field (after Refs. [110],[111]). (a) DW motion applied by the magnetic field. (b) The DW motion induced by an applied current for various values of β. (c) Three regimes of DW motions applied by driving foce, *i.e.*, a magnetic field and/or spin-polarised current.

(i) DW moves while maintaining its structure: steady-state motion. (ii) The magnetisation rotation occurs continuously in the entire DW: precessional motion. (iii) The DW motion is stopped in time for (iii, iv) β = 0, (v) β = α, (vi, vii) β = 2α. The DW motions at (iv, vii) and (v, vi) are the precessional and the steady motion, respectively. The corresponding animations are shown for the cases (i) ~ (vii).

3. Spin-Orbit Effects

3.1. Spin Hall effects

Non-local spin-valves have also been used to detect both spin Hall and inverse spin Hall effects via the spin-orbit interactions as detailed in Section 3.2, showing the advantages of the lateral device configuration. A charge current in a paramagnetic metal has been predicted to induce a transverse spin imbalance without the application of a magnetic field, resulting in the spin Hall effect [112],[113]. On the contrary, a spin current can also induce a spin Hall voltage without a charge current or a magnetic field, *i.e.*, the inverse spin Hall effect. This is theoretically equivalent to anomalous Hall effect in a FM material and originates from the spin-orbit scattering of conduction electrons through skew and side-jump scattering.

A spin Hall effect has first been measured in InSb [114] and Ge [115] at low temperature. RT observation has been demonstrated at the edges of a GaAs semiconductor channel by magneto-optical Kerr imaging [116]. The spin Hall effect has then been detected in a metallic lateral spin-valve [117]. Here, a spin current is injected into a 60 nm wide Al wire from a 250 nm wide $Co_{0.80}Fe_{0.20}$ wire by the non-local method. The spin Hall voltage is then measured at the other end of the Al wire. By employing a perpendicularly magnetised FePt and a Au Hall bar, both spin Hall and inverse spin Hall effects as large as 2.9 mΩ have been detailed at RT for a separation between the injector and detector of 70 nm [118]. Such a large signal is very useful for the generation and detection of spin polarisation in a NM material. The spin-injection Hall effect, which is a transverse voltage response to the local spin polarisation of injected charge carriers, has also been reported in a 2DEG photovoltaic cell of GaAs/AlGaAs/GaAs [119]. The spin-dependent photovoltaic effect resulting from this effect has been found to convert the degree of circular polarisation of light directly to a voltage signal. These effects are summarised in Fig. 8.

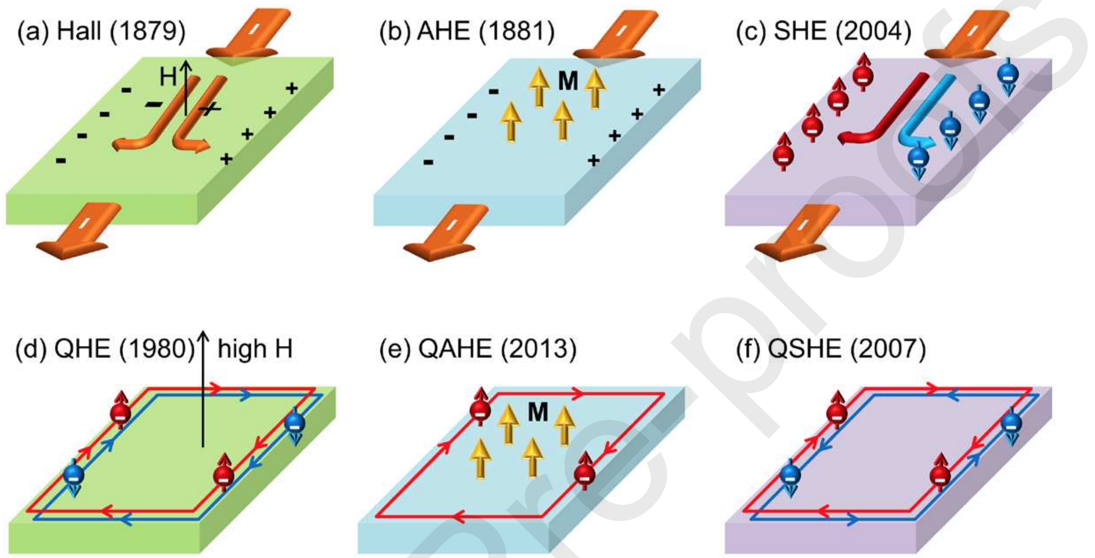

Fig. 8 Schematic diagrams of Hall effects, (a) conventional Hall effect, (b) anomalous Hall effect (AHE), (c) spin Hall effect (SHE), (d) quantum Hall effect (QHE), (e) quantum anomalous Hall effect (QAHE) and (f) quantum spin Hall effect (QSHE) [120].

An anomalous Hall effect can be induced by replacing a magnetic field with the intrinsic magnetisation in a FM. Unlike the conventional Hall effect caused by the Lorentz force, the anomalous Hall effect is also caused by the spin-orbit interactions. The intrinsic anomalous Hall effect occurs by impurity scattering without any angle or shift changes. The extrinsic anomalous Hall effect occurs by either skew scattering at a finite angle for low impurity concentration or side jump with a finite shift by high impurity concentration. The macroscopic scattering angle can be measured as the spin Hall angle θ_{SH}. Further increase in the impurity modifies the band structure, leading to hopping conduction [120].

In a two-dimensional insulator, the Hall conductance can be quantised as a multiple of e^2/h, quantum anomalous Hall effect. This has been reported in Cr-doped Bi_2Se_3 [121]. In the quantum anisotropic Hall effect, a huge MR exceeding 2,000% at 30mK can be observed at the chaege neutral point.

3.2. Spin-orbit torque

The spin-orbit interaction can be determined as

$$H_{\mathrm{SOI}} = \eta_{\mathrm{SO}} \vec{\boldsymbol{s}} \cdot \vec{\boldsymbol{L}}, \tag{12}$$

where η_{SO} is the spin-orbit interaction constant, $\vec{\boldsymbol{s}}$ and $\vec{\boldsymbol{L}}$ are the spin and orbital moments. η_{SO} is determined as

$$\eta_{\mathrm{SO}} = -(g-1)\frac{q\hbar^2}{2m^2c^2}\left(\frac{1}{r}\frac{d\phi(r)}{dr}\right). \tag{13}$$

Here, g is the Lande *g*-factor, q is the electron charge, $\hbar$ is the Planck constant divided by 2π, *m* is the electron mass, *c* is the speed of light, $\phi(r)$ is the scalar potential.

Spin-orbit interactions play an important role in SC as detailed below in Sections 11.7 and 11.8. In a spin Hall device, three configurations can be achieved as shown in Fig. 9. The spin-orbit torque is induced through the spin-orbit interaction in FM/heavy metal (HM) bilayers by flowing an in-plane electrical current. The magnitude of the induced torque can be evaluated by the switching current required for CIMS, J_c. For the perpendicular magnetisation, J_c is estimated to be (2.0 ± 0.1) × 10^{10} A/m with the θ_{SH} of (– 0.25 ± 0.02). For the in-plane magnetisation perpendicular to the electrical current direction, J_c is reduced to 1.0 × 10^{10} A/m with the θ_{SH} of – 0.08, while for the in-plane magnetisation parallel to the current, J_c is also reduced to (4.3 ± 0.2) × 10^{10} A/m with the θ_{SH} of (– 0.22 ± 0.01). As shown in Fig. 9(c), the last case has the fast damping process.

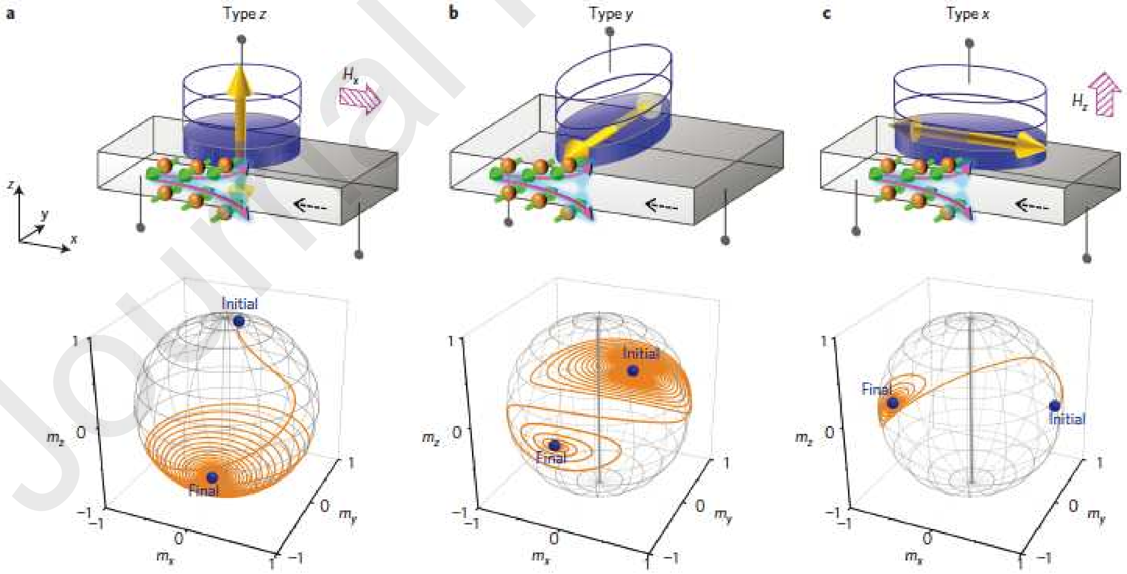

Fig. 9 Spin Hall effects depending on three different configurations, (a) perpendicular magnetisation and in-plane magnetisations with an electrical current (b) perpendicular and (c) along the magnetisation [122].

3.3. Antiferromagnetic/ferrimagnetic spintronics

3.3.1. Tunnelling anisotropic magnetoresistance

For a junction consisting of a FM/tunnelling barrier/NM, the resistance can be controlled by magnetisation rotation through the spin-orbit interaction at the interface, which is called tunnelling anisotropic magnetoresistance (TAMR). This effect has first been demonstrated experimentally by Gould *et al.* with a junction of $Ga_{0.94}Mn_{0.06}As$ (70)/AlOx (1.4)/Ti (5)/Au (300) (thickness in nm) [123]. A TAMR ratio of ~ 0.4% has also been measured with GaAs as a tunnel barrier [124]. Further increase in TAMR to 13% has been reported for a textured Co (1)/Pt (1)/Co (1)/Pt (0.5)/Al-O (2)/Pt (5) (thickness in nm) junction with perpendicular magnetic anisotropy [125]. In this case the TAMR has also been reported to be dependent strongly on the crystalline structure of the tunnelling barrier [126]. By replacing an amorphous Al-O barrier with highly-textured MgO in MTJs with $Co_{0.49}Fe_{0.21}B_{0.30}$/$Co_{0.70}Fe_{0.30}$/Oxide/$Co_{0.70}Fe_{0.30}$/$Co_{0.49}Fe_{0.21}B_{0.30}$, The TMR has been increased from 89% to 377% at 10 K.

3.3.2. Antiferromagnetic spintronics

Antiferromagnetic (AF) materials have been investigated intensively both theoretically and experimentally since the initial discovery by Néel [127]. For example, MnOx exhibits AF behaviour due to the antiparallel alignment of Mn magnetic moments [128] via superexchange interactions [129]. Due to the antiparallel alignment of the moments with the same amplitude, it is very difficult to characterise the AF behaviour directly using macroscopic measurements. Accordingly, a FM/AF bilayer has been commonly used to induce interfacial exchange coupling to pin the magnetisation of the FM layer. This results in a shift in the corresponding magnetisation curve, which is known as exchange bias field H_{ex}, along the direction of the magnetic field applied [130]. In such a bilayer, the AF properties, *e.g.*, magnetic anisotropy and temperature dependence, can be indirectly characterised by measuring H_{ex} due to the interfacial FM/AF coupling. From the device application point of view, H_{ex} can pin one of the FM magnetisations in a FM1/NM/FM2 junction, providing a spin-valve structure [131]. By replacing the NM layer with an insulating barrier, MTJ can be fabricated in a similar manner. MTJ is a basic building block for a read head of HDD, which is the most common data storage recording almost 85% of the information produced by human being. MTJs are also used as a data bit cell of MRAM.

Recently, by flowing an electrical current in an AF layer, spin polarisation has been demonstrated to be induced, leading to AF spintronics [132],[133]. For these spintronic applications, an $IrMn_3$ alloy has been predominantly used due to its corrosion resistance and robustness against device fabrication processes in nanometre-scale in both thickness and in-plane dimensions. STT on AF layer has theoretically been predicted by Núñez *et al.* [134] and has experimentally confirmed by Wei *et al.* by measuring the current dependence of an exchange bias field in a spin-valve consisting of CoFe (10)/Cu (10)/CoFe (3)/FeMn (8) (thickness in nm) [135]. A damping-like STT has also been calculated to induce the precessional motion of an AF magnetic moment, resulting in THz oscillation [136], which has been experimentally demonstrated in a spin-Hall oscillator [137] and imaging [138]. Spin pumping from the AF layer has also been measured recently [139]. However, the spin diffusion length in the AF layer is measured to be at the order of a few nm [133].

From the application viewpoint, a large anomalous Hall effect has been reported in non-collinear AF materials, *e.g.*, Mn_5Si_3 [140], Mn_3Sn [141] which is also knows as a Wyle metal. A spin Hall effect has then been measured in $Ir_{0.20}Mn_{0.80}$ [142] for example, revealing the spin Hall angle to be almost 80% of Pt value. Spin Hall magnetoresistance has also been reported in bilayers, *e.g.*, YIG/$IrMn_3$ [143].

The 90° order-parameter rotation in AF CuMnAs has been performed by a current density of 10^6 A/cm^2 with a ~1 ps pulse, which has been detected via anisotropic magnetoresistance [144]. Additionally, CIMS has been demonstrated in FM/AF bilayers via the creation of in-plane exchange bias recently [145]. The electrical switching of AF ordering can be read using anisotropic magnetoresistance and spin Hall MR (see Section 3.1). Complete electrcal writing and reading can be achieved with large signals [146]. These findings prove that AF spintronics can offer new devices with THz operationability. It should be noted that similar behaviour and devices can be achieved using ferrimagnets (see for example, [147]).

3.4. Magnetic skyrmions

The Dzyaloshinskii-Moriya interaction (DMI) is described by

$$H_{\mathrm{DMI}} = -\vec{\boldsymbol{D}} \cdot \left(\overrightarrow{\boldsymbol{s}_i} \times \overrightarrow{\boldsymbol{s}_j}\right) \qquad (14)$$

where $\vec{\boldsymbol{D}}$ is the DMI vector based on the crystalline structure [148],[149]. Note, that due to the cross product, Eq. (14) contains a chirality. As shown in Fig. 10, in a FM film with perpendicular anisotropy, the spins can rotate either along the radius or circumference to form a vortex configuration [150]. The difference in the rotation depends on the direction of the Dzyaloshinskii–Moriya vector.

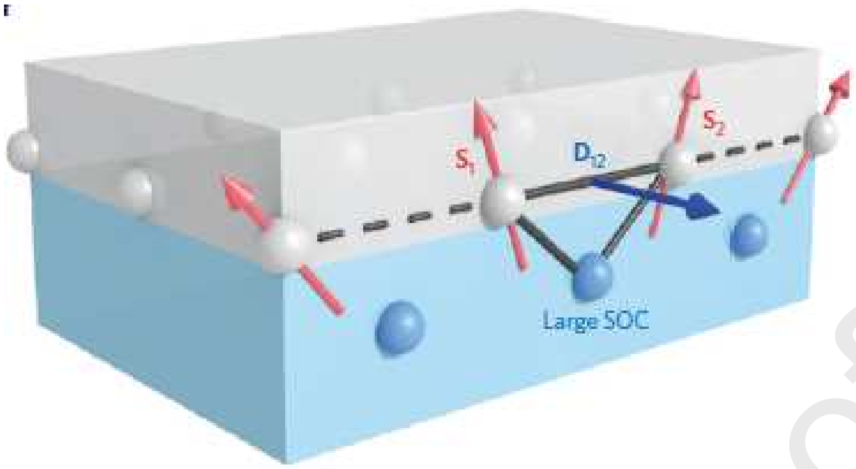

Fig. 10 Schematic diagram of DMI induced at the FM/HM interface [150].

A magnetic skyrmion is a quasi-particle theoretically predicted by Skyrme [151], consisting of a vortex configuration of magnetic spins as Fig. 11. The skyrmions can be categorised into three types: Bloch, Néel and anti-skyrmions. The Bloch type is formed by spin alignments with continuously rotating across the skyrmion radius from perpendicular-to-plane to in-plane and back to perpendicular-to-plane, the in-plane component of the magnetization being along the radius. The Néel type is formed by the uniform rotation of spins but the in-plane component of the magnetization is tangential to the radius. The anti-skyrmion is a combination of these two types with in-plane spin rotation along two directions.

The first observation was made by Mühlbauer *et al.* [152] in a MnSi film. The diameter of the skyrmion (typically of the order of ~10 nm) can be controlled by the type of material and magnetic fields. These skyrmions can be displaced by an electrical current, allowing the use of skyrmions instead of magnetic DWs as an information career in a racetrack memory [153]. Magnetic skyrmions are solid states topologically protected defects. However, stable smectic liquid-crystalline structure of skyrmions has also recently been observed [154].

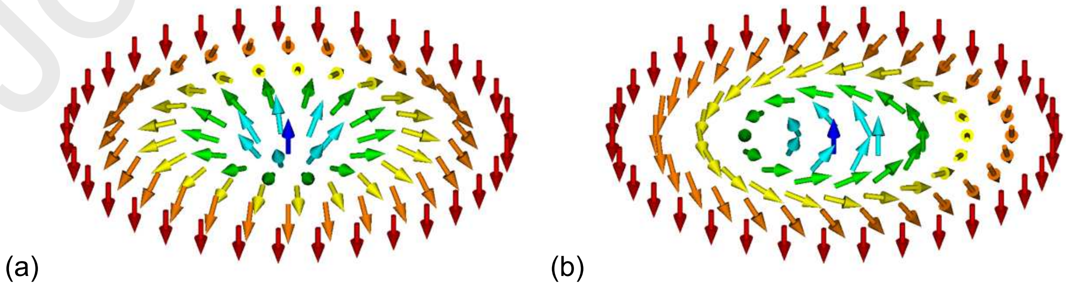
(a) (b)

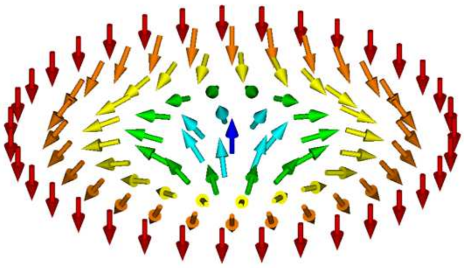

(c)

Fig. 11 Skyrmions in a 2D FM with uniaxial magnetic anisotropy along the vertical axis. Moving along a diameter, the spin rotates (a) Bloch type by 2π around an axis perpendicular to the diameter and (b) Néel type by 2π around the diameter [155] and (c) anti-skyrmion.

3.5. Topological insulators

Topological insulators (TIs) have been theoretically proposed in two-dimensional (2D) materials in 2005 [156],[157]. The theory has later been extended to the three-dimensional (3D) scenario [158]. Here, a spin gapless state needs to be formed at the edge (for 2D) or on the surface (for 3D), where an opposite spin current flows in an opposite direction, *i.e.*, helical state. For the 2D TI, the conduction and valence bands are connected by a cross-shaped edge bands across the Fermi level, forming a spin gapless state. By stacking the 2D TI, a 3D weak TI can be formed, while intrinsic spin gapless band, *i.e.* Dirac cone, in 3D can form a strong TI.

Experimentally, 2D quantum well consisting of CdTe/HgTe/CdTe has been widely studied since its conductance measurements [19]. For a 3D case, $Bi_{1-x}Sb_x$ alloys have been predicted to be TI with the (111) surface [159] and experimentally confirmed with angle-resolved photoemission spectroscopy (ARPES) [160]. TI has been discovered at the center of the surface Brillouin zone with only one Dirac cone in tetradymite-type crystal structures Bi_2Se_3 [161] and Bi_2Te_3 [162]. Similarly, TI has been demonstrated in the other materials, such as thallium-based chalcogenides ($TlBiSe_2$ [163],[164] and $TlBiTe_2$ [165]). Topological Hall effect has been predicted [166] and measured in a FM/NM TI bilayer of $Cr_x(Bi_{1-y}Sb_y)_{2-x}Te_3/(Bi_{1-y}Sb_y)_2Te_3$ [167] for example. Such TIs have also been reported to exhibt large spin-Hall angles, *e.g.*, 2~3.5 for Bi_3Se_2 and 52 for BiSb at RT [168]. In a $Bi_{0.9}Sb_{0.1}$/MnGa bilayer, for example, the critical current density for STT switching has been reported to be 1.5×10^6 A/cm^2, which can be applicable for devices.

4. Electric Field Applications

4.1. Voltage controlled magnetism

In 2000, Ohno et al have achieved a magnetic phase transition between ferromagnetic and paramagnetic phase by applying a bias voltage on an InMnAs layer sandwiched within FET [169]. A positive bias on the gate created an electric field which repels holes, thus reducing the Mn-Mn exchange interactions causing the Mn ions to become paramagnetic. A negative voltage generates an electric field which attracts holes, thus strengthening the Mn-Mn exchange interactions and causing the Mn ions to become ferromagnetic. Although these phenomena were only seen at 25K with a bias voltage of ± 125 V, this constituted a significant step towards the realisation of fully electrically controlled spintronic devices.

Gate control of the spin-orbit interaction in InGaAs was demonstrated by Nitta *et al.* [170]. This is clear evidence of the controllability of the spin orbit interaction in 2DEG by an electric field through the Rashba Hamiltonian. They have observed Schubnikov-de Haas oscillations in an $In_{0.53}Ga_{0.47}As/In_{0.52}Al_{0.48}As$ QW as a function of a gate voltage. Recently, full gate-voltage operation has been demonstrated [171]. By applying a few V (up to ± 3 V), a uniform oscillation was measured in a non-local geometry below 40K. This result unambiguously proves the gate operation by an electric field.

4.2. Voltage-control in a ferromagnet

A similar control in magnetic behaviour has been demonstrated in FePd [172] as well as an ultrathin Co film [173]. For a sample, consisting of a 0.4 nm thick Co layer, + 10 V induces FM but – 10 V induces NM behaviour, corresponding to ± 2 MV/cm^2. Similarly, Ni nanoparticles dispersed between Ti and Pt layers show a change between superparamagnetism and ferromagnetism with respect to the in-plane strain directions [174]. The voltage control is achieved via the electrical modulation of the spin-orbit interaction at the interface between a 3*d*-transition FM and a dielectric layer.

Voltage control switching of magnetisation has been implemented in MTJs in the view of zero standby power and ultralow active power consumption [175]. Voltage-controlled magnetic anisotropy (VCMA) has been demonstrated in an ultrathin Fe layer with atomical iridium doping. In a Cr (30)/Fe (1.0)/Ir (0.05)/MgO (2.5) (thickness in nm) junction, a large interfacial perpendicular anisotropy up to 3.7 mJ/m^2 is achieved, which is 1.8 times larger than that of the pure Fe/MgO interface. The VCMA coefficient is reported to be up to 320 fJ·V/m) as well as high-speed response.

Ionic materials have also been used to further extend the controllability by a voltage application [176]. The non-volatile voltage control of the DMI by ionic-liquid gating on a Pt/Co/HfO_2 film. The voltage effect is reported to scale with the voltage application time, which can be linked to the migration of oxygen species from HfO_2 into Co and Pt. The Curie temperature (T_C) of Co can be controlled by applying the gate voltage of ± 2 V through forming an electric double layer (EDL) in a polymer film containing an ionic liquid, which is induced by a large amount of carrier density control due to the formation of the EDL [177].

5. Electromagnetic Wave Application

5.1. Optical induction

5.1.1. Photoexciation

Another method for creating a spin current is photoexcitation, which uses circularly polarised light to excite spin-polarised electrons and typically detects the spin polarisation as electrical signals. The possibility of generating a spin-dependent current through thin film tunnel junctions consisting of Co/Al_2O_3/GaAs and Co/τ-MnAl/AlAs/GaAs has been first discussed by Prins *et al.* using photoexcitation [178]. For the former structure, a spin-dependent tunnelling current is observed, while only magnetic circular dichroism (MCD) signals are seen in the latter. In their experiment, a sample with a 2 nm thick Al_2O_3 tunnelling barrier showed the largest helical asymmetry of approximately 1.2% at 1.5 eV (near the GaAs band gap) in the photoexcited current. Accordingly, many studies of spin-dependent tunnelling through MOS junctions have been carried out *e.g.*, Ref. [179], especially to achieve optically pumped spin-polarised scanning tunnelling microscopy (SP-STM) [180].

Accordingly, evidence for RT spin generation has been systematically investigated at the FM/SC interface in forward bias [181]. The bias and GaAs doping density dependence of photoexcited currents suggest that electron tunnelling is the spin-dependent transport mechanism. Temperature-dependent measurements of band gap engineered NiFe/AlGaAs barrier/GaAs structures support the mechanism. In addition, strong photoexcited currents at RT have been observed in spin-valve/semiconductor structures. The difference in the optical magnetocurrent obtained between parallel and antiparallel spin-valve configurations is extremely large (up to 2,400%). The photon energy dependence of the photoexcited currents also proved that the largest signals can be achieved with the photon energy at the SC bandgap. The effect of a QW in the semiconductor on spin-polarised electron transport across the FM/SC interface has also been made [182]. Since 20 nm thick FeCo and Fe films are used for the measurement, MCD background signals dominate the polarised photocurrent, resulting in at most, 0.5% of the photocurrent being attributable to a true spin-dependent signal at 10K. The spin filtering effect can be used for future spintronic devices, such as an optically assisted magnetic sensor.

5.1.2. All optical magnetisation switching

Ultrafast light pulses in the femtosecond regime have been used for all-optical magnetisation reversal. To understand this phenomenon, the easiest route is to use circularly- and linearly-polarised light, which carries angular momentum. Such circularly-polarised light has been used for all-optical magnetisation reversal in a 20 nm thick Ni film [183]. The reversal speed is reported to be 260 fs, which is much faster than that in the other devices, such as MTJs and GMR junctions. $[Co(0.4)/Pt(0.7)]_N$ (thickness in nm, $N \leq 8$) multilayers also show magneto-optical magnetisation reversal [184]. This is a new method for the magneto-optical control of a FM magnetisation applicable for integrated magneto-optical data storage [185].

Circularly-polarised pulsed light has also been introduced into 10 nm thick Fe to generate a pulsed current [186]. The pulsed current is detected up to 20 THz via the inverse spin Hall effect through a neightbouring Au layer. This method has been further advanced to serve as a source of THz radiation [187],[188]. A further application is to switch a magnetic storage layer by introducing ultrafast laser pulses as a means of energy-efficient magnetic storage. Single pulse switching has been demonstrated [189]. Magnetisation reversal still holds a great advantage over the current Si technology due to its reversal speed which is in the femtosecond [190]. A focused circularly polarised beam (100 μm diameter and 40 fs pulse) has been used to reverse the magnetisation of a $Gd_{0.220}Fe_{0.746}Co_{0.034}$ film. A small Gilbert damping constant is essential for high-frequency operation.

5.2. Microwave induction

5.2.1. Spin pumping

FMR excitations under microwaves irraditation has bee studied in FM/NM bilayers. By an inverse effect of the spin-transfer torque, the magnetisation precession in the FM layer yields a DC spin-polarised difusion current in the NM layer.L This phenomenon is called spin pumping [191]. A spin current generated by the spin pumping has been detected as an inverse spin Hall voltage [192]. A similar effect can be observed using a FM insulator, offering a new paradigm for spintronics. The spin pumping into a superconducting material has been demonstrated in a $Ni_{0.8}Fe_{0.2}$/Nb bilayer system, showing decrease in the spin pumping signal below the superconducting transition temperature [193].

5.2.2. Ferromagnetic magnetic resonance

In order to adopt spintronic devices into the current Si technology, which is operated over 3 GHz at this stage, spin operation at a few GHz frequency is required. As a first step towards high-frequency operation, both fast settling of spin oscillation, which is defined by a damping constant, and fundamental spin dynamics in devices need to be investigated.

Ferromagnetic resonance (FMR) has been measured for a permalloy (Py, $Ni_{0.8}Fe_{0.2}$) film [194]. The relaxation time was found to be of the order of 10^8 s^{-1} and it depends on the thickness of a capping Cu layer. This small value of the damping constant (≥ 0.02) is an important parameter for the reduction of a switching current. To date permalloy films have been commonly used. However, Heusler alloy films can have much smaller damping constants compared to permalloy [195],[196],[197] with values of α down to the range of 0.0005 [197]. Aditionally, they can have more advantages due to their very large spin polarisation (100% in theory, recently demonstated experimentally in Ref. [197]).

5.2.3. Spin-transfer torque oscillation

In a GMR nanopillar, microwave oscillations have been demonstrated taking advantage of the angular dependence of STT without the application of an external magnetic field [198]. The nanopillar consisting of a $Ni_{0.81}Fe_{0.19}$ (4)/Cu (10)/$Ni_{0.81}Fe_{0.19}$ (15) (thickness in nm) stack shows a frequency-dependent STT. Broader frequency response has been achieved for a spin-valve nanopillar of $Ni_{0.81}Fe_{0.19}$ (5)/Cu (40)/$Ni_{0.81}Fe_{0.19}$ (60) (thickness in nm) in the oscillation frequency range between 300 kHz and ~ 1.1 GHz. High-frequency operation has then been extended to a MTJ nanopillar of $Co_{0.60}Fe_{0.20}B_{0.20}$/MgO/$Co_{0.60}Fe_{0.20}B_{0.20}$ with microwave generation in the vicinity of 7 GHz [199] and (3 ~ 8) GHz [200]. The frequency of these devices can be controlled by a bias current or voltage.

To date, the linewidth of the microwave oscillation in MTJ is still of the order of ~ 100 MHz, which is much wider than that required for device applications. Typically, Q-factor of 10,000 is required for reliable device operation, leading to < 1 MHz linewidth. These devices also have an output power of ~ 0.1 μW, which is three orders of magnitude larger than the conventional GMR-based oscillators.

Vortex core oscillation has also been reported in the frequency range between 300 kHz and 1.1 GHz in a Py (60)/Cu (40)/Py (5) (thickness in nm) nanopillar [201]. Electrically switching of a vortex core has been demonstrated with an ac current in a 50 nm thick Py disc (diameter: 1 μm) [202].

In theory, these FM discs and FM/NM/FM stacks can be operated almost up to the FMR frequency (~ a few 10 GHz), which has better advantage than the current Si-based devices. In preliminary demonstrations, a point contact can realise very large Q-factor for the frequency-dependence of the power spectral density [203]. However, by patterning the FM layer or the entire GMR/TMR stack into a nanopillar or disc, the Q-factor decreases significantly due to the presence of the edges. In order to overcome this issue, a new design needs to be developed.

5.2.4. Spin-orbit torque oscillation

As discussed in Section 3.2, spin-orbit torque (SOT) can also switch a FM magnetisation and induce its oscillatory behaviour [204],[205]. SOT is known to be more efficient and faster than STT by almost one order of magnitude. SOT oscillations have been reported in MTJ of CoFeB/MgO/CoFeB patterned on a Ta electrode [206]. Under a magnetic field application of – 160 Oe, 1.6 ~ 1.8 GHz oscillation is realised. Subsequently, higher oscillation of ~7.5 GHz has also been demonstrated by introducing an electrical current into a micron-size disc of NiFe (5)/Pt (8) (thickness in nm) [207]. By applying the effects of external microwave signals on SOT oscillators consisting of Py (5)/Pt (8) (thickness in nm) discs, the frequency of the auto-oscillation can be efficiently synchronised using an external RF frequency equal to twice that of the auto-oscillations [208]. SOT is characterised a strong increase of the oscillation linewidth with temperature which is correlated with the emergence of an additional higher-frequency oscillation mode [209].Similar GHz oscillations have been realised in YIG/Pt [210] and Bi_2Se_3 [211].

5.3. Spin waves

Low energy magnetisation dynamics can be described as oscillatory motion of the magnetisation, *i.e.*, by spin waves and their quanta, magnons. The magnetisation precesses in the vicinity of its equilibrium state and the minor precessional motion propagates in the lattice, which can be detected, *e.g.*, by Brillouin light scattering (BLS). Hence the oscillatory motion is tied to the lattice and can be quantised as a magnon. The magnon flow can be determined as

$$\overrightarrow{\boldsymbol{J_m}} = \hbar \textstyle\sum_{\boldsymbol{k}} \overrightarrow{\boldsymbol{v_k}}\overrightarrow{\boldsymbol{n_k}}, \qquad (15)$$

where $\overrightarrow{\boldsymbol{v_k}}$ is the group velocity of the spin wave ($=\partial\omega_k/\partial\vec{\boldsymbol{k}}$) and $n_{\boldsymbol{k}}$ is the distribution function of the spin wave.

Spin waves have been reported to possess very long coherence length, especially in insulators, *e.g.*, 7 μm for α-Fe_2O_3 [212] and cm distances for YIG, which can be useful for logic applications. A nanoscaled reconfigurable directional coupler has been calculated and fabricated using YIG [213]. YIG with the thickness and width down to 39 and 50 nm, respectively, has been used as a waveguide [214]. Further reduction may allow such spin-wave logic to be implemented in a logic device. The field is often termed magnonics or magnon spintronics. For recent reviews see, *e.g.*, Refs. [6],[7]. Issues are generation, propagation and detection of spin waves, manipulation, interaction (in particular nonlinear interactions), as well as novel states such as macroscopic magnonic quantum states [215]. Progress has been very successful, provided by by the superior properties of spin waves, such as short wavelengths (favouring scalability down to the nanometre range [216]), good isolation of waveguides (no unintended cross talk), parametric amplification [217], access to interference based functionalities (such as the majority gate [218],[219]) and nonlinear interaction (needed for information processing). Many of the concepts developed some time ago in the field of integrated optics have been successfully transferred into magnonics. Examples are the development of ultra-narrow magnonic waveguides, majority based logic [220], the magnon transistor [221], magnonic Bose-Einstein condensates carrying supercurrents, Boguliubov waves and the ac Josephson effect [222].

6. Spin-Band Splitting

6.1. Spin filtering

The search for an applicable spin-filtering layer has successfully produced very large TMR values using a large Zeeman splitting in the magnetic semiconductors EuO and EuS [223]. Spin filtering has also been reported using Europium and Chromium calcogenides rock-salt, *e.g.*, EuO and EuSe, and the spinels, *e.g.*, $CdCr_2S_4$ and $CdCr_2Se_4$ [224],[225]. For example, EuS shows a TMR ratio of up to 110% at 2K, which disappears above $T_C \sim 16.8$K [226]. Larger TMR ratios has been reported using coherent tunnelling with a MgO barrier as detailed in Section 2.1, of which lattice matching can be precisely controlled by Al doping [227].

6.2. Spin light emitting diode

Since DMS show a large Zeeman splitting and ferromagnetism [228], DMS can be used as a spin aligner to inject spin-polarised carriers, *i.e.*, spin-polarised electrons for *n*-SC or holes for *p*-SC. The spin polarisation of the injected carriers is detected optically through circularly polarised EL from the SC (*e.g.*, GaAs), which are called spin LEDs. With FM *p*-GaMnAs as a spin aligner, spin-polarised hole injection has been reported at low temperature [229]. At forward bias, spin-polarised holes from the *p*-GaMnAs as well as unpolarised electrons from the *n*-GaAs layer are injected into the InGaAs QW, so that the recombination of the spin-polarised holes can create circularly polarised EL emission from the QW. However, as the spin relaxation time for the holes is much shorter than that for the electrons [230], the spin polarisation signal through the recombination process in the GaAs is very small (about ± 1%). On the other hand, using paramagnetic *n*-BeMnZnSe with large Zeeman splitting as a spin aligner, highly efficient electron spin injection has been achieved with the applied field of ~ 30 kOe (spin polarisation in EL ~ 90%) [231]. This is because the spin diffusion length of the electrons has been reported to be above 100 μm in the GaAs [232].

Similar results have been obtained using CdMnTe [233], ZnMnSe [234],[235], ZnSe [236] and MnGe [237] but only at low temperatures (typically $T < 80$K). Since RT ferromagnetism has been predicted in several DMS compounds [238] but not yet observed, spin injection at RT with a DMS may be achievable in the near future.

7. Influence of Thermal Gradient

Spin caloritronics has a great potential for energy harvesting and highly efficient spin transport [239]. By attaching Pt electrodes at both ends of a $Ni_{0.81}Fe_{0.19}$ strip with a temperature gradient across the strip, spin-polarised electrons with opposite sign of the polarisation can be collected at both ends dependent upon the directions of magnetisation of the strip and the temperature gradient (spin Seebeck effect) [240]. The structure is much larger than the nanometre scale (up to a millimetre scale), however, the essence of the effect can be understood in a simple one-dimensional (1D) model. This effect converts thermal energy into a spin voltage, which is another method to generate spin-polarised electrons.

In FM insulators, *e.g.*, YIG and ferrites (Fe_2O_3), spin waves can be generated by a thermal gradient due to the spin Seebeck and Nernst effects (see Fig. 12) without an associated electrical current, see, *e.g.*, Ref. [240]. Also, the opposite effect of spin-wave heat conveyers is known [241]. This is advantageous for harvesting energy from heating source which can be solar radiation or heat from hot parts of electronic circuits.

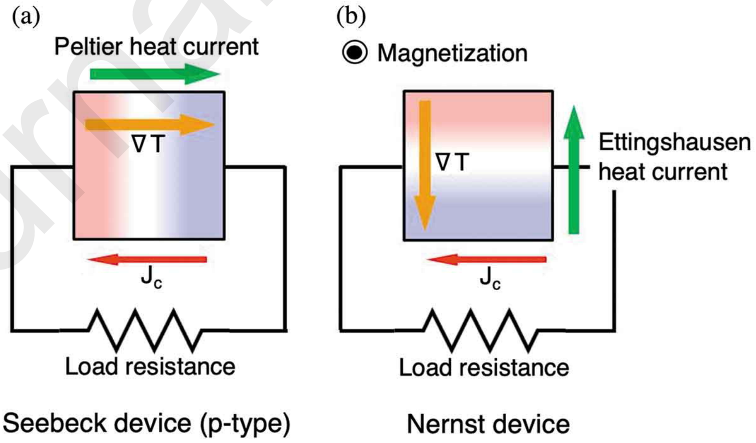

Fig. 12 Schematic images of flows of energy in (a) the Seebeck device (p-type) and (b) the Nernst device during operation [242].

Similarly, anomalous spin caloritronic effects have been investigated. The anomalous Nernst effect (ANE) is the voltage generation along the cross product of the magnetisation and the temperature gradient ∇T. The amplitude of ANE is controlled by the magnitude of magnetic anisotropy of a material used [243]. On the other hand, anomalous Ettingshausen effect (AEE) can be induced ∇T along the cross product of the current J_c and the magnetisation [244]. In an FePt thin film, the reciprocal relationship between ANE and AEE has been evaluated. These spincaloritronic effects are promising for energy harvesting from thermal gradients but the amplitude oft these effects is still too small to date for practical application.

8. Geometrical Phase

The quantum phases of charged particles in mesoscopic structures have been investigated intensively. Their interference and oscillatory behaviours were induced by application of an external field [245]. Electrons traveling along semiconductor or normal metal rings threaded by a magnetic flux acquire a quantum dynamical phase that produces interference phenomena such as the Aharonov-Bohm (AB) [246] and Altshuler-Aronov-Spivak (AAS) [247] effects. AB oscillations have been reported in a NiFe/Cu/NiFe nanoring, demonstrating a crossover regime between the quantum-phase effects and ferromagnetism [248]. In addition, when the spin of the electron rotates during its orbital motion along the ring-shaped path, the electron acquires an additional phase element known as the geometrical or Berry phase [249].

Although spin geometrical phase has been demonstrated to be controlled in a semicondutor ring array [250], no conclusive experimental proof on a persistent spin current has been reported to date unfortunately. A NM nanoring [inner diameter: (200 ~ 350) nm] with an FePt nanopillar [diameter: (120 ~ 270) nm] inside has been fabricated by a combination of electron- beam lithography and Ar-ion milling [251]. The Cu nanoring is 150 nm wide and 20 nm thick. The centre nanopillar is designed to provide a nonuniform magnetic field in the nanoring in its remanent state after perpendicular saturation. Four contacts are fabricated near the nanoring for measurement of the induced current. A minor change in the non-local signal is demonstrated indicating the possible experimental confirmation of a persistent spin current induced by the Berry phase.

9. Mechanical Rotation

In 2011, Matsuo *et al.* [252] proposed a method for generation of a pure spin current by mechanical rotation, based on the Barnett effect [253],[254]. By solving the Pauli-Schrödinger equation, they predicted that a spin current could be generated via angular momentum carried by a conductor rotating mechanically at high speed given by a $(\vec{\boldsymbol{\Omega}} \times \vec{\boldsymbol{R}}) \times \vec{\boldsymbol{B}}$ term, where $\vec{\boldsymbol{\Omega}}$ is angular frequency, $\vec{\boldsymbol{R}}$ is distance from the centre of rotation and $\vec{\boldsymbol{B}}$ is applied magnetic field. This additional term gives rise to spin-dependent wave packet velocities. For materials with a large spin-orbit coupling parameter, a detectable spin imbalance is expected to be accumulated at the edges of the sample as electrons with opposite spins migrate in opposite directions.

The magnitude of the spin current generated by a uniformly rotating body is given by

$$\overrightarrow{J_S} = 2nqR\eta_{SO}\frac{\hbar\vec{\Omega}}{E_F}\omega_C, \qquad (16)$$

where $\overrightarrow{J_S}$ is the spin current density, q is the electron charge, n is the electron density, R is the radius of rotation, η_{SO} is the spin-orbit coupling parameter of the material, Ω is the angular frequency and E_F is the Fermi energy. The term $\omega_C = qB/m$ is the cyclotron frequency for the wave packet of electrons treated in the derivation, where q is the charge of the wave packet and m is its mass. In the case of B ≈ 1 T, Ω ≈ 1 kHz, η_{SO} ≈ 0.59 (as in Pt), k_F ≈ 10^{10} m^{-1} and R ≈ 0.1 m, Matsuo *et al.* estimates the spin current generated at the edges of the Pt foil to be of $\left|\overrightarrow{J_S}\right|$ ≈ 10^4 A/cm^2. In the presence of impurity scattering, the spin current for the radial (J_S^r) and azimuthal (J_S^ϕ) directions [see Fig. 13(a)] is given by [255]

$$J_S^r = \frac{\tau\omega_C}{1+(\tau\omega_C)^2}\left|\overrightarrow{J_S}\right|, \qquad (17)$$

$$J_S^\phi = \frac{(\tau\omega_C)^2}{1+(\tau\omega_C)^2}\left|\overrightarrow{J_S}\right|, \qquad (18)$$

where τ is the relaxation time due to the impurity scattering. With an experimental condition reported recently [256], $\tau\omega_C$ is expected to be ~ 10^{-3} for Pt, and the radial component will dominate over the azimuthal element.

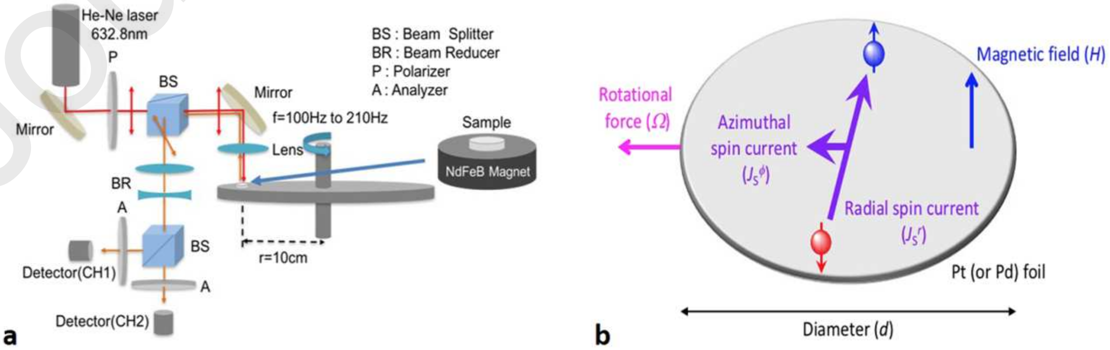

Fig. 13 (a) Magneto-optical measurement set-up. The magnified diagram in (b) shows the distribution of the generated spin current.

As schematically shown in Fig. 13(b), accumulated spins with opposite signs at both ends of the samples can be detected as an in-plane "magnetic moment" using a magneto-optical Kerr effect (MOKE) set-up [256]. This is due to small misalignment of the incident and reflection beam from the plane normal of the sample, confirming the sensitivity of the set-up. The MOKE measurement report that small magnetic fields below $|H| = \pm 4$ kOe only induce the Barnett effect for the foil attached on a rotational plate with the radius of 0.10 m due to the Barnett effect [253] as observed earlier [257]. On the other hand, the fields above ± 4 kOe were found to generate the spin current discussed above. Such a spin current proves that the spin-polarised carrier can be generated by mechanical rotation, which is analogous to the spin Hall effect. Kobayashi *et al.* [258] have also detected spin currents generated by using Rayleigh-type surface acoustic wave (SAW) in $Ni_{0.81}Fe_{0.19}$/Cu bilayer system. By measuring microwave absorption at SAW excitation frequency at 1.5 GHz, a large spin-rotation coupling effect was observed.

The kinetic energy of fluid has been demonstrated to be converted into a spin current [259]. Here, the spin–orbit interaction in Hg liquid plays a key role for the spin conversion, which has been detected via the inverse spin Hall effect. Such magnetohydrodynamic spin generation can also be categorised in spin mechatronics.

10. Spintronic Materials

10.1. Half-metallic ferromagnets

For further improvement in the MR junctions to meet the requirements for the set goals of 10 Gbit MRAM and 2 Tbit/in^2 HDD as shown in Fig. 14, HMF needs to be developed to achieve 100% spin polarisation at E_F at RT [260],[261] leading to an infinite MR ratio using Eq. (3). The half-metallicity is induced by the formation of a bandgap δ only in one of the electron-spin bands in density of states (DOS). There are four major types of HMFs theoretically proposed and experimentally demonstrated to date; (i) oxide compounds (*e.g.*, rutile CrO_2 [262] and spinel Fe_3O_4 [263]); (ii) perovskites (*e.g.*, (La,Sr)MnO_3 [264]); (iii) magnetic semiconductors, including Zinc-blende compounds (*e.g.*, EuO and EuS [265], (Ga,Mn)As [22] and CrAs [266]) and (iv) Heusler alloys (*e.g.*, NiMnSb [267]). Low-temperature Andreev reflection measurements have confirmed that both rutile CrO_2 and perovskite $La_{0.7}Sr_{0.3}MnO_3$ compounds possess almost 100% spin polarisation [268], however, no experimental report has been proved the half-metallicity at RT to date. Among these HMFs, magnetic semiconductors have been reported to show 100% spin polarisation in a film form due to their Zeeman splitting in two spin bands. However, their T_C are still below

RT [269]. The Heusler alloys exhibit the half-metallicity at RT in a bulk form but not in a film form to date [269],[271],[272]. Even so, the Heusler alloy films can be the most promising candidate for the RT half-metallicity due to their lattice constant matching with major substrates, high T_C and large δ at E_F in general. The largest GMR ratio of 82% has been achieved at RT by sandwiching a Ag spacer with NiAl to improve the interfacial lattice matching as $Co_2Fe(Ga_{0.5}Ge_{0.5})$/NiAl/Ag/NiAl/$Co_2Fe(Ga_{0.5}Ge_{0.5})$ [273].

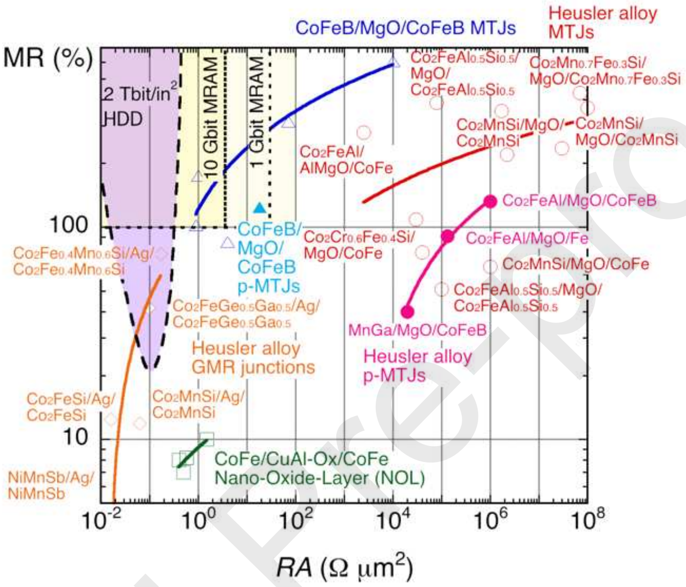

Fig. 14 Relationship between a MR ratio and *RA* of MTJs with CoFeB/MgO/CoFeB (blue triangles), nano-oxide layers (NOL, green squares) and Heusler alloys (red circles) with in-plane (open symbols) and perpendicular magnetic anisotropy (closed symbols) together with that of GMR junctions with Heusler alloys (orange rhombus). The target requirements for 2 Tbit/in^2 HDD read heads as well as 1 and 10 Gbit MRAM applications are shown as purple and yellow shaded regions, respectively. After Ref. [274].

10.2. Low damping materials

For faster magnetisation reversal in a data bit of MRAM, a low damping constant is required, resulting in smaller switching current density for reversal. To date, $Ni_{0.8}Fe_{0.2}$ has been used as a low damping material, while Heusler alloys have been investigated as shown in Fig. 15 for further reduction in their Gilbert damping constant α. Theoretically, α is known to be proportional to DOS at E_F [275], ensuring the half-metallic ferromagnets to exhibit a small α (< 0.01). Here, the magnetisation damping frequency G is determined as $\gamma \alpha M_s$, where γ and M_s are gyromagnetic ratio and saturation magnetisation, respectively. α has been typically been measured by FMR [276] and time-resolved (TR)-MOKE [277].

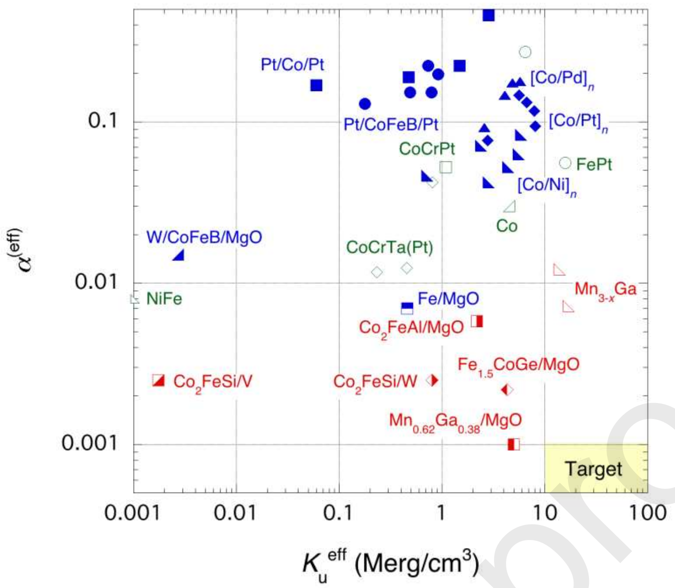

Fig. 15 Relationship between the magnetic anisotropy constant K_u^{eff} and the Gilbert damping constant α. Single films, multilayers with heavy metals and half-metallic Heusler alloy films are shown in green open, blue closed and red open symbols. Heusler alloys with MgO and heavy metals are also shown in half-closed symbols. After Refs. [278],[279],[280] and [281].

10.3. Perpendicularly anisotropic materials

A CoFeB/MgO/CoFeB system has been widely used to induce perpendicular anisotropy [282],[103]. When the size of spintronic devices is reduced, the magnetic anisotropy energy which ensures the thermal stability of its various magnetic components decreases. For very small devices (typically sub-50nm in dimensions), it is therefore preferable to use perpendicularly isotropic materials since large perpendicular anisotropy can be obtained from bulk sources such as crystalline structure or strain, or from interfaces. In addition, some layers can have a high Gilbert damping (such as the reference layer of magnetic tunnel junctions), while others must exhibit a low Gilbert damping (for instance the storage layer of STT-MRAM or the free layer of spin-torque oscillators to minimise the required excitation current).

High perpendicular anisotropy materials with large damping can be generally realized by using materials with large spin orbit constant, typically Pt, Ir and Au. Such materials are in the upper right corner of Fig.15, typically [Co/Pt] or [Co/Pd] multilayers or alloys, FePt L_10 ordered alloys. They are often used in the hard layer of MTJs.

Finding low damping material with large perpendicular anisotropy was less obvious since anisotropy and damping both originate from spin orbit coupling. Fortunately, some materials or material combinations do exhibit both properties. In particular, it was discovered that large perpendicular anisotropy exists at the interface between magnetic transition metals (Fe, Co, Ni and their alloys) and oxides (AlOx, MgO, TaOx etc,) [103],[104][282],[283],[284],[285]. This magnetic metal/oxide interface is a quite general phenomenon resulting from interfacial hybridisation between the electronic orbitals of the transition metal and those of the oxygen in the adjacent oxide layer. It turned out to be particularly useful for the realisation of CoFeB/MgO/CoFeB-based out-of-plane magnetised tunnel junctions for STT-MRAM cells [104]. The interfacial anisotropy at Fe or FeCoB rich alloy/MgO interface is significantly larger than at Co/MgO interface [104] and remarkably, as large as at (Co/Pt) interface (*i.e.*, of the order of 1.4 mJ/m²). MgO based MTJ are always annealed after deposition to improve the crystallinity of the MgO barrier and provoke the crystallisation of the FeCoB amorphous layer into a bcc crystalline layer. In this process, the B must migrate out-of the FeCoB alloy towards a B-getter layer located at the interface of the FeCoB layer opposite to the MgO interface. This B-getter layer is often made of Ta, W or Mo [104].

In STT-MRAM cells, to further increase the magnetic stability of the storage layer, it was proposed to sandwich the layer between two MgO layers [285],[286]. This allows to benefit from two MgO/magnetic metal interaces. The storage layer then has a typical composition of the form MgO/FeCoB (1.4)/Mo (0.2)/FeCoB (1)/MgO (thickness in nm). More rencently, it was proposed to further increase the anisotropy by inserting a thin MgO layer in the middle of the storage layer thus benefiting from four MgO/magnetic metal interfaces [284],[287].

Intense research on Heusler alloys for MRAM cells is ongoing. Form their bulk properties, they can realize the combination of high anisotropy, low damping and high spin polarisation thanks to their half-metallic nature. For instance, a MTJ consisting of Co_2FeAl (1.2)/MgO (1.8)/Fe (0.1)/CoFeB (1.3) (thickness in nm) has been reported to show TMR = 132% and $RA = 1\times10^6\ \Omega\cdot\mu m^2$ at RT [288]. A perpendicularly magnetised seed layer can also be used to pull out-of-plane the magnetisation of an Heusler-alloy films thanks to interfacial exchange interactions. For example, MTJ stack with $L1_0$-CoPt/Co_2MnSi/MgO/FePt has been demonstrated [289]. A W(110) seed layer has also been reported to induce perpendicular magnetic anisotropy in a $Co_2FeAl_{0.5}Si_{0.5}$ Heusler alloy layer [290].

10.4. Antiferromagnetic materials

AF metals, *e.g.*, $IrMn_3$, have been traditionally used to pin the magnetisation of the neighbouring FM layer via the interfacial exchange bias in a MR junction [291]. Due to recent progress in AF spintronics as described in Section 3.3.2 and the criticality issues of Ir as a platinum group metal, intensive investigation on AF materials have been performed. However, the majority of the AF materials have their Néel temperature T_N near or below RT. Some oxides (*e.g.*, NiO) and sulphides (*e.g.*, $CuFeS_2$) have T_N > RT but they have very poor corrosion resistance and hence cannot be used in a device. Manganese alloys (*e.g.*, $NiMn_3$ and $PtMn_3$) and nitrides (*e.g.*, $MnSiN_2$) also have T_N > RT but $NiMn_3$ has poor corrosion resistance and $PtMn_3$ has very high crystallisation temperature, indicating that they cannot be used in a device either. Therefore, there is strong demand for a new AF Heusler alloy to be developed.

One potential candidate is an AF Heusler alloy, which are categorised into two types: (i) full- and (ii) half-Heusler alloys. These alloys crystallise in (i) $L2_1$ phase with X_2YZ composition and (ii) $C1_b$ phase with XYZ composition [292]. The half-Heusler alloys have an X-vacancy in the unit cell, making them susceptible to atomic displacement. Even for the full-Heusler alloys, the perfectly-ordered $L2_1$ phase can be deformed into the $B2$ phase by atomically displacing Y-Z elements, the $D0_3$ phase by X-Y displacements and the $A2$ phase by randomly exchanging X-Y-Z elements. For the AF Heusler alloys, Ru_2YZ, Ni_2YZ and Mn_2YZ have recently been reported to exhibit AF behaviour in their $L2_1$, $B2$ and $A2$ crystalline ordering phases. By attaching a FM Fe layer to these AF layers, Hex of up to 600 Oe at 100K, 90 Oe at 100K and 30 Oe at 100K for Ru_2MnGe, Ni_2MnAl and Mn_2VAl, respectively, have been found. Mn_2VAl is found to maintain its AF properties at RT. These differences are found to be induced by the AF alignment of spin moments at the Y site in unique ordered phases. In the ordered $L2_1$ type Ru_2MnZ (Z = Si, Ge, Sn or Sb), the complex AF ordering (2nd type) is a consequence of the frustrated exchange interaction between the Mn atoms. It is concluded that Néel temperature (T_N) sharply depends on the Z element and that T_N in Ru_2MnGe can be increased by avoiding the disorder in the Mn-Z sub-lattice. For Ni_2MnAl, the (checkerboard-like) AF order only exists in the chemically disordered $B2$ phase due to the large AF nearest neighbour Mn-Mn interaction. Decreasing the atomic disorder in the Mn-Al sublattice leads to non-zero total magnetisation (ferrimagnet). The excess of Mn or Ni does not improve the quality of the AF state. From the device application point of view, Mn-based AF Heusler alloys are ideal due to their robustness against atomic disordering, especially at the interfaces to neighbouring layers.

For the Mn-based Heusler alloys, off-stoichiometric compositions have also been investigated, which maintain AF spin alignment even with some degrees of atomic disorder in the alloys. For example, by mixing two ferrimagnetic Heusler alloys, Mn_3Ga and Mn_2PtGa, $Mn_{2.4}Pt_{0.6}Ga$ has been demonstrated to show compensated ferrimagnetism supported by calculations [293]. By substituting Y elements with Mn, binary Mn-based Heusler alloys can be formed. One example is hexagonal Mn_3Ge [294]. H_{ex} of up to 1.5 kOe is measured at the bilayer of epitaxial Mn_3Ga (10 nm)/$Co_{0.9}Fe_{0.1}$ (2.5 nm) at RT. Magnetic anisotropy energy and $<T_B>$ are estimated to be 3×10^6 erg/cm^3 and ~ 400K, respectively. Recently, H_{ex} of 430 Oe has also be reported in polycrystalline $Mn_3Ga/Co_{0.6}Fe_{0.4}$ bilayers at 120K [295],[296].

By expanding the definition of the Heusler alloys to nitrides, MnN has been investigated extensively. MnN films are grown using ultrahigh vacuum sputtering in N_2 atmosphere to achieve Mn:N=1:1. A MnN/Fe bilayer has been reported to show H_{ex} of 1.4 kOe at RT with $<T_B>$ = 388K [297]. To date, the minimum thickness of MnN to induce the AF behaviour is 20 nm, which needs to be almost halved to be competitive against the 6-nm-thick Ir-Mn layer used in the latest spintronic devices.

10.5. Topological insulators and semi-metals

Topological insulators (TI) are materials that are insulating in their interior but they are conducting on their surface. The chemical doping of TI with transition metal elements, *e.g.*, Mn-doped in Bi_2Ti_3 [298] and in BiTeSe [299], has been reported to induce an intrinsic magnetisation. As a new principle of spin current generation to replace the conventional methods, *e.g.*, the spin hall effect, Rashba-Edelstein effect [300] is key effect in an interfacial two-dimensional electron system with spin splitting, which enables efficient charge-to-spin conversion (see Table 1 [18]). This is a phenomenon in which spin accumulation with the polarisation along the direction perpendicular to the current occurs as similar to the spin Hall effect. At the surface state of TI, the spin accumulation is caused by the formation of a special electronic state called spin-momentum locking.

Interfacial spin accumulation in TI of Bi_2Se_3 has been observed by applying the charge current [301], and a strong spin ransfer torque has been generated at the interface of Bi_2Se_3 by applying the charge current [302]. A spin-electricity conversion has been reported in $Bi_{1.5}Sb_{0.5}Te_{1.7}Se_{1.3}$, where an interface conduction is more dominant [303]. The magnetisation reversal by spin torque using an epitaxial $(Bi_{0.5}Sb_{0.5})_2Te_3$/Cr-doped $(Bi_{0.5}Sb_{0.5})_2Te_3$ bilayer films has also been reported [304].

11. Spintronic Devices

Figure 16 shows a summary of spintronic devices, which can be categorised into two, Mott- and Dirac-types based on electron/hole spins as well as spin waves and spin/orbit moments. For the Mott-type devices, GMR and TMR are the key phenomena used, while the spin-orbit interactions are the fundamental phenomena used in Dirac-type devices. These devices can also be grouped into three generations. The first generation is based on spin transport, which utilises electrical spin generation as described in Section 2. The second generation is based on spin dynamics employing spin-orbit effects, electric field and electromagnetic wave applications in Sections 3, 4 and 5, respectively. The latest development has been entered into the third generation employing three-dimensional structures and quantum engineering, including the applications for quantum computation.

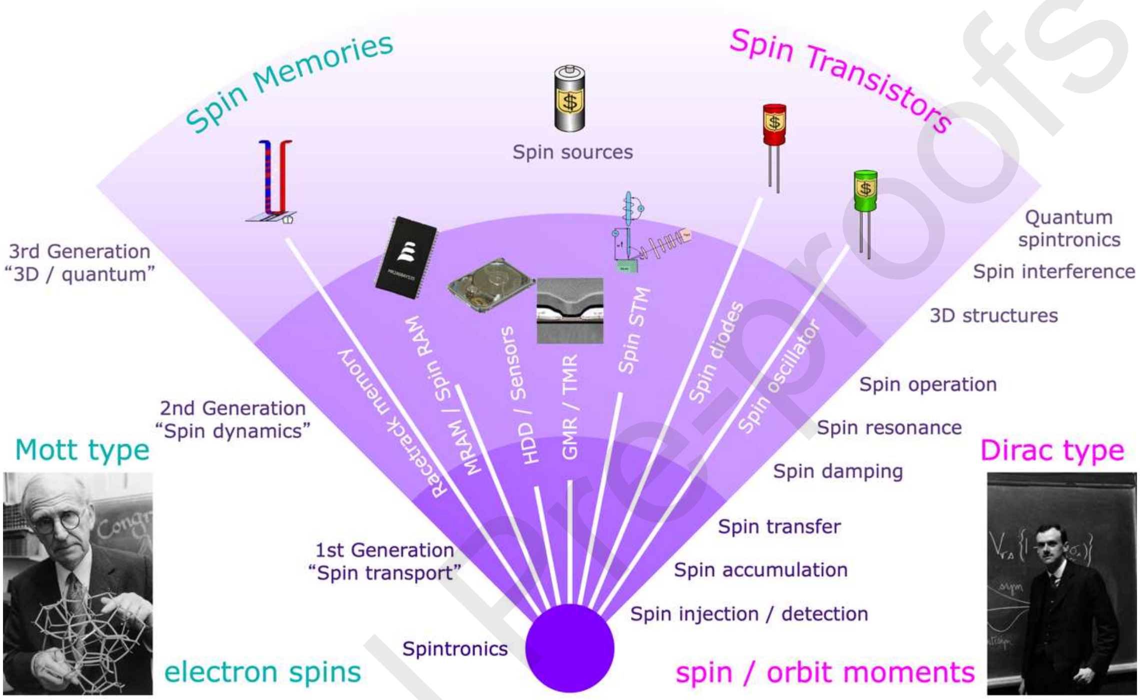

Fig. 16 List of spintronic devices. After Refs. [9] and [305].

11.1. Hard disk drive read head

HDD was introduced by IBM in 1956 to store 4.4 MB on 50 discs (2 kbit/in^2). In 1997, a GMR spin-valve HDD read head has been introduced by IBM. In 2005, a TMR head was introduced by Seagate. The MgO-based TMR technology is still used in current HDD, at areal density of > 600 Gbit/in^2 [306]. However, the *RA* product of the MTJ tunnel barrier has to decrease as the storage areal density keeps on increasing. Indeed, the size of the MTJ reader decreases as the areal density increases which imposes to reduce its *RA* product since the sensor impedance must remain of the order of a few tens of Ohms to match the pre-amp impedance. For above 2 Tbit/in^2 HDD applications, it becomes increasingly difficult to use MgO-based MTJ since the barrier thickness becomes ultra low (below 1 nm) which impacts its reliability and reduces its TMR [307]. It has been proposed by Toshiba to use spin-valves embedding a nano-oxide spacer layer (NOL) formed of an oxide AlOx layer comprising metallic Cu pinholes. These pinholes are intended to locally restrict the current path perpendicular to the GMR stack. This NOL layer is formed by oxidising an $Al_{1-x}Cu_x$ alloy [x = (2 ~ 3)%] spacer layer [308]. A $Co_{0.5}Fe_{0.5}$ (2.5)/NOL/$Co_{0.5}Fe_{0.5}$ (2.5) (thickness in nm) junction has demonstrated RA = (0.5 ~ 1.5) Ω·μm^2 and MR = (7~10)% at RT. These values are below the requirement for the 2 Tbit/in^2 HDD and the reliability of these devices is very uncertain due to the extremely high current density flowing through the pinholes. Therefore, further improvement in these junctions are crucial.

Intense research is ongoing on spin-valves based on Heusler alloys and Ag spacer layer [274] (see Fig.14) which could constitute an alternative. However, the growth of these materials often require high temperature deposition or anneal not compatible with head fabrication process. Besides, the total thickness of the reader in HDD must be as low as possible below 20 nm since it determines the reader shield to shield spacing and therefore the linear downtrack resolution. This adds another constrain in the design of the reader MR stack.

For the further improvement in the HDD areal density, a trilemma has to be overcome between areal density (grain size), thermal stability and writability [309]. To improve the writability, possible solutions consist in assisting the magnetisation switching during write by transferring additional energy to the local magnetisation through heat transfer or microwave. Heat-assisted magnetic recording (HAMR) was proposed [310],[311]. A laser beam is employed to locally transfer heat to the media. This is achieved through a plasmonic antenna which allows to create a thermal gradient as large as 10 K/nm. The resulting local heating of the media reduces the thermal stability of the data bit to be written which eases the switching of its magnetisation. A successful demonstration has been reported [312]. In 2012, TDK demonstrated a new HAMR head with the areal density of 1.5 Tbit/in^2 and bit-error rate of 10^{-2}. Seagate also demonstrated a new HAMR drive in 2012. A problem which had to be solved is the reliability of head and particularly of the plasmonic antenna which reaches quite elevated temperatures. Head lifetime above 1000 hours was demonstrated [313].

Microwave-assisted magnetic recording (MAMR) was also proposed by Zhu *et al.* as another energy assisted recording approach [314]. The MAMR utilises microwaves produced by a spin transfer oscillator patterned in the write gap of the write head to reduce the switching field by an order of magnitude [315]. Great progress has been made lately on this technology. In 2017, Western Digital announced the commercialisation of MAMR based hard disk drives.

11.2. Magnetic sensors

Current magnetic sensors have been used to detect position, angle, rotation and magnetic fields, based on three key types of technologies: Hall, AMR and GMR effects. Hall sensors are made by patterning Silicon into a cross-bar, where sensitivity can be increased by replacing Si with compound semiconductors such as InAs and GaAs. However, these sensors suffer from large temperature dependence of their output in a finite magnetic field and have limitations in their working temperature range (typically between 230 and 390K) as well as their detectable field range (between 10^2 and 10^3 kOe).

For the magnetic sensors, the presence of European companies is very large. As shown in Table 2, the magnetic sensor market is dominated by the top 10 suppliers who have 90% of the worldwide market [316]. Japan and USA are the leading players in magnetic sensors, holding 28% and 24% shares, respectively. The EU has 5 suppliers of magnetic sensors, who produce by value $575m with 38% market share, most of which are produced by SMEs. Even though over 70% of magnetic sensors are based on Hall devices, only a few suppliers have been developing GMR and TMR sensors intensively. Currently, almost 20% of sensors are based on GMR (and TMR) techniques, leading to 7.6% of the current world market. The EU-based suppliers produced almost 2.5bn sensors in 2013 [317], out of which 0.1bn units are based on GMR (and TMR) technologies. The pro-duction of sensor units is anticipated to grow monotonically and to reach 9.6bn units with revenues of $2.9bn in 2020. Hence, the development of a new highly-sensitive magnetic sensor is timely and holds large impact in our society.

Such a highly sensitive magnetic sensor holds a key for the magnetoencephalography, which can detect a small magnetic field at the resolution of ~ 5 mm in space and ~ 1 ms in time [318]. The magnetic field is generated by activated synapse voltages as an electric dipole moment, which can either be measured as a voltage, *i.e.*, brain wave, or a magnetic field induced by a current due to the synapse voltage, *i.e.*, magnetoencephalography. Since the brain is covered by a scalp and crania, which have high electrical resistance, as well as cerebrospinal fluid with low resistance, brain wave measurements cannot precisely determine the position of the activated synapse in the brain. However, these elements are transparent to a magnetic field, allowing accurate determination of the activated synapse for the case of magnetoencephalography. However, the directions of the electric dipole moments can be freely generated depending on the shape of cerebral cortex. This means a magnetic sensor for the magnetoencephalography can be very sensitive to the dipole parallel to the scalp which generates a magnetic field perpendicular to the scalp, while it can be hardly sensitive to that perpendicular to the scalp which generates a field parallel to the scalp. Currently both a superconducting quantum interference device (SQUID) and an optically pumped atomic magnetometer have been used to achieve fT/Hz$^{1/2}$ resolution. However, SQUID requires cryogenic temperature for the operation and the atomic magnetometer is not suitable for minaturisation due to the minimum size of ~ 1 cm^3 to maintain its sensitivity. Hence, it is crucial to develop new magnetic sensors with higher spatial and time resolution, so that they can be used in an array form with different tilted angles to avoid such insensitiveness.

Table 2 Supplies of magnetic sensors by revenue (in $m) [316].

Suppliers	Countries	2010	2011	Shares	Key sensors
Asahi Kasei Microsystems	Japan	300	372	25%	Hall
Allegro MicroSystems	USA	264	302	20%	Hall
Infineon Technologies	Germany	142	188	13%	Hall, GMR
Micronas	Germany	143	150	10%	Hall, (TMR)
Melexis Microelectronic Systems	Belgium	107	112	7%	Hall, (TMR)
NXP	Netherlands	92	96	6%	AMR, (TMR)
Aichi Steel	Japan	18	40	3%	Amorphous
Austria Microsystems	Austria	21	29	2%	(TMR)
MEMSIC	USA	2	29	2%	AMR
Diodes	USA	22	24	2%	Hall
Honeywell	USA				AMR
NVE	USA				GMR, TMR
Hitachi	Japan				GMR
Sinfulus	Germany				GMR, TMR
Total		1225	1499		

Using a MTJ, consisting of Si/SiO_2//Ta (5)/Ru (10)/$Ni_{0.8}Fe_{0.2}$ (70)/Ru (0.9)/$Co_{0.4}Fe_{0.4}B_{0.2}$ (3)/MgO (1.6)$Co_{0.4}Fe_{0.4}B_{0.2}$ (3)/Ru (0.9)/$Co_{0.75}Fe_{0.25}$ (5)/$Ir_{0.22}Mn_{0.78}$ (10)/Ta (5)/Ru (30) (thickness in nm), the noise density of 14 pT/$Hz^{1/2}$ has recently been reported at a single frequency of 10 Hz [319]. Further improvement in sensitivity is necessary for broader usages, especially biomedical applications.

11.3. Magnetic random access memory

The concept of MRAM was first proposed by Schwee in 1972 [320]. The functionality of MRAM was demonstrated with an Fe-Ni-Co alloy-based GMR cell [321]. In 1996, the first MTJ cell was implemented in an MRAM demonstration [322]. IBM and Motorola have independently developed 1-kbit and 512-kbit MRAM, respectively, in 1999 [323],[324]. Motorola then developed a 1-Mbit, 2-Mbit and 4-Mbit MRAM [325],[326]. NEC-Toshiba also demonstrated 1-Mbit and 16-Mbit MRAM in 2003 and 2006, respectively [327]. Fast random access has been demonstrated at a speed of ~ 5 ns for read and write [328]. In 2007, Freescale Semiconductor, which was spun off from Motorola in 2004, commercialised a 4-Mbit MRAM with a working temperature between – 40°C and 105°C, for *e.g.*, automobile applications. In 2010, EverSpin Technologies, which was spun off from Freescale in 2008, started to ship a 16-Mbit Toggle MRAM. This MRAM is field written. It is operated at a bias voltage of 3.3 V and a current of 60 mA (110 mA) for read-out (write-in) at the speed of 35 ns. This Toggle MRAM suffers from the large current required to write which limits its downsize scalability due to electromigration in the field lines.

Later, Grandis and Sony proposed the Spin Transfer Torque RAM, which utilises CIMS for writing rather than an Ampère field as for Toggle MRAM. Sony demonstrated a 4-kbit functional STT-MRAM chip [329]. They have achieved a resistance area product *RA* of 20 $\Omega \cdot \mu m^2$ and a TMR ratio of 160% with a minimum writing current of 200 μA. In 2007, Hitachi-Tohoku University have demonstrated a 2-Mbit STT-MRAM with a cell size of 1.6×1.6 μm^2 (16 F^2, F: fabrication rule), a TMR ratio of 100% and a writing current of 200 μA.

For a 1 Gbit STT-MRAM, the junction cell diameter (F) should be < 65 nm with a resistance area product (*RA*) < 30 $\Omega \cdot \mu m^2$ and a MR ratio > 100% [330]. For a 10 Gbit MRAM, the cell diameter should be reduced to be < 20 nm with *RA* < 3.5 $\Omega \cdot \mu m^2$ and a MR ratio >100%. Here, low *RA* is required to satisfy the selection transistor impedance matching [331] and low power consumption (< 100 fJ/bit). A standard MRAM architecture commercially employed is one MRAM cell connected in series with a selection transistor, where a large MR ratio (> 150%) is essential to allow for fast read-out with sufficiently low read error rate. In order to achieve these requirements, intensive investigation has been carried out on the CoFeB/MgO/CoFeB junctions. In-plane CoFeB/MgO/CoFeB MTJs have successfully satisfied the requirement for the 10 Gbit MRAM by in terms of *RA* = 0.9 $\Omega \cdot \mu m^2$ and TMR = 102% at RT [332] (as shown as open triangles with a blue fit in Fig. 14) but not in terms of thermal stability and therefore of memory retention. Driven by scalability, and taking advantage of the perpendicular magnetic anisotropy at the CoFeB/MgO interface, industrial efforts focus on perpendicularly magnetised STT-MRAM as it offers large retention and small cell footprint. Leading semiconductor industries and tool suppliers have aggressively launched their development program for STT-MRAM for either eFlash or SRAM replacement. Perpendicularly-magnetised MTJ (p-MTJ) has been investigated to achieve the requirement for the 1 Gbit MRAM with *RA* = 18 $\Omega \cdot \mu m^2$ and TMR = 124% at RT [333]. Further improvement is required to satisfy the 10 Gbit MRAM target. These MTJs under development are expected to replace the current-generation 256 Mbit MRAM with perpendicular magnetic anisotropy produced by Everspin [334]. Samsung shipped their new MRAM with a 28-nm fabrication rule for embedded-memory evaluation in March 2019 [335].

For the next-generation STT-MRAM, the following issues need to be solved: reduction of the switching critical current density (*i.e.*, reduction of power consumption) and reduction of dot-to-dot variability. Based on the scalability of the MRAM bits, CIMS must be used as discussed above. For the reduction of power consumption, the tradeoff between thermal stability of the free layer and its writability has to be optimised. A synthetic FM, such as CoFeB/Ru/CoFeB, has been implemented as the free layer, resulting in five times more thermal stability with only 80% increase in the critical current density meaning a four-fold improvement in the figure of merit Δ/I_c. This configuration can achieve a 10-Gbit MRAM device. The remaining issue to realise a high-density STT-MRAM is the reduction of the dot to dot variability which goes through process optimisation in particular concerning the etching of the magnetic stack.

In order to promote MRAM as a viable solution for high desnity memory arrays [*e.g.*, dynamic random access memory (DRAM)], several solutions for the patterning of MTJ at very narrow pitch have been proposed, either by improved etching chemistries or by unconventional strategies, such as depositing the MTJ on prepatterned pillars. A new concept to increase the downsizing, called perpendicular shape anisotropy (PSA)-STT-MRAM [101],[102] has been introduced, which consists in significantly increasing the thickness of the storage layer so as to induce a perpendicular shape anisotropy that reinforces the interfacial anisotropy. Hence, large thermal stability factors can be achieved down to sub-10 nm diameters.

A new class of magnetic memory called spin-orbit-torque (SOT)-MRAM [336] offers cache-compatible high speed and improved endurance, at the cost of larger writing currents and footprint. In order to reduce the writing current and therefore the size of the selection transistor, charge-spin conversion materials with low resistivity and large SOT efficiency must be developed. To be operated in stand-alone mode, these devices require applying a static magnetic field bias, for which several embedded solutions have been recently proposed, some demonstrated on large scale wafer [337].

Since most of the power dissipation is due to Ohmic conduction, electric field control of magnetism has been suggested as a new MRAM writing mechanism, enabling significant reduction of the energy consumption [173],[338]. As no current is needed to operate the device except during the read operation, the power consumption is reduced to the charging/discharging energy through the MTJ, which results in a very low switching energy compared with that of STT switching. Although significant results have been achieved in voltage-controlled MRAM, there are still some issues for practical use. First, VCMA with reasonable applied voltage (~ 1V) is so far too weak to be able to induce magnetisation switching while insuring sufficient magnetic thermal stability in standby. Second, the writing time window is small and size dependent, resulting in reliability issues.

Besides, like SOT, voltage control also requires an in-plane field. A promising perspective to mitigate these issues is offered by hybrid VCMA-STT combinations in 2-terminal devices or by VCMA-SOT combinations in 3-terminal MTJ devices, which enable write speed acceleration, lower current thresholds, as well as selective SOT switching of several MTJs sharing a single write line [339].

11.4. Spin-torque oscillator

By extending FMR as discussed in Section 5.2.2, microwave generation has been reported in a Co/Cu/Co GMR nanopillar under the application of STT by Kiselev *et al.* [340]. By applying a dc current into a MR nanopillar, the magnetisation in the free layer tries to switch by CIMS. However, by applying an additional magnetic field to compensate STT, the magnetisation can precess consistently, spin-torque oscillation. Here, the magnitude of the oscillation is proportional to the MR ratio [341]. Accordingly, a MgO-based MTJ has been used to demonstrate 140 nW oscillation [342].

Another critical parameter of the spin-torque oscillator (STO) is the Q-factor, which depends on the MR ratio, junction resistance, bias voltage and oscillation angle. The above MgO-based MTJ shows the Q-factor of ~ 5, indicating multiple oscillation may be induced in the nanopillar. GMR nanocontacts, on the other hand, can handle a large bias voltage, leading to the Q-factor of up to 18,000 at the oscillation frequency of 34 GHz [343]. However, the oscillation power is only 1 nW. By using a perpendicularly-magntised free layer, the Q-factor of MTJ has been reported to be 135 with maintaining 550 nW oscillation [344].

For a device application, the Q-factor and oscillation power needs to be over 100 and 1 μW, respectively. Recently, a sombrero-shaped STO has been used for the spin-torque oscillation with achieving the maximum Q-factor of 3,200 and 2.4 μW [345]. STO is hence almost ready to be implemented in a device.

11.5. Neuromorphic logic

Nanoelectronic devices, namely silicon chips, have been following Moore's law by increasing the number of transistors on a chip over the last decades. However, most of recent workloads run on a chip cannot use the entire transistors and their clusters, *i.e.*, cores, causing a problem called "dark silicon". In order to solve such inefficiency, beyond von-Neumann-type chip architecture has been sought. One of the solutions is neuromorphic computing to mimic a brain, where a neuron only sends a signal when a spike input to the neuron exceeds a threshold. The neuron can also change its form to record the input patterns. Since the pioneering work on neuromorphic computing by Mead of the California Institute of Technology in 1980, many researchers in the USA and EU have been investigating new architectures and scaling up the number of their artificial synapses (see Table 3).

Table 3 List of major neuromorphic computing projects.

Projects	Neurogrid	TrueNorth	Loihi	BrainScaleS	SpiNNaker	Biocomp
Institutes	Stanford	IBM	Intel	Heidelberg	Manchester	CNRS

Years reported	2009	2014	2017	2015	2015	2017
Technologies		CMOS	14 nm CMOS		0.5m ARM processors	MTJ
Neurons	65,536		130k	4m	100m/rack	
Synapses		286m	130m	1bn		
Energy		1/10,000	1/1,000			
References	[346]	[347]	[348]	[349]	[350]	[351]

IBM and Intel independently demonstrated neuromorphic operation of over 130 million (m) synapses. TrueNorth uses resistive random access memory (ReRAM) at 20 Hz operation, while Loihi uses static random access memory (SRAM) with over 1 GHz operation. They also achieved over three orders of magnitude reduction in their energy consumption as compared to the current CMOS technology. In parallel, the European Union (EU) initiated the Human Brain Project by funding the BrainScaleS [349] and SpiNNaker [350] projects. The BrainScaleS system is based in Heidelberg employing silicon-based analogue electronics to model four million neurons and one billion (bn) synapses. The system runs 10,000 times faster than its biological archetype. The SpiNNaker system, on the other hand, is based in Manchester using parallel computing. It planned to use one million ARM processors. These artificial synapses are all based on the current Si-based CMOS technology, which is advantageous from the viewpoints of their fabrication and implementation but with less robustness under extreme conditions, *e.g.*, high temperature use and radiation exposure, as compared with metal-based chips.

On contrary, another European project, Biocomp [351], utilises voltage-tuneable nano-resistance in a metallic MTJ, which has also been studied by Tohoku University in Japan [352]. Their concept is to utilise resistance changes in a current-induced magnetisation reversal process and to control them by taking a “minor” loop in the process. Here, the data is stored as a magnetisation direction in one of the ferromagnetic layers in a MTJ, which can be reversed by applying a current. Phase-synchronisation of a vortex-type STO array has also been demonstrated [353]. Up to eight STOs are used to demonstrate long-term stability of the phase difference better than 1.6 ms and the noise power spectral density of phase difference of – 80 dBc/Hz at 1 kHz offset frequency

Recently, probabilistic magnetisation reversal has also been used for stochastic computation [354]. An array of MTJ consisting of CoFeB/MgO/CoFeB has been employed to demonstrate the factorisation of integers up to 945. Similar chaotic behaviour has been reported in a vortex oscillator with a nano-contact up to 1.5 GHz [355]. Such a computational method can bridge between the conventional and quantum computations with low energy consumption.

11.6. Racetrack memory

Following Slonczewski [43] and Berger [88], STT concept has also been applied to displace DW by flowing an electrical current through DW. DW displacement as discussed in Section 3.1.4 can also be used to produce a racetrack memory as a high density shift register memory as shown in Fig. 17 [356],[357]. This racetrack memory, originally proposed by Parkin, potentially extends a device structure into a 3D configuration. In a racetrack memory, information is stored in the form of DWs along magnetic racetracks on a wafer. DWs are caused to move in synchronism around the racetracks by applying spin-polarised current pulses. Information is written by a domain injection pad and read by a spin tunnel junction at the end of the wire. This technology accommodates multiple magnetic DWs per racetrack, and the spacing between consecutive magnetic DWs that defines the bit length is controlled by pinning sites formed from notches along the racetrack [358].

Experimentally, DWs need to be pinned at precise positions following the wall motion is induced by a current. A FM micro-wire has been prepared with DW, giving a current density between 10^7 and 10^8 A/cm^2 for the wall motion [359],[360]. The velocity of the wall motion has also been estimated to be (2 ~ 6) m/s [108]. A similar experiment has also been performed in a DMS wire [361],[362]. Since a vortex-like component in the wall can induce random movement of the wall after the current injection, a step-like motion is required for memory applications. Wall motion at a speed of 100 m/s under a current density of 2×10^8 A/cm^2 has been achieved [363],[364]. This type of DW motion has been implemented into an MRAM device to switch the magnetisation in the free layer of a bit, which has been demonstrated by NEC with a wall separation of 45 to 60 nm [365]. Recently, much faster speed up to 750 m/s were achieved in synthetic antiferromagnetic wires with perpendicular anisotropy [366].

In order to achieve fast read/write operation, the DW motion dependent upon the current-pulse width has been studied [367],[368]. Thomas *et al.* have observed amplification of the DW oscillation even after the pulsed current injection. By carefully matching the time constants of these phenomena, they have reported a possibility of reducing the critical current density for DW motion using numerical calculations. During the DW motion, complex oscillatory motions can occur depending on the shape of the vortex components of DW [369]. By tuning the current pulse, coherent and reproducibly smooth motion of DW has been achieved.

In order to realise the racetrack memory, micro- or nanometre wide FM wire needs to be fabricated either with very smooth edge, which ensures uniform DW displacement, or with periodical DW traps at the edge. To extend the racetrack concept to 3D, it would be important to fabricate these wires in the shape of "U" figure as shown in Fig. 17. These requirements are very severe to the current nanofabrication techniques.

The remaining key issues for memory application is to fabricate reproducible DW pinning with uniform pinning strength and reasonable density. Initial RM concept uses a series of notches for pinning, which suffers from the broad distributions in their shapes by nanofabrication, resulting in the broad distributions in their pinning strength and the corresponding critical current densities for their displacement. Comb-shapes have then been used as an alternative but they cannot provide uniform pinning fields either [370]. For RM using a DMS wire, thickness steps can act as pinning sites but with a limited number [361]. Exchange bias has been demonstrated to be employed as DW pinning by simply depositing additional AF nanowires across the FM nanowire [371]. The exchange bias fields, which directly determine the pinning strendth, can be controlled by the setting conditions at the AF/FM interfaces. Such interfaces can be fabricated using photolithography. Similar configuration can be achieved by metal diffusion at the desired location of the DW pinning centres [372].

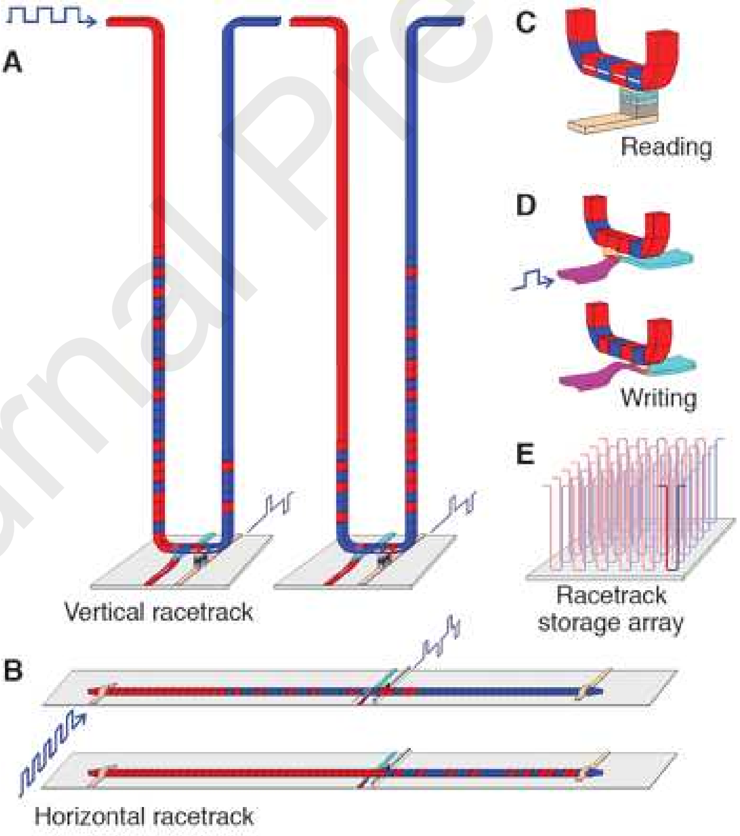

Fig. 17 Schematic diagram of a racetrack memory concept in (A) vertical and (B) horizontal configurations. (C) Reading and (D) writing operation can be carried out electrically. (E) 3D-array concept [368].

Instead of DW as a memory bit, a magnetic skyrmion, which is a topologically stable entity in FM via DMI, can be used for RM. The comparison between these two quasi-particles are shown in Table 4, showing the advantages of skyrmions [373]. However, they also have disadvantages, including easy pinning outside pinning positions, unstability at RT (collapsing) and sideway motion. The dynamics of a skyrmion can be determined by the competition of adiabatic and non-adiabatic STT terms [374]. Figure 18 shows a simulater result of a skyrmion moving at the speed of 20 m/s with the adiabatic and non-adiabatic terms to be $\alpha = 0.1$ and $\beta = 0.1$.

Table 4 Comparison between skyrmions and DWs.

	Skyrmions	DWs
Size [nm]	10 ~ 50	20 ~ 50
Speed [m/s]	~ 100	~ 500 ~ 750
Critical current [A/cm]	10^2	~ 10^7

The skyrmion motion has been demonstrated in a multilayer of Ta/CoFeB/Ta-O at the speed of ~ 10 m/s at RT [375]. Further increase in the speed > 100 m/s has then be achieved in Pt/CoFeB/MgO [376] and magnetically symmetric structures [377]. Using such current-induced skyrmion motion, skyrmion logic has been proposed and demonstrated [378]. Using a “Y”-shaped wire, both AND and OR operation has been demonstrated. In addition, the size of the skyrmions can be controlled by applied magnetic field [154]. These devices use one of the characteristics of the skyrmion, polarity. However, skyrmion has another property, chirality. Nakatani *et al.* have reported the skyrmion logic using the chirality [379]. It was shown that the chirality of the skyrmion can be controlled by a pulse heat spot by simulation.

Fig. 18 Simulated Boloch-type skyrmion motion by an electrical current (animation).

11.7. Spin-polarised field effect transistor

In order to realise a spin-FET, the modulation of spin-polarised electrons accumulated in the semiconductor material needs to be achieved. The spin-orbit interaction Hamiltonian can be derived from the Dirac equations [380]:

$$H_{\mathrm{SO}} = \frac{q\hbar^2}{4m^2c^2}\left(\vec{\boldsymbol{\sigma}} \cdot \left[\vec{\boldsymbol{E}} \times \vec{\boldsymbol{p}}\right]\right), \tag{19}$$

where q, $\hbar$, m, c, $\vec{\boldsymbol{\sigma}}$, $\vec{\boldsymbol{E}}$ and $\vec{\boldsymbol{p}}$ are the electron charge, Planck constant, electron mass, speed of light, Pauli matrices, electric field and electron momentum, respectively. By comparison with the Rashba Hamiltonian $H_\mathrm{R} = \eta_\mathrm{SO}(\vec{\boldsymbol{\sigma}} \times \vec{\boldsymbol{k}}) \cdot \vec{\boldsymbol{v}}$ ($\vec{\boldsymbol{k}}$: wave vector and $\vec{\boldsymbol{v}}$: unit vector perpendicular to plane),

$$H_\mathrm{R} = \frac{q\hbar^2}{4m^2c^2}\left(\vec{\boldsymbol{\sigma}} \cdot \left[\vec{\boldsymbol{E}} \times \vec{\boldsymbol{p}}\right]\right) = \frac{q\hbar^2}{4m^2c^2}\frac{V_\mathrm{G}}{d}\left(\vec{\boldsymbol{\sigma}} \times \vec{\boldsymbol{k}}\right) \cdot \vec{\boldsymbol{v}}. \quad (20)$$

(i) Electric field operation

Therefore, the spin-orbit interaction constant η_SO can be obtained by using a gate voltage V_G and distance between an electron path and a gate length d:

$$\eta_\mathrm{SO} = \frac{q\hbar^2}{4m^2c^2}\frac{V_\mathrm{G}}{d}. \quad (21)$$

For commonly-used InGaAs 2DEG, a 180º phase shift can be achieved for a separation between an injector and a detector: $l = \Delta\theta\hbar^2/2m^*\eta_\mathrm{SO} \approx$ 3 μm, and gate length: $w = \hbar^2/2m^*\eta_\mathrm{SO} \approx$ 1 μm. The corresponding electric field required is estimated to be $V_\mathrm{G}/d = 4{m^*}^2c^2\eta_\mathrm{SO}/q\hbar^2 \approx$ 4.3 × 10^{10} V/m, where m^* is the electron effective mass. This provides d ~ 1 nm and V_G ~ 43 V, which are very difficult to realise with present nano-fabrication techniques and requires a further improvement of the spin-orbit interaction constant η_SO to achieve a realistic spin transistor. Experimentally, electrical field operation has been demonstrated in a InAs QW with achieving a spin rotation over a distrance of 0.54 μm [381], which is not suitable for device-level miniaturisation.

(ii) Magnetic field operation

Instead of an electric field, a magnetic field can be used as an electromagnetic gate. As a demonstration, a lateral spin-valve structure has been fabricated using a non-magnetic Cu nano-ring in order to split the diffusive spin-current path for operation [382]. By providing Larmor precession independently onto each spin path with respect to the distance from a dc current path, the dc current introduces a perpendicular Ampère field and acts as a gate in a three-terminal device. Successful spin-current modulation is demonstrated in a non-local signal, which is 30% more effective than that expected from the conventional simple Larmor precession, *i.e.*, the Hanle effect. This is predominantly due to the shorter oscillation period observed as a result of arithmetic operation of the spin currents. The same modulation can also be applied to a SC nano-ring for magnetic-field operation. It is therefore important to minimise the device dimensions to operate a spin-polarised electron current effectively.

(iii) Optical operation

Circularly polarised light can also be used as a gate for a nano-spin motor [383]. A variable wavelength continuous-wave laser with a photo-elastic modulator was used to introduce a circularly polarised beam to a non-local Fe/*n*-GaAs device. Time-resolved Kerr rotation technique was employed to obtain the *n*-GaAs excitation wavelength (822 nm), the spin dephasing time (2.9 ns), and the electron *g*-factor (– 0.43). In order to test the feasibility of optical gating, the circularly polarised beam has been illuminated to the region of pure spin current between the injector and the detector ferromagnets, while observing the changes in the non-local voltage so that the spin-FET-type operation can be verified. The linear increase of the non-local voltage with the laser power is observed, which can be accounted to both heating and photoexcitation. However, there are no significant changes between the circularly polarised and the unpolarised lights, which suggests that the observed increase can be solely from the magnetic circular dichroism. The optical gating technique is expected to have significant advantages over conventional electric and magnetic field operation due to a lower power consumption of at least 25%.

11.8. Spin-polarised light emitting diode and laser

Circularly polarised light emission was initially studied in a InGaAs QW structure (QW) [384]. A vertical cavity surface emitting laser (VCSEL) was fabricated with circular polarisation in Voigt geometry, showing 35 mW power under a magnetic field of 20 kOe. The VCSEL operation was then demonstrated both by optical and electrical injection [385]. By optimising the structure to reduce spin–orbit coupling, just a 4% spin polarisation of injected carriers led to a nearly complete (96%) polarisation of emitted light reported with a QW-VCSEL, demonstrating that such lasers can be highly efficient spin filters and spin amplifiers, as predicted theoretically [386]. The behaviour of the spin lasers was analysed by the bucket model [387]. The model offers a way to design a desirable spin laser for both QW and QD configurations. Spin-injection modulation was also demonstrated to be able to eliminate parasitic frequency modulation (chirp) and to enhance the modulation bandwidth [388], improving the two key parameters in lasers. The operation frequency can be over 11 GHz, which is highly advantageous for future spintronic communications via circularly polarised light at RT [389]. The mechanism of VCSEL can also be described using a spin-flip model [390]. Elliptically polarised fields are investigated and the spin polarisation is determined by the initial pump power.

These spin-polarised lasers are limited by their constituent materials. Recently, Fe_3O_4 nanoparticles dispersed on GaN nanorods have been reported to emit spin-polarised laser with spin polarisation up to 28.2% at RT under a low magnetic field of 3.5 kOe [391]. This emission is induced by the selective charge transfer of electrons with opposite spins at the

Fe_3O_4/GaN interfaces. Similar laser emission may be realised using a wide range of materials.

12. Future Perspectives

Spin-electronics is at the verge of becoming a mainstream technology in microelectronics. The launch of magnetic memory production in 2018 at major microelectronic foundries marks the adoption of spintronics by microelectronics industry. This decisive step has now been passed and lot of further developments should yield to new applications of spintronic phenomena and devices.

In particular, the following items should be considered for further improvements or new directions in spintronic device applications:

(i) Development of low-power electronics by taking an advantage of non-volatility of magnetic based devices and electric field writing. This requires the development of materials with larger VCMA coefficient, the develomment of RT multiferroic material integrable in MTJ with large TMR and CMOS compatible or of the other materials sensitive to an electric field such as magnetic semiconductors which could operate at RT.

(ii) Low power read-out using spin-orbit phenomena rather than tunnel magnetoresistance.

(iii) Innovative circuits architecture taking full advantage of spintronic phenomena, materials and devices (*e.g.*, in memory computing, normally-off/instant-on architecture).

(iv) Unconventional computing using spintronic devices (*e.g.*, stochastic computing).

(v) Innovative magnetic field sensors with increased sensitivity, reduced temperature dependence, or broader field dynamics for all kinds of applications from position encoders to medical diagnosis or HDD read-heads.

(vi) Coupling of photonics and nanomagnetism/spintronics in relation with the development of optical interconnects in electronics and all optical writing in storage technology.

(vii) 3D spintronic embodiments for high-density memory and storage devices.

(viii) Energy harvesting from thermal gradients via spincaloritronics or electromagnetic radiations using spin-diodes.

(ix) Development of artificial neurones and synpases for artificial intelligence based on spintronic devices.

(x) Spintronic devices optimised for low-temperature operation for quantum engineering or large scale computers.

Acknowledgements

The authors would like to thank the financial support by JST-EC DG RTD Coordinated research project (FP7-NMP3-SL-2013-604398), EPSRC-JSPS Core-to-Core programme (EP/M02458X/1) and JST CREST (JPMJCR17J5). The UK team has been supported by EPSRC grants (EP/I000933/1 and EP/K03278X/1), Royal Society research grant and International Collaboration Center of the Institute for Materials Research at Tohoku University. B.D. acknowledges support from ERCEA via ERC MAGICAL 669204. B.H. acknowledges financial support by the Deutsche Forschungsgemeinschaft (SFB/TRR 173 "Spin + X", Project B01).

References

[1] https://www.statista.com/statistics/398951/global-shipment-figures-for-hard-disk-drives/

[2] https://www.grandviewresearch.com/industry-analysis/permanent-magnets-industry

[3] https://www.statista.com/statistics/266973/global-semiconductor-sales-since-1988/

[4] J. E. Lilienfeld, *US Patent 1,745,175* (1926).

[5] https://ethw.org/Milestones:Invention_of_the_First_Transistor_at_Bell_Telephone_Laboratories,_Inc.,_1947

[6] A. V. Chumak, V. I. Vasyuchka, A. A. Serga and B. Hillebrands, *Nat. Phys.* **11**, 453 (2015).

[7] A. A. Serga, A. V. Chumak and B. Hillebrands, *J. Phys. D: Appl. Phys.* **43**, 264002 (2010).

[8] A. Hubert and R. Schäfer, *Magnetic Domains* (Springer, Berlin, Germany, 1998).

[9] A. Hirohata and K. Takanashi, *J. Phys. D: Appl. Phys.* **47**, 193001 (2014).

[10] A. Fujiwara and Y. Takahashi, *Nature* **410**, 560 (2001).

[11] S. Maekawa *et al.* (*Eds.*), *Spin Current* (Oxford University Press, Oxford, 2017).

[12] A. Hirohata, *Frontiers in Physics* **6**, 23 (2018).

[13] E. Lesne, Y. Fu, S. Oyarzun, J. C. Rojas-Sánchez, D. C. Vaz, H. Naganuma, G. Sicoli, J.-P. Attané, M. Jamet, E. Jacquet, J.-M. George, A. Barthélémy, H. Jaffrès, A. Fert, M. Bibes and L. Vila, *Nat. Mater.* **15**, 1261 (2016).

[14] T. Kimura, N. Hashimoto, S. Yamada, M. Miyao and K. Hamaya, *NPG Asia Mater.* **4**, e9 (2012).

[15] W. H. Butler, X.-G. Zhang, T. C. Schulthess and J. M. MacLaren, *Phys. Rev B* **63**, 054416 (2001).

[16] J. Mathon and A. Umerski, *Phys. Rev. B* **63**, 220403(R) (2001).

[17] M.-H. Nguyen, M. Zhao, D. C. Ralph and R. A. Buhrman, *Appl. Phys. Lett.* **108**, 242407 (2016).

[18] K. Kondou, R. Yoshimi, A. Tsukazaki, Y. Fukuma, J. Matsuno, K. S. Takahashi, M. Kawasaki, Y. Tokura and Y. Otani, *Nat. Phys.* **12**, 1027 (2016).

[19] M. Konig, S. Wiedmann, C. Brüne, A. Roth, H. Buhmann, L. W. Molenkamp, X.-L. Qi and S.-C. Zhang, *Science* **318**, 766 (2007).

[20] H. Ohno, D. Chiba, F. Matsukura, T. Omiya, E. Abe, T. Dietl, Y. Ohno and K. Ohtani, *Nature* **408**, 944 (2000).

[21] T. Tashiro, S. Matsuura, A. Nomura, S. Watanabe, K. Kang, H. Sirringhaus and Kazuya Ando, *Sci. Rep.* **5**, 15158 (2015).

[22] H. Munekata, H. Ohno, S. von Molnar, Armin Segmüller, L. L. Chang and L. Esaki, *Phys. Rev. Lett.* **63**, 1849 (1989).

[23] A. Kirihara, K. Kondo, M. Ishida, K. Ihara, Y. Iwasaki, H. Someya, A. Matsuba, K. Uchida, E. Saitoh, N. Yamamoto, S. Kohmoto and T. Murakami, *Sci. Rep.* **6**, 23114 (2016).

[24] D. Loss and P. M. Goldbart, *Phys. Rev. B* **45**, 13544 (1992).

[25] J. Bass, *J. Magn. Magn. Mater.* **408**, 244 (2016).

[26] K. Yasuda, A. Tsukazaki, R. Yoshimi, K. Kondou, K. S. Takahashi, Y. Otani, M. Kawasaki and Y. Tokura, *Phys. Rev. Lett.* **119**, 137204 (2017).

[27] M. Jullière, *Phys. Lett. A* **54**, 225 (1975).

[28] M. N. Baibich, J. M. Broto, A. Fert, F. Nguyen Van Dau, F. Petroff, P. Etienne, G. Creuzet, A. Friederich and J. Chazelas, *Phys. Rev. Lett.* **61**, 2472 (1988).

[29] G. Binasch, P. Grünberg, F. Saurenbach and W. Zinn, *Phys. Rev. B* **39**, 4828(R) (1989).

[30] M. Johnson, *Phys. Rev. Lett.* **67**, 3594 (1993).

[31] S. A. Wolf, D. D. Awshalom, R. A. Buhrman, J. M. Daughton, S. von Molnár, M. L. Roukes, A. Y. Chtchelkanova and D. M. Treger, *Science* **294**, 1488 (2001).

[32] T. Miyazaki and N. Tezuka, *J. Magn. Magn. Mater.* **139**, L231 (1995).

[33] J. S. Moodera, L. R. Kinder, T. M. Wong and R. Meservey, *Phys. Rev. Lett.* **74**, 3273 (1995).

[34] H. X. Wei, Q. H. Qin, M. Ma, R. Sharif and X. F. Han, *J. Appl. Phys.* **101**, 09B501 (2007).

[35] S. S. P. Parkin, C. Kaiser, A. Panchkula, P. M. Rice, B. Hughes, M. Samant and S.-H. Yang, *Nat. Mater.* **3**, 862 (2004).

[36] S. Yuasa, T. Nagahama, A. Fukushima, Y. Suzuki and K. Ando, *Nat. Mater.* **3**, 868 (2004).

[37] S. Ikeda, J. Hayakawa, Y. Ashizawa, Y. M. Lee, K. Miura, H. Hasegawa, M. Tsunoda, F. Matsukura and H. Ohno, *Appl. Phys. Lett.* **93**, 082508 (2008).

[38] S. S. P. Parkin, Z. G. Li and D. J. Smith, *Appl. Phys. Lett.* **58**, 2710 (1991).

[39] J. W. Jung, Y. Sakuraba, T. T. Sasaki, Y. Miura and K. Hono, *Appl. Phys. Lett.* **108**, 102408 (2016).

[40] U. Hartmann (*Ed.*), *Magnetic Multilayers and Giant Magnetoresistance* (Springer, Berlin, 2000).

[41] P. M. Levy, *Solid State Phys.* **47**, 367 (1994).

[42] T. Valet and A. Fert, *Phys. Rev. B* **48**, 7099 (1993).

[43] S. Datta and B. Das, *Appl. Phys. Lett.* **56**, 665 (1990).

[44] G. Schmidt, D. Ferrand, L. W. Molenkamp, A. T. Filip and B. J. van Wees, *Phys. Rev. B* **62**, R4790 (2000).

[45] H. X. Tang, F. G. Monzon, R. Lifshitz, M. C. Cross and M. L. Roukes, *Phys. Rev. B* **61**, 4437 (2000).

[46] E. I. Rashba, *Phys. Rev. B* **62**, 16267 (2000).

[47] P. R. Hammar, B. R. Bennet, M. J. Yang and M. Johnson, *Phys. Rev. Lett.* **83**, 203 (1999).

[48] H. X. Tang, F. G. Monzon, R. Lifshitz, M. C. Cross and M. L. Roukes, *Phys. Rev. B* **61**, 4437 (2000).

[49] A. T. Filip, B. H. Hoving, F. J. Jedema, B. J. van Wees, B. Dutta and S. Borghs, *Phys. Rev. B* **62**, 9996 (2000).

[50] P. Kotissek, M. Bailleul, M. Sperl, A. Spitzer, D. Schuh, W. Wegscheider, C. H. Back and G. Bayreuther, *Nat. Phys.* **3**, 872 (2007).

[51] O. Wunnicke, P. Mavropoulos, R. Zeller and P. H. Dederichs, *Phys. Rev. B* **65**, 241306(R) (2002).

[52] S. A. Crooker, M. Furis, X. Lou, C. Adelmann, D. L. Smith, C. J. Palmstrøm and P. A. Crowell, *Science* **309**, 2191 (2005).

[53] S. Honda, H. Itoh, J. Inoue, H. Kurebayashi, T. Trypiniotis, C. H. W. Barnes, A. Hirohata and J. A. C. Bland, *Phys. Rev. B* **78**, 245316 (2008).

[54] L. R. Fleet, K. Yoshida, H. Kobayashi, Y. Kaneko, S. Matsuzaka, Y. Ohno, H. Ohno, S. Honda, J. Inoue and A. Hirohata, *Phys. Rev. B* **87**, 024401 (2013).

[55] H. J. Zhu, M. Ramsteiner, H. Kostial, M. Wassermeier, H.-P. Schönher and K. H. Ploog, *Phys. Rev. Lett.* **87**, 016601 (2001).

[56] A. T. Hanbicki, B. T. Jonker, G. Itskos, G. Kioseoglou and A. Petrou, *Appl. Phys. Lett.* **80**, 1240 (2002).

[57] S. A. Crooker, M. Furis, X. Lou, C. Adelmann, D. L. Smith, C. J. Palmstrøm and P. A. Crowell, *Science* **309**, 2191 (2005).

[58] O. H. J. van't Erve, G. Kioseoglou, A. T. Hanbicki, C. H. Li, B. T. Jonker, R. Mallory, M. Yasar and A. Petrou, *Appl. Phys. Lett.* **84**, 4334 (2004).

[59] R. Wang, X. Jiang, R. M. Shelby, R. M. Macfarlane, S. S. P. Parkin, S. R. Bank and J. S. Harris, *Appl. Phys. Lett.* **86**, 052901 (2005).

[60] X. Jiang, R. Wang, R. M. Shelby, R. M. Macfarlane, S. R. Bank, J. S. Harris and S. S. P. Parkin, *Phys. Rev. Lett.* **94**, 056601 (2005).

[61] I. Žutić, J. Fabian and S. C. Erwin, *Phys. Rev. Lett.* **97**, 026602 (2006).

[62] B.-C. Min, K. Motohashi, J. C. Lodder and R. Jansen, *Nat. Mater.* **5**, 817 (2006).

[63] B. T. Jonker, G. Kioseoglou, A. T. Hanbicki, C. H. Li and P. E. Thompson, *Nat. Phys.* **3**, 542 (2007).

[64] E. Shikoh, K. Ando, K. Kubo, E. Saitoh, T. Shinjo and M. Shiraishi, *Phys. Rev. Lett.* **110**, 127201 (2013).

[65] F. J. Jedema, A. T. Filip and B. J. van Wees, *Nature* **410**, 345 (2000).

[66] F. J. Jedema, H. B. Heersche, A. T. Filip, J. J. A. Baselmans and B. J. van Wees, *Nature* **416**, 713 (2002).

[67] T. Kimura, J. Hamrle, Y. Otani, K. Tsukagoshi and Y. Aoyagi, *Appl. Phys. Lett.* **85**, 3501 (2004).

[68] S. Garzon, I. Žutić and R. A. Webb, *Phys. Rev. Lett.* **94**, 176601 (2005).

[69] T. Kimura, Y. Otani and J. Hamrle, *Phys. Rev. B* **73**, 132405 (2006).

[70] R. Godfrey and M. Johnson, *Phys. Rev. Lett.* **96**, 136601 (2006).

[71] T. Kimura, N. Hashimoto, S. Yamada, M. Miyao and K. Hamaya, *NPG Asia Mater.* **4**, e9 (2012).

[72] K. Tsukagoshi, B. W. Alphenaar and H. Ago, *Nature* **401**, 572 (1999).

[73] L. E. Hueso, J. M. Pruneda, V. Ferrari, G. Burnell, J. P. Valdés-Herrera, B. D. Simons, P. B. Littlewood, E. Artacho, A. Fert and N. D. Mathur, *Nature* **445**, 410 (2007).

[74] N. Tombros, C. Jozsa, M. Popinciuc, H. T. Jonkman and B. J. van Wees, *Nature* **448**, 571 (2007).

[75] B. Dlubak, M.-B. Martin, C. Deranlot, B. Servet, S. Xavier, R. Mattana, M. Sprinkle, C. Berger, W. A. De Heer, F. Petroff, A. Anane, P. Seneor and A. Fert, *Nat .Phys.* **8**, 557 (2012).

[76] Z. H. Xiong, D. Wu, Z. V. Vardeny, J. Shi, *Nature* **427**, 821 (2004).

[77] M. Cinchetti, K. Heimer, J. Wüstenberg, O. Andreyev, M. Bauer, S. Lach, C. Ziegler, Y. Gao and M. Aeschlimann, *Nat. Mater.* **8**, 115 (2009).

[78] L. Landau and E. Lifshitz, *Physik A (Soviet Union)* **8**, 135 (1935).

[79] T. L. Gilbert, *IEEE Trans. Magn.* **40**, 3443 (2004).

[80] N. F. Mott and H. S. W. Massey, *The Theory of Atomic Collisions* (Third Edition) (Oxford University Press, Oxford, 1965).

[81] M. D’yakonov and V. Perel, *Sov. Phys. Sol. State* **13**, 3023 (1972).

[82] R. J. Elliott, *Phys. Rev.* **96**, 266 (1954).

[83] Y. Yafet, *Sol. State Phys.* **14**, 1 (1963).

[84] V. Kamberskỳ, *Can. J. Phys.* **48**, 1103 (1970).

[85] V. Koreman and R. E. Prange, *Phys. Rev. B* **6**, 2769 (1972).

[86] J. Kuneš and V. V. Kamberskỳ, *Phys. Rev. B* **65**, 212411 (2002).

[87] J. Slonczewski, *J. Magn. Magn. Mater.* **159**, L1 (1996).

[88] L. Berger, *Phys. Rev. B* **54**, 9353 (1996).

[89] A. Thiaville, Y. Nakatani, J. Miltat and Y. Suzuki, *Europhys. Lett.* **69**, 990 (2005).

[90] V. Vlaminck and M. Bailleul, *Science* **322**, 410 (2008).

[91] F. J. Albert, J. Katine, R. A. Buhrmn and D. C. Ralph, *Appl. Phys. Lett.* **77**, 3809 (2000).

[92] J. Bass, *J. Magn.Magn. Mater.* 408, 244 (2016).

[93] Y. Jiang, S. Abe, T. Ochiai, T. Nozaki, A. Hirohata, N. Tezuka and K. Inomata, *Phys. Rev. Lett.* **92**, 167204 (2004).

[94] Y. Jiang, T. Nozaki, S. Abe, T. Ochiai, A. Hirohata, N. Tezuka and K. Inomata, *Nat. Mater.* **3**, 361 (2004).

[95] T. Yang, A. Hirohata, T. Kimura and Y. Otani, *Phys. Rev. B* **74**, 153301 (2006).

[96] D. J. Monsma, J. C. Lodder, Th. J. A. Popma and B. Dieny, *Phys.Rev Lett.* **74**, 5260 (1995).

[97] C. Vautrin, D. Lacour, G. Sala, Y. Lu, F. Montaigne and M. Hehn, *Phys. Rev. B* **96**,174426 (2017).

[98] G. D. Fuchs, N. C. Emley, I. N. Krivorotov, P. M. Braganca, E. M. Ryan, S. I. Kiselev, J. C. Sankey, D. C. Ralph, R. A. Buhrman and J. A. Katine, *Appl. Phys. Lett.* **85**, 1205 (2004).

[99] H. Kubota, A. Fukushima, Y. Ootani, S. Yuasa, K. Ando, H. Maehara, K. Tsunekawa, D. D. Djayaprawira, N. Watanabe and Y. Suzuki, *Jpn. J. Appl. Phys.* **44**, L1237 (2005).

[100] J. Hayakawa, S. Ikeda, Y. M. Lee, R. Sasaki, T. Meguro, F. Matsukura. H. Takahashi and H. Ohno, *Jpn. J. Appl. Phys.* **44**, L1267 (2005).

[101] K. Watanabe, B. Jinnai, S. Fukami, H. Sato and H. Ohno, *Nat. Commun.* **9**, 663 (2018).

[102] N. Perrissin, S. Lequeux, N. Strelkov, A. Chavent, L. Vila, L. D. Buda-Prejbeanu, S. Auffret, R. C. Sousa, I. L. Prejbeanu and B. Dieny, *Nanoscale* **10**, 12187 (2018).

[103] S. Ikeda, K. Miura, H. Yamamoto, K. Mizunuma, H.D. Gan, M. Endo, S. Kanai, J. Hayakawa, F. Matsukura and H. Ohno, *Nat. Mater.* **9**, 721 (2010).

[104] B. Dieny and M. Chshiev, *Rev. Mod. Phys.* **89**, 025008 (20017).

[105] F. Greulet, C. Tiusan, F. Montaigne, D. Hehn, D. Halley, O. Bengone, M. Bowen and W. Weber, *Phys.Rev Lett.* **99**, 187202 (2007).

[106] B. S. Tao, H. X. Yang, Y. L. Zuo, X. Devaux, G. Lengaigne, M. Hehn, D. Lacour, S. Andrieu, M. Chshiev, T. Hauet, F. Montaigne, S. Mangin, X. F. Han and Y. Lu, *Phys. Rev. Lett.* **115**, 157204 (2015).

[107] B. Tao, C. Wan, P. Tang, J. Feng, H. Wei, X. Wang, S. Andrieu, H. Yang, M. Chshiev, X. Devaux, T. Hauet, F. Montaigne, S. Mangin, M. Hehn, D. Lacour, X. Han and Y. Lu, *Nano. Lett.* **19**, 3019 (2019).

[108] A. Yamaguchi, T. Ono, S. Nasu, K. Miyake, K. Mibu and T. Shinjo, *Phys. Rev. Lett.* **92**, 077205 (2004).

[109] N. L. Schryer and L. R. Walker, *J. Appl. Phys.* **45**, 5406 (1974).

[110] S. Emori. and G. S. D. Beach, *J. Phys. Condens. Matter.* **24**, 024214 (2012).

[111] A. Mougin, M. Cormier, J. P. Adam, P. J. Metaxas and J. Ferré, *Euro. Phys. Lett.* **78**, 57007 (2007).

[112] M. I. Dyakonov and V. I. Perel, *Phys. Lett. A* **35**, 459 (1971).

[113] J. E. Hirsch, *Phys. Rev. Lett.* **83**, 1834 (1999).

[114] J. N. Chazalviel and I. Solomon, *Phys. Rev. Lett.* **29**, 1676 (1972).

[115] J.-N. Chazalviel, *Phys. Rev. B* **11**, 3918 (1975).

[116] Y. K. Kato, R. C. Myers, A. C. Gossard and D. D. Awschalom, *Science* **306**, 1910 (2004).

[117] S. O. Valenzuela and M. Tinkham, *Nature* **442**, 176 (2006).

[118] T. Seki, Y. Hasegawa, S. Mitani, S. Takahashi, H. Imamura, S. Maekawa, J. Nitta and K. Takanashi, *Nat. Mater.* **7**, 125 (2008).

[119] J. Wunderlich, A. C. Irvine, J. Sinova, B. G. Park, X. L. Xu, B. Kaestner, V. Novák and T. Jungwirth, *Nat. Phys.* **5**, 675 (2009).

[120] C.-Z. Chang and M. Li, *J. Phys.: Condens. Matter* **28**, 123002 (2016).

[121] C.-Z. Chang, J. Zhang, X. Feng, J. Shen, Z. Zhang, M. Guo, K. Li, Y. Ou, P. Wei, L.-L. Wang, Z.-Q. Ji, Y. Feng, S. Ji, X. Chen, J. Jia, X. Dai, Z. Fang, S.-C. Zhang, K. He, Y. Wang, L. Lu, X.-C. Ma and Q.-K. Xue, *Science* **340**, 167 (2016).

[122] S. Fukami, T. Anekawa, C. Zhang and H. Ohno, *Nat. Nanotechnol.* **11**, 621 (2016).

[123] C. Gould, C. Rüster, T. Jungwirth, E. Girgis, G. M. Schott, R. Giraud, K. Brunner, G. Schmidt and L. W. Molenkamp, *Phys. Rev. Lett.* **93**, 117203 (2004).

[124] J. Moser, A. Matos-Abiague, D. Schuh, W. Wegscheider, J. Fabian and D. Weiss, *Phys. Rev. Lett.* **99**, 056601 (2007).

[125] B. G. Park, J. Wunderlich, D. A. Williams, S. J. Joo, K. Y. Jung, K. H. Shin, K. Olejník, A. B. Shick and T. Jungwirth, *Phys. Rev. Lett.* **100**, 087204 (2008).

[126] L. Gao, X. Jiang, S.-H. Yang, J. D. Burton, E. Y. Tsymbal and S. S. P. Parkin, *Phys. Rev. Lett.* **99**, 226602 (2007).

[127] L. Néel, *Annales de Physique* **3**, 137 (1948).

[128] C. G. Shull and J. S. Smart, *Phys. Rev.* **76**, 1256 (1949).

[129] P. W. Anderson, *Phys. Rev.* **79**, 350 (1950).

[130] W. H. Meiklejohn and C. P. Bean, *Phys. Rev.* **105**, 904 (1957).

[131] R. E. Fontana, Jr., B. A. Gurney, T. Lin, V. S. Speriosu, C. H. Tsang and D. R. Wilhoit, *U. S. Patent* 5,701,223 (1997).

[132] T. Jungwirth, X. Marti, P. Wadley and J. Wunderlich, *Nat. Nanotech.* **11**, 231 (2016).

[133] V. Baltz, A. Manchon, M. Tsoi, T. Moriyama, T. Ono and Y. Tserkovnyak, *Rev. Mod. Phys.* **90**, 015005 (2018).

[134] A. S. Núñez, R. A. Duine, P. M. Haney and A. H. MacDonald, *Phys. Rev. B* **73**, 214426 (2006).

[135] Z. Wei, A. Sharma, A. Nunez, P. M. Haney, R. A. Duine, J. Bass, A. H. MacDonald and M. Tsoi, *Phys. Rev. Lett.* **98**, 116603 (2007).

[136] H. V. Gomonay and V. M. Loktev, *Phys. Rev. B* **81**, 144427 (2010).

[137] R. Cheng, D. Xiao and A. Brataas, *Phys. Rev. Lett.* **116**, 207603 (2016).

[138] C. Tzschaschel, T. Satoh and M. Fiebig, *Nat. Commun.* **10**, 3995 (2019)

[139] S. Takei, T. Moriyama, T. Ono and Y. Tserkovnyak, *Phys. Rev. B* **92**, 020409 (2015).

[140] C. Sürgers, G. Fischer, P. Winkel and H.V. Löhneysen, *Nat. Commun.* **5**, 3400 (2014).

[141] S. Nakatsuji, N. Kiyohara and T. Higo, *Nature* **527**, 212 (2015).

[142] J. B. S. Mendes, R. O. Cunha, O. Alves Santos, P. R. T. Ribeiro, F. L. A. Machado, R. L. Rodríguez-Suárez, A. Azevedo and S. M. Rezende, *Phys. Rev. B* **89**, 140406 (2014).

[143] X. Zhou, L. Ma, Z. Shi, W. J. Fan, J. G. Zheng, R. F. L. Evans and S.M. Zhou, *Phys. Rev. B* **92**, 060402(R) (2015).

[144] P. Wadley, B. Howells, J. Železný, C. Andrews, V. Hills, R.P. Campion, V. Novak, K. Olejník, F. Maccherozzi, S. S. Dhesi, S. Y. Martin, T. Wagner, J. Wunderlich, F. Freimuth, Y. Mokrousov, J. Kuneš, J. S. Chauhan, M. J. Grzybowski, A. W. Rush-forth, K. W. Edmonds, B. L. Gallagher and T. Jungwirth, *Science* **351**, 587 (2016).

[145] A. V. D. Brink, G. Vermijs, A. Solignac, J. Koo, J. T. Kohlhepp, H. J. M. Swagten and B. Koopmans, *Nat. Commun.* **7**, 10854 (2016).

[146] V. Tshitoyan, C. Ciccarelli, A. P. Mihai, M. Ali, A. C. Irvine, T. A. Moore, T. Jungwirth and A. J. Ferguson, *Phys. Rev. B* **92**, 214406 (2015).

[147] T. Okuno, D.-H. Kim, S.-H. Oh, S. K. Kim, Y. Hirata, T. Nishimura, W. S. Ham, Y. Futakawa, H. Yoshikawa, A. Tsukamoto, Y. Tserkovnyak, Y. Shiota, T. Moriyama, K.-J. Kim, K.-J. Lee and T. Ono, *Nat. Electronics* **2**, 9 (2019).

[148] I. Dzyaloshinskii, *J. Phys. Chem. Solids* 4, 241 (1958).

[149] T. Moriya, *Phys. Rev.* 120, 91 (1960).

[150] A. Fert, V. Cros and J. Sampaio, *Nat. Nanotech.* **8**, 152 (2013).

[151] T. H. R. Skyrme, *Proc. Royal Soc. London A: Math. Phys. Eng. Sci.* **247**, 260 (1958); *ibid.* **252**, 236 (1959); *ibid.* **260**, 127 (1961); *ibid.* **262**, 237 (1961).

[152] S. Mühlbauer, B. Binz, F. Jonietz, C. Pfleiderer, A. Rosch, A. Neubauer, R. Georgii and P. Böni, *Science* **323**, 915 (2009).

[153] A. V. Chumak, V. I. Vasyuchka, A. A. Serga and B. Hillebrands, *Nat. Phys.* **11**, 453 (2015).

[154] T. Nagase, M. Komatsu, Y. G. So, T. Ishida, H. Yoshida, Y. Kawaguchi, Y. Tanaka, K. Saitoh, N. Ikarashi, M. Kuwahara and M. Nagao, *Phys Rev. Lett.* **123**, 137203 (2019).

[155] N. Romming, A. Kubetzka, C. Hanneken, K. von Bergmann and R. Wiesendanger, *Phys. Rev. Lett.* **114**, 177203 (2015).

[156] C. L. Kane and E. J. Mele, *Phys. Rev. Lett.* **95**, 146802 (2005); *ibid.* **95**, 226801 (2005).

[157] B. A. Bernevig and S.-C. Zhang, *Phys. Rev. Lett.* **96**, 106802 (2006).

[158] L. Fu, C. L. Kane and E. J. Mele, *Phys. Rev. Lett.* **98**, 106803 (2007).

[159] L. Fu and C. L. Kane, *Phys. Rev. B* **76**, 045302 (2007).

[160] D. Hsieh, D. Qian, L. Wray, Y. Xia, Y. S. Hor, R. J. Cava and M. Z. Hasan, *Nature* **452**, 970 (2008).

[161] Y. Xia, D. Qian, D. Hsieh, L. Wray, A. Pal, H. Lin, A. Bansil, D. Grauer, Y. S. Hor, R. J. Cava and M. Z. Hasan, *Nat. Phys.* **398**, 5 (2009).

[162] Y. L. Chen, J. G. Analytis, J.-H. Chu, Z. K. Liu, S.-K. Mo, X. L. Qi, H. J. Zhang, D. H. Lu, X. Dai, Z. Fang, S. C. Zhang, I. R. Fisher, Z. Hussain and Z.-X. Shen, *Science* **178**, 325 (2009).

[163] T. Sato, K. Segawa, H. Guo, K. Sugawara, S. Souma, T. Takahashi and Y. Ando, *Phys. Rev. Lett.* **105**, 136802 (2010).

[164] K. Kuroda, M. Ye, A. Kimura, S. V. Eremeev, E. E. Krasovskii, E. V. Chulkov, Y. Ueda, K. Miyamoto, T. Okuda, K. Shimada, H. Namatame and M. Taniguchi, *Phys. Rev. Lett.* **105**, 146801 (2010).

[165] Y. L. Chen, Z. K. Liu, J. G. Analytis, J.-H. Chu, H. J. Zhang, B. H. Yan, S.-K. Mo, R. G. Moore, D. H. Lu, I. R. Fisher, S. C. Zhang, Z. Hussain and Z.-X. Shen, *Phys. Rev. Lett.* **105**, 266401 (2010).

[166] B. Scharf, A. Matos-Abiague, J. E. Han, E. M. Hankiewicz and I. Žutić, *Phys. Rev. Lett.* **117**, 166806 (2016).

[167] K. Yasuda, R. Wakatsuki, T. Morimoto, R. Yoshimi, A. Tsukazaki, K. S. Takahashi, M. Ezawa, M. Kawasaki, N. Nagaosa and Y. Tokura, *Nat. Phys.* **12**, 555 (2016).

[168] N. H. D. Khang, Y. Ueda and P. N. Hai, *Nat. Mater.* **17**, 808 (2018).

[169] H. Ohno, D. Chiba, F. Matsukura, T. Omiya, E. Abe, T. Dietl, Y. Ohno and K. Ohtani, *Nature* **408**, 944 (2000).

[170] J. Nitta, T. Akazaki, H. Takayanagi and T. Enoki, *Phys. Rev. Lett.* **78**, 1335 (1997).

[171] H. C. Koo, J. H. Kwon, J. Eom, J. Chang, S. H. Han and M. Johnson, *Science* **325**, 1515 (2009).

[172] M. Weisheit, S. Fähler1, A. Marty, Y. Souche, C. Poinsignon, D. Givord, *Science* **315**, 349 (2007).

[173] D. Chiba, S. Fukami, K. Shimamura, N. Ishiwata, K. Kobayashi and T. Ono, *Nat. Mater.* **10**, 853 (2011).

[174] H. K. D. Kim, L. T. Schelhas, S. Keller, J. L. Hockel, S. H. Tolbert and G. P. Carman, *Nano Lett.* **13**, 884 (2013).

[175] T. Nozaki, A. Kozioł-Rachwał, M. Tsujikawa, Y. Shiota, X. Xu, T. Ohkubo, T. Tsukahara, S. Miwa, M. Suzuki, S. Tamaru, H. Kubota, A. Fukushima, K. Hono, M. Shirai, Y. Suzuki and S. Yuasa, *NPG Asia Materials* **9**, e451 (2017).

[176] L. Herrera Diez, Y. T. Liu, D. A. Gilbert, M. Belmeguenai, J. Vogel, S. Pizzini, E. Martinez, A. Lamperti, J. B. Mohammedi, A. Laborieux, Y. Roussigné, A. J. Grutter, E. Arenholtz, P. Quarterman, B. Maranville, S. Ono, M. Salah El Hadri, R. Tolley, E. E. Fullerton, L. Sanchez-Tejerina, A. Stashkevich, S. M. Chérif, A. D. Kent, D. Querlioz, J. Langer, B. Ocker and D. Ravelosona, *Phys. Rev. Appl.* **12**, 034005 (2019).

[177] K. Shimamura, D. Chiba, S. Ono, S. Fukami, N. Ishiwata, M. Kawaguchi, K. Kobayashi, and T. Ono, *Appl. Phys. Lett.* **100**, 122402 (2012).

[178] M. W. J. Prins, H. van Kempen, H. van Leuken, R. A. de Groot, W. van Roy and J. de Boeck, *J. Phys.: Condens. Matter* **7**, 9447 (1995).

[179] K. Nakajima, S. N. Okuno and K. Inomata, *Jpn. J. Appl. Phys.* **37**, L919 (1998).

[180] K. Sueoka, K. Mukasa, and K. Hayakawa, *Jpn. J. Appl. Phys.* **32**, 2989 (1993).

[181] J. A. C. Bland, S. J. Steinmüller, A. Hirohata and T. Taniyama, "Optical Studies of Electron Spin Transmission," in *Ultrathin Magnetic Structures IV*, B. Heinrich and J. A. C. Bland (*Eds.*) (Springer, Berlin, 2005) p. 59.

[182] A. F. Isakovic, D. M. Carr, J. Strand, B. D. Schultz, C. J. Palmstrøm and P. A. Crowell, *Phys. Rev. B* **64**, R161304 (2001).

[183] E. Beaurepaire, J.-C. Merle, A. Daunois and J.-Y. Bigot, *Phys. Rev. Lett.* **76**, 4250 (1996).

[184] C-H. Lambert, S. Mangin, B. S. D. Ch. S. Varaprasad, Y. K. Takahashi, M. Hehn, M. Cinchetti, G. Malinowski, K. Hono, Y. Fainman, M. Aeschlimann and E. E. Fullerton, *Science* **345**, 1337 (2014).

[185] J. Feldmann, N. Youngblood, D. Wright, H. Bhaskaran and W. H. P. Pernice, *Nature* **569**, 208 (2019).

[186] T. Kampfrath, M. Battiato, P. Maldonado, G. Eilers, J. Nötzold, S. Mährlein, V. Zbarsky, F. Freimuth, Y. Mokrousov, S. Blügel, M. Wolf, I. Radu, P. M. Oppeneer and M. Münzenberg, *Nat. Nanotechnol.* **8**, 256 (2013).

[187] T. Kampfrath, M. Battiato, P. Maldonado, G. Eilers, J. Nötzold, S. Mährlein, V. Zbarsky, F. Freimuth, Y. Mokrousov, S. Blügel, M. Wolf, I. Radu, P. M. Oppeneer amd M. Münzenberg, *Nat. Nano* **8**, 256 (2013).

[188] G. Torosyan, S. Keller, L. Scheuer, R. Beigang and E. Th. Papaioannou, *Sci. Rep.* **8**, 1311 (2018).

[189] S. Iihama, Y. Xu, M. Web, G. Malinowski, M. Hehn, J. Gorchon, E. E. Fullerton and S. Mangin, *Adv. Mater.* **30**, 1804004 (2018).

[190] C. D. Staciu, F. Hansteen, A. V. Kimel, A. Kirilyuk, A. Tsukamoto, A. Itoh and T. Rasing, *Phys. Rev. Lett.* **99**, 047601 (2007).

[191] Y. Tserkovnyak, A. Brataas and G. E. W. Bauer, *Phys. Rev. Lett.* **88**, 117601 (2002).

[192] E. Saitoh, M. Uchida, H. Miyajima and G. Tatara, *Appl. Phys. Lett.* **88**, 182509 (2006).

[193] C. Bell, S. Milikisyants, M. Huber and J. Aarts, *Phys. Rev. Lett.* **100**, 047002 (2008).

[194] S. Mizukami, Y. Ando and T. Miyazaki, *Phys. Rev. B* **66**, 104413 (2002).

[195] M. Oogane, T. Kubota, H. Naganuma and Y. Ando, *J. Phys. D: Appl. Phys.* **48**, 164012 (2015).

[196] C. Sterwerf, S. Paul, B. Khodadadi, M. Meinert, J.-M. Schmalhorst, M. Buchmeier, C. K. A. Mewes, T. Mewes and G. Reiss, *J. Appl. Phys.* **120**, 083904 (2016).

[197] C. Guillemard, S. Petit-Watelot, L. Pasquier, D. Pierre, J. Ghanbaja, J. C. Rojas-Sánchez, A. Bataille, J. Rault, P. Le Fèvre, F. Bertran and S. Andrieu, *Phys. Rev. Appl.* **11**, 064009 (2019).

[198] O. Boulle, V. Cros, J. Groller, L. G. Pereira, C. Deranlot, F. Petroff, G. Faini, J. Barnaś and A. Fert, *Nat. Phys.* **3**, 492 (2007).

[199] H. Kubota, A. Fukushima, K. Yakushiji, T. Nagahama, S. Yuasa, K. Ando, H. Maehara, Y. Nagamine, K. Tsunekawa, D. D. Djayaprawira, N. Watanabe and Y. Suzuki, *Nat. Phys.* **4**, 37 (2008).

[200] A. M. Deac, A. Fukushima, H. Kubota, H. Maehara, Y. Suzuki, S. Yuasa, Y. Nagamine, K. Tsunekawa, D. D. Djayaprawira and N. Watanabe, *Nat. Phys.* **4**, 803 (2008).

[201] V. S. Pribiag, I. N. Krivorotov, G. D. Fuchs, P. M. Braganca, O. Ozatay, J. C. Sankey, D. C. Ralph and R. A. Buhrman, *Nat. Phys.* **3**, 498 (2007).

[202] K. Yamada, S. Kasai, Y. Nakatani, K. Kobayashi, H. Kohno, A. Thiaville and T. Ono, *Nat. Mater.* **6**, 269 (2007).

[203] T. J. Silva and W. H. Rippard, *J. Magn. Magn. Mater.* **320**, 1260 (2008).

[204] R. Ramaswamy, J. M. Lee, K. Cai and H. Yang, *Appl. Phys. Rev.* **5**, 031107 (2018).

[205] A. Manchon, J. Železný, I. M. Miron, T. Jungwirth, J. Sinova, A. Thiaville, K. Garello and P. Gambardella, *Rev. Mod. Phys.* **91**, 035004 (2019).

[206] L. Liu, C.-F. Pai, D. C. Ralph and R. A. Buhrman, *Phys. Rev. Lett.* **109**, 186602 (2012).

[207] V. E. Demidov, S. Urazhdin, H. Ulrichs, V. Tiberkevich, A. Slavin, D. Baither, G. Schmitz and S. O. Demokritov, *Nat. Mater.* **11**, 1028 (2012).

[208] V. E. Demidov, H. Ulrichs, S. V. Gurevich, S. O. Demokritov, V. S. Tiberkevich, A. N. Slavin, A. Zholud and S. Urazhdin, *Nat. Commun.* **5**, 3179 (2014).

[209] R. H. Liu, W. L. Lim and S. Urazhdin, *Phys. Rev. Lett.* **110**,147601 (2013).

[210] M. Collet, X. de Milly, O. d'Allivy Kelly, V. V. Naletov, R. Bernard, P. Bortolotti, J. Ben Youssef, V. E. Demidov, S. O. Demokritov, J. L. Prieto, M. Muñoz, V. Cros, A. Anane, G. de Loubens and O. Klein, *Nat. Commun.* **7**, 10377 (2016).

[211] R. Ramaswamy, T. Dutta, S. Liang, G. Yang, M. S. M. Saifullah and H. Yang, *J. Phys. D: Appl. Phys.* **52**, 224001 (2019).

[212] R. Lebrun, A. Ross, S. A. Bender, A. Qaiumzadeh, L. Baldrati, J. Cramer, A. Brataas, R. A. Duine and M. Kläui, *Nature* **561**, 222 (2018).

[213] Q. Wang, M. Kewenig, M. Schneider, R. Verba, B. Heinz, M. Geilen, M. Mohseni, B. Lägel, F. Ciubotaru, C. Adelmann, C. Dubs, P. Pirro, T. Brächer, and A. V. Chumak arXiv:1905.12353.

[214] Q. Wang, B. Heinz, R. Verba, M. Kewenig, P. Pirro, M. Schneider, T. Meyer, B. Lägel, C. Dubs, T. Brächer and A. V. Chumak, *Phys. Rev. Lett.* **122**, 247202 (2019).

[215] S. O. Demokritov, V. E. Demidov, O. Dzyapko, G. A. Melkov, A. A. Serga, B. Hillebrands and A. N Slavin, *Nature* **443**, 430 (7110).

[216] B. Heinz, T. Brächer, M. Schneider, Q. Wang, B. Lägel, A. M. Friedel, D. Breitbach, S. Steinert, T. Meyer, M. Kewenig, C. Dubs, P. Pirro and A. V. Chumak, arXiv:1910.08801.

[217] T. Brächer, P. Pirro, and B. Hillebrands, *Phys. Rep.* **699**, 1 (2017).

[218] A. Khitun, M. Bao and K. L. Wang, *J. Phys. D: Appl. Phys.* **43,** 264005 (2010).

[219] S. Klingler, P. Pirro, T. Brächer, B. Leven, B. Hillebrands and A. V. Chumak, *Appl. Phys. Lett.* **105,** 152410 (2014).

[220] T. Schneider, A. A. Serga, B. Leven, B. Hillebrands, R. L. Stamps and M. P. Kostylev, *Appl. Phys. Lett.* **92**, 022505 (2008).

[221] A. Chumak, A. Serga and B. Hillebrands, *Nat. Commun.* **5**, 4700 (2014).

[222] A. J. E. Kreil, A. Pomyalov, V. S. L'vov, H. Yu. Musiienko-Shmarova, G. A. Melkov, A. A. Serga and B. Hillebrands, arXiv:1911.07802.

[223] J. S. Moodera and R. H. Meservey, "Spin-polarized tunnelling Magnetoelectronics," in *Magnetoelectronics* M. Johnson (*Ed.*) (Elsevier, Amsterdam, 2004) pp. 163-204.

[224] T. Kasuya and A. Yanase, *Rev. Mod. Phys.* **40**, 684 (1968).

[225] P. V. Radovanovic and D. R. Gamelin, *Phys. Rev. Lett.* **91**, 157202 (2003).

[226] P. LeClair, J. K. Ha, H. J. M. Swagten, J. T. Kohlhepp, C. H. van de Vin and W. J. M. de Jonge, *Appl. Phys. Lett.* **80**, 625 (2002).

[227] H. Sukegawa, J. P. Hadorn, Z. Wen, T. Ohkubo, S. Mitani and K. Hono, *Appl. Phys. Lett.* **110**, 112403 (2017).

[228] H. Ohno, *Science* **281**, 951 (1998).

[229] Y. Ohno, D. K. Young, B. Beschoten, F. Matsukura, H. Ohno and D. D. Awschalom, *Nature* **402**, 790 (1999).

[230] M. E. Flatté and J. M. Byers, *Phys. Rev. Lett.* **84**, 4220 (2000).

[231] R. Fiederling, M. Keim, G. Reuscher, W. Ossau, G. Schmidt, A. Waag and L. W. Molenkamp, *Nature* **402**, 787 (1999).

[232] J. M. Kikkawa and D. D. Awschalom, *Nature* **397**, 139 (1999).

[233] M. Oestreich, J. Hübner, D. Hägele, P. J. Klar, W. Heimbrodt, W. W. Rühle, D. E. Ashenford and B. Lunn, *Appl. Phys. Lett.* **74**, 1251 (1999).

[234] B. T. Jonker, Y. D. Park, B. R. Bennett, H. D. Cheong, G. Kioseoglou and A. Petrou, *Phys. Rev. B* **62**, 8180 (2000).

[235] B. T. Jonker, A. T. Hanbicki, Y. D. Park, G. Itskos, M. Furis, G. Kioseoglou, A. Petrou and X. Wei, *Appl. Phys. Lett.* **79**, 3098 (2001).

[236] I. Malajovich, J. M. Kikkawa, D. D. Awschalom, J. J. Berry and N. Samarth, *Phys. Rev. Lett.* **84**, 1015 (2000).

[237] Y. D. Park, A. T. Hanbicki, S. C. Erwin, C. S. Hellberg, J. M. Sullivan, J. E. Mattson, T. F. Ambrose, A. Wilson, G. Spanos and B. T. Jonker, *Science* **295**, 651 (2002).

[238] T. Dietl, H. Ohno, F. Matsukura, J. Cibert and D. Ferrand, *Science* **287**, 1019 (2000).

[239] G. E. W. Bauer, E. Saitoh and B. J. van Wees, *Nat. Mater.* **11**, 391 (2012).

[240] K. Uchida, S. Takahashi, K. Harii, J. Ieda, W. Koshibae, K. Ando, S. Maekawa and E. Saitoh, *Nature* **455**, 778 (2008).

[241] T. An, V. I. Vasyuchka, K. Uchida, A. V. Chumak, K. Yamaguchi, K. Harii, J. Ohe, M. B. Jungfleisch, Y. Kajiwara, H. Adachi, B. Hillebrands, S. Maekawa and E. Saitoh, *Nat. Mater.* **12**, 549 (2013).

[242] M. Mizuguchi and S. Nakatsuji, *Sci. Technol. Adv. Mater.* **20**, 262 (2019).

[243] K. Hasegawa, M. Mizuguchi, Y. Sakuraba, T. Kamada, T. Kojima, T. Kubota, S. Mizukami, T. Miyazaki and K. Takanashi, *Appl. Phys. Lett.* **106**, 252405 (2015).

[244] T Seki, R Iguchi, K Takanashi and K Uchida, *J. Phys. D: Appl. Phys.* **51**, 254001 (2018).

[245] Y. Imry, *Introduction to Mesoscopic Physics* (Oxford Univ. Press, Oxford, 1997).

[246] Y. Aharonov and D. Bohm, *Phys. Rev.* **115**, 485 (1959).

[247] B. L. Altshuler, A. G. Aronov and B. Z. Spivak, *JETP Lett.* **33**, 94 (1981).

[248] K. Sekiguchi, A. Yamaguchi, H. Miyajima and A. Hirohata, *Phys. Rev. B* **77**, 140401(R) (2008).

[249] D. Loss and P.M. Goldbart, *Phys. Rev. B* **45**, 13544 (1992).

[250] F. Nagasawa, D. Frustaglia, H. Saarikoski, K. Richter and J. Nitta, *Nat. Commun.* **4**, 2526 (2013).

[251] A. Hirohata, I. Sugai, M. Mizuguchi, K. Takanashi and S. N. Holmes, *4th Int'l. Workshop on Spin Currents and 2nd Int'l. Workshop on Spin Caloritronics* (09/02/2010, Sendai, Japan).

[252] M. Matsuo, J. Ieda, E. Saitoh and S. Maekawa, *Phys. Rev. Lett.* **106**, 076601 (2011).

[253] S. J. Barnett, *Phys. Rev.* **6**, 239 (1915).

[254] S. J. Barnett, *Rev. Mod. Phys.* **7**, 129 (1935).

[255] M. Matsuo, J. Ieda, E. Saitoh and S. Maekawa, *Appl. Phys. Lett.* **98**, 242501 (2011).

[256] A. Hirohata, Y. Baba, B. A. Murphy, B. Ng, Y. Yao, K. Nagao and J.-Y. Kim, *Sci. Rep.* **8**, 1974 (2018).

[257] H. Chudo, M. Ono, K. Harii, M. Matsuo, J. Ieda, R. Haruki, S. Okayasu, S. Maekawa, H. Yasuoka and E. Saitoh, *Appl. Phys. Exp.* **7**, 063004 (2014).

[258] D. Kobayashi, T. Yoshikawa, M. Matsuo, R. Iguchi, S. Maekawa, E. Saitoh and Y. Nozaki, *Phys. Rev. Lett.* **119**, 077202 (2017).

[259] R. Takahashi, M. Matsuo, M. Ono, K. Harii, H. Chudo, S. Okayasu, J. Ieda, S. Takahashi, S. Maekawa and E. Saitoh, *Nat. Phys.* **12**, 52 (2016).

[260] I. Galanakis and P. H. Dederichs (Eds.), *Half-Metallic Alloys* (Springer, Berlin, 2005).

[261] K. Elphick, W. Frost, M. Samiepour, T. Kubota, K. Takanashi, H. Sukegawa, S. Mitani and A. Hirohata, *Mater. Today* (submitted).

[262] K. Schwarz, *J. Phys. F* **16**, L211 (1986).

[263] A. Yamase and K. Shiratori, *J. Phys. Soc. Jpn.* **53**, 312 (1984).

[264] Y. Okimoto, T. Katsufuji, T. Ishikawa, A. Urushibara, T. Arima and Y. Tokura, *Phys. Rev. Lett.* **75**, 109 (1995).

[265] J. S. Moodera and R. H. Meservey, Spin-polarized tunneling. in *Magnetoelectronics* M. Johnson (Ed.) (Elsevier, Amsterdam, The Netherlands, 2004) pp. 163-204.

[266] H. Akinaga, T. Manago and M. Shirai, *Jpn. J. Appl. Phys.* **39**, L1118 (2000).

[267] R. A. de Groot, F. M. Mueller, P. G. van Engen and K. H. J. Buschow, *Phys. Rev. Lett.* **50**, 2024 (1983).

[268] R. J. Soulen, Jr., J. M. Byers, M. S. Osofsky, B. Nadgorny, T. Ambrose, S. F. Cheng, P. R. Broussard, C. T. Tanaka, J. Nowak, J. S. Moodera, A. Barry and J. M. D. Coey, *Science* **282**, 85 (1998).

[269] T. Dietl, H. Ohno, F. Matsukura, J. Cibert and D. Ferrand, *Science* **287**, 1019 (2000).

[270] I. Galanakis, Theory of Heusler and full-Heusler compounds. in *Heusler Alloys* C. Felser and A. Hirohata (Eds.) (Springer, Berlin, Germany, 2016) pp. 3-36.

[271] A. Hirohata, M. Kikuchi, N. Tezuka, K. Inomata, J. S. Claydon, Y. B. Xu, G. van der Laan, *Curr. Opin. Solid State Mater. Sci.* **10**, 93 (2006).

[272] A. Hirohata, H. Sukegawa, H. Yanagihara, I. Žutić, T. Seki, S. Mizukami and R. Swaminathan, *IEEE Trans. Magn.* **51**, 0800511 (2015).

[273] J. W. Jung, Y. Sakuraba, T. T. Sasaki, Y. Miura and K. Hono, *Appl. Phys. Lett.* **108**, 102408 (2016).

[274] A. Hirohata, W. Frost, M. Samiepour and J.-Y. Kim, *Materials* **11**, 105 (2018).

[275] V. Kambersky, Can. *J. Phys.* **48**, 2906 (1970).

[276] M. Oogane, T. Wakitani, S. Yakata, R. Yilgin, Y. Ando, A. Sakuma and T. Miyazaki, *Jpn. J. Appl. Phys.* **45**, 3889 (2006).

[277] M. van Kampen, C. Jozsa, J. T. Kohlhepp, P. LeClair, L. Lagae, W. J. M. Jonge and B. Koopmans, *Phys. Rev. Lett.* **88**, 227201 (2002).

[278] Z. Bai, L. Shen, G. Han and Y. Feng, *Spin* **2**, 1230006 (2012).

[279] A. Conca, A. Niesen, G. Reiss and B. Hillebrands, *AIP Adv.* **9**, 085205 (2019).

[280] A. Hirohata, W. Frost, M. Samiepour and J.-Y. Kim, *Materials* **11**, 105 (2018).

[281] D. M. Lattery, D. Zhang, J. Zhu, X. Hang, J.-P. Wang and X. Wang, *Sci Rep.* **8**, 13395 (2018).

[282] A. Manchon, C. Ducruet, L. Lombard, S. Auffret, B. Rodmacq, B. Dieny, S. Pizzini, J. Vogel, V. Uhlíř, M. Hochstrasser and G. Panaccione, *J. Appl. Phys.* **104**, 043914 (2008).

[283] S. Monso, B. Rodmacq, S. Auffret, G. Casali, F. Fettar, B. Gilles, B. Dieny and P. Boyer, *Appl. Phys. Lett.* **80**, 4157 (2002).

[284] B. Rodmacq and B. Dieny, *US Patent* 7,813,202B2 (2006); *US Patent* 8,247,093 B2 (2006).

[285] B. Rodmacq, S. Auffret, B. Dieny and L. E. Nistor, *US Patent* 8,513,944B2 (2008).

[286] H. Sato, T. Yamamoto, M. Yamanouchi, S. Ikeda, S. Fukami, K. Kinoshita, F. Matsukura, N. Kasai and H. Ohno, “Comprehensive study of CoFeB-MgO magnetic tunnel junction characteristics with single- and double-interface scaling down to 1X nm,” *Proc. Int’l Elec. Dev. Meeting (IEDM)* 33.2.1 (2014).

[287] K. Nishioka, et al., "Novel Quad interface MTJ technology and its first demonstration with high thermal stability and switching efficiency for STT-MRAM beyond 2Xnm," *Symp. VLSI Technol.* T120 (2019).

[288] Z. Wen, H. Sukegawa, T. Furubayashi, J. Koo, K. Inomata, S. Mitani, J. P. Hadorn, T. Ohkubo and K. Hono, *Adv. Mater.* **26**, 6483 (2014).

[289] T. Hiratsuka, G. Kim, Y. Sakuraba, T. Kubota, K. Kodama, N. Inami, H. Naganuma, M. Oogane, T. Nakamura, K. Takanashi and Y. Ando, *J. Appl. Phys.* **107**, 09C714 (2010).

[290] W. Frost, M. Samiepour and A. Hirohata, *J. Magn. Magn. Mater.* **484**, 100 (2019).

[291] A. Hirohata, T. Huminiuc, J. Sinclair, H. Wu, M. Samiepour, G. Vallejo-Fernandez, K. O'Grady, J. Balluf, M. Meinert, G. Reiss, E. Simon, S. Khmelevskyi, L. Szunyogh, R. Yanes Díaz, U. Nowak, T. Tsuchiya, T. Sugiyama, T. Kubota, K. Takanashi, N. Inami and K. Ono, *J. Phys. D: Appl. Phys.* **50**, 443001 (2017).

[292] A. Hirohata, M. Kikuchi, N. Tezuka, K. Inomata, J. S. Claydon, Y. B. Xu and G. van der Laan, *Curr. Opin. Solid State Mater. Sci.* **10**, 93 (2006).

[293] A. K. Nayak, M. Nicklas, S. Chadov, P. Khuntia, C. Shekhar, A. Kalache, M. Baenitz, Y. Skourski, V. K. Guduru, A. Puri, U. Zeitler, J. M. D. Coey and C. Felser, *Nat. Mater.* **14**, 679 (2015).

[294] E. Krén and G. Kádár, *Solid State Commun.* **8**, 1653 (1970).

[295] H. Kurt, K. Rode, H. Tokuc, P. Stamenov, M. Venkatesan and J. M. D. Coey, *Appl. Phys. Lett.* **101**, 232402 (2012).

[296] H. Wu, I. Sudoh, R. Xu, W. Si, C. A. F. Vaz, J.-Y. Kim, G. Vallejo-Fernandez and A. Hirohata, *J. Phys. D: Appl. Phys.* **51**, 215003 (2018).

[297] J. Balluff, M. Meinert, J.-M. Schmalhorst, G. Reiss and E. Arenholz, *J. Appl. Phys.* **118**, 243907 (2016).

[298] Y. S. Hor, P. Roushan, H. Beidenkopf, J. Seo, D. Qu, J. G. Checkelsky, L. A. Wray, D. Hsieh, Y. Xia, S.-Y. Xu, D. Qian, M. Z. Hasan, N. P. Ong, A. Yazdani and R. J. Cava, *Phys. Rev. B* **81**, 195203 (2010).

[299] J. G. Checkelsky, J. Ye, Y. Onose, Y. Iwasa and Y. Tokura, *Nat. Phys.* **8**, 729 (2012).

[300] V. M. Edelstein, *Solid State Commun.* **73**, 233 (1990).

[301] C. H. Li, O. M. J. van‘t Erve, J. T. Robinson, Y. Liu, L. Li and B. T. Jonker, *Nat. Nanotechnol.* **9**, 218 (2014).

[302] A. R. Mellnik, J. S. Lee, A. Richardella, J. L. Grab, P. J. Mintun, M. H. Fischer, A. Vaezi, A. Manchon, E.-A. Kim, N. Samarth, D. C. Ralph, *Nature* **511**, 449 (2014).

[303] Y. Shiomi, K. Nomura, Y. Kajiwara, K. Eto, M. Novak, K. Segawa, Y. Ando and E. Saitoh, *Phys .Rev. Lett.* **113**, 196601 (2014).

[304] Y. Fan, P. Upadhyaya, X. Kou, M. Lang, S. Takei, Z. Wang, J. Tang, L. He, L.-T. Chang, M. Montazeri, G. Yu, W. Jiang, T. Nie, R. N. Schwartz, Y. Tserkovnyak and K. L. Wang, *Nat. Mater.* **13**, 699 (2014).

[305] J. Sinova and Igor Žutić, *Nat. Mater.* **11**, 368 (2012).

[306] S. Mao, Y. Chen, F. Liu, X. Chen, B. Xu, P. Lu, M. Patwari, H. Xi, C. Chang, B. Miller, D. Menard, B. Pant, J. Loven, K. Duxstad, S. Li, Z. Zhang, A. Johnston, R. Lamberton,

M. Gubbins, T. McLaughlin, J. Gadbois, J. Ding, B. Cross, S. Xue and P. Ryan, *IEEE Trans. Magn.* **42**, 97 (2006).

[307] M. Takagishi, K. Yamada, H. Iwasaki, H. N. Fuke and S. Hashimoto, *IEEE Trans. Magn.* **46**, 2086 (2010).

[308] H. N. Fuke, S. Hashimoto, M. Takagishi, H. Iwasaki, S. Kawasaki, K. Miyake and M. Sahashi, *IEEE Trans. Magn.* **43**, 2848 (2007).

[309] H. J. Richter, *J. Phys. D: Appl. Phys.* **40**, R149 (2007).

[310] H. Katayama, S. Sawamura, Y. Ogimoto, J. Nakajima, K. Kojima and K. Ohta, *J. Magn. Soc. Jpn.* **23**, 233 (1999).

[311] R. Rottmayer, S. Batra, D. Buechel, W. A. Challener, J. Hohlfeld, Y. Kubotam L. Li, B. Lu, C. Mihalcea, K. Mountfield, K. Pelhos, C. Peng, T. Rausch, M. A. Seigler, D. Weller and X.-M. Yang, *IEEE Trans. Magn.* **42**, 2417 (2006).

[312] M. A. Seigler, W. A. Challener, E. Gage, N. Gokemeijer, G. Ju, B. Lu, K. Pelhos, C. Peng, R. E. Rottmayer, X. Yang, H. Zhou and T. Rausch, *IEEE Trans. Magn.* **44**, 119 (2008).

[313] G. Ju, Y. Peng, E. K. C. Chang, Y. Ding, A. Q. Wu, X. Zhu, Y. Kubota, T. J. Klemmer, H. Amini, L. Gao, Z. Fan, T. Rausch, P. Subedi, M. Ma, S. Kalarickal, C. J. Rea, D. V. Dimitrov, P.-W. Huang, K. Wang, X. Chen, C. Peng, W. Chen, J. W. Dykes, M. A. Seigler, E. C. Gage, R. Chantrell, J.-U. Thiele *IEEE Tran. Magn.* **51**, 3201709 (2015).

[314] J.-G, Zhu and Y. Tang, *IEEE Trans. Magn.* **44**, 125 (2008).

[315] T. Seki, K. Utsumiya, Y. Nozaki, H. Imamura and K. Takanashi, *Nat. Commun.* **4**, 1726 (2013).

[316] http://technology.ihs.com/

[317] http://www.yole.fr/

[318] S. Baillet, *Nat. Neurosci.* **20**, 327 (2017).

[319] K. Fujiwara, M. Oogane, A. Kanno, M. Imada, J. Jono, T. Terauchi, T. Okuno, Y. Aritomi, M. Morikawa, M. Tsuchida, *App. Phys. Exp.* **11**, 023001 (2018).

[320] L. J. Schwee, *IEEE Trans. Magn.* **8**, 405 (1972).

[321] G. B. Granley, J. M. Daughton, A. V. Pohm and C. S. Comstock, *IEEE Trans. Magn.* **27**, 5517 (1991).

[322] Z. G. Wang and Y. Nakamura, *IEEE Trans. Magn.* **32**, 4022 (1996)., J. M. Daughton, *J. Appl. Phys.* **81**, 3758 (1997).

[323] R. E. Scheunerlein, W. Gallagher, S. S. P. Parkin, A. Lee, S. Ray, R. Robertazzi and W. Reohr, *IEEE Int. Solid-State Circuits Conf. (ISSCC)*, Digest of Technical Papers p. 128 (2000).

[324] M. Durlan, P. Naji, M. DeHerrera, S. Tehrani, G. Kerszykowski and K. Kyler, *IEEE Int. Solid-State Circuits Conf. (ISSCC)*, Digest of Technical Papers p. 130 (2000).

[325] M. Durlam, D. Addie, J. Åkerman, B. Butcher, P. Brown, J. Chan, M. DeHerrera, B. N. Engel, B. Feil, G. Grynkewich, J. Janesky, M. Johnson, K. Kyler, J. Molla, J. Martin, K. Nagel, J. Ren, N. D. Rizzo, T. Rodgiguez, L. Savtchenko, J. Salter, J. M. Slaughter, K. Smith, J. J. Sun, M. Lien, K. Papworth, P. Shah, W. Qin, R. Williams, L. Wise and S. Tehrani, *Int. Electron Devices Meeting (IEDM)*, Technical Digest p. 995 (2003).

[326] B. N. Engel, J. Åkerman, B. Butcher, R. W. Dave, M. DeHerrea, M. Durlam, G. Grynkewich, J. Janesky, S. V. Pietambaram, N. D. Rizzo, J. M. Slaughter, K. Smith, J. J. Sun and S. Tehrani, *IEEE Trans. Magn.* **41**, 132 (2005).

[327] Y. Iwata, K. Tsuchida, T. Inaba, Y. Shimizu, R. Takizawa, Y. Ueda, T. Sugibayashi, Y. Asao, T. Kajiyama, K. Hosotani, S. Ikegawa, T. Kai, M. Nakayama, S. Tahara and H. Yoda, *IEEE Int. Solid-State Circuits Conf. (ISSCC)*, Digest of. Technical Papers p. 477 (2006).

[328] J. DeBrosse, D. Gogl, A. Bette, H. Hoenigschmid, R. Robertazzi, C. Arndt, D. Braun, D. Casarotto, R. Havreluk, S. Lammers, W. Obermaier, W. R. Reohr, H. Viehmann, W. J. Gallagher and G. Müller, *IEEE J. Solid-State Circ.* **39**, 678 (2004).

[329] M. Hosomi, H. Yamagishi, T. Yamamoto, K. Bessho, Y. Higo, K. Yamane, H. Yamada, M. Shoji, H. Hachino, C. Fukumoto, H. Nagao and H. Kano, *Int. Electron Devices Meeting (IEDM)*, Tech. Dig. p. 459 (2005).

[330] http://www.ewh.ieee.org/r6/scv/mag/MtgSum/Meeting2012_05_Presentation.pdf.

[331] G. Schmidt, D. Ferrand, L. W. Molenkamp, A. T. Filip and B. J. van Wees, *Phys. Rev. B* **62**, 4790(R) (2000).

[332] Y. Nagamine, H. Maehara, K. Tsunekawa, D. D. Djayaprawira and N. Watanabe, *Appl. Phys. Lett.* **89**, 162507 (2006).

[333] S. Ikeda, K. Miura, H. Yamamoto, K. Mizunuma, H. D. Gan, M. Endo, S. Kanai, J. Hayakawa, F. Matsukura and H. Ohno, *Nat. Mater.* **9**, 721 (2010).

[334] https://www.everspin.com/news/everspin-256mb-st-mram-perpendicular-mtj-sampling.

[335] https://news.samsung.com/global/samsung-electronics-starts-commercial-shipment-of-emram-product-based-on-28nm-fd-soi-process.

[336] I. M. Miron, K. Garello, G. Gaudin, P.-J. Zermatten, M. V. Costache, S. Auffret, S. Bandiera, B. Rodmacq, A. Schuhl and P. Gambardella, *Nature* **476**, 189 (2011).

[337] K. Garello, F. Yasin, S. Couet, L. Souriau, J. Swerts, S. Rao, S. Van Beek, W. Kim, E. Liu, S. Kundu, D. Tsvetanova, K. Croes, N. Jossart, E. Grimaldi, M. Baumgartner, D. Crotti, A. Fumémont, P. Gambardella and G. S. Kar, “SOT-MRAM 300MM Integration

for Low Power and Ultrafast Embedded Memories," *IEEE Symp. VLSI Circuits* **2018**, 81 (2018).

[338] Y. Shiota, T. Nozaki, F. Bonell, S. Murakami, T. Shinjo and Y. Suzuki, *Nat. Mater.* **11**, 39 (2011).

[339] H. Yoda, N. Shimomura, Y. Ohsawa, S. Shirotori, Y. Kato, T. Inokuchi, Y. Kamiguchi, B. Altansargai, Y. Saito, K. Koi, H. Sugiyama, S. Oikawa, M. Shimizu, M. Ishikawa, K. Ikegami and A. Kurobe, "Voltage-control spintronics memory (VoCSM) having potentials of ultra-low energyconsumption and high-density," *Proc. 2016 IEEE Int'l Elec. Dev. Meeting (IEDM)* 3-7 Dec. (2016).

[340] S. I. Kiselev, J. C. Sankey, I. N. Krivorotov, N. C. Emley, R. J. Schoelkopf, R. A. Buhrman and D. C. Ralph, *Nature* **425**, 380 (2003).

[341] T. Silva and W. Rippard, *J. Magn. Magn. Mater.* **320**, 1260 (2010).

[342] A. M. Deac, A. Fukushima, H. Kubota, H. Maehara, Y. Suzuki, S. Yuasa, Y. Nagamine, K. Tsunekawa, D. D. Djayaprawira and N. Watanabe, *Nat. Phys.* **4**, 803 (2008).

[343] W. H. Rippard, M. R. Pufall, S. Kaka, T. J. Silva and S. E. Russek, *Phys. Rev. B* **70**, 100406(R) (2004).

[344] H. Kubota, K. Yakushiji, A. Fukushima, S. Tamaru, M. Konoto, T. Nozaki, S. Ishibashi, T. Saruya, S. Yuasa, T. Taniguchi, H. Arai and H. Imamura, *Appl. Phys. Exp.* **6**, 103003 (2013).

[345] H. Maehara, H. Kubota, Y. Suzuki, T. Seki, K. Nishimura, Y. Nagamine, K. Tsunekawa, A. Fukushima, H. Arai, T. Taniguchi, H. Imamura, K. Ando and S. Yuasa, *Appl. Phys. Exp.* **7**, 023003 (2014).

[346] B. V. Benjamin, P. Gao, E. McQuinn, S. Choudhary, A. R. Chandrasekaran, J.-M. Bussat, R. Alvarez-Icasa, J. V. Arthur, P. A. Merolla and K. Boahen, *Proc. IEEE* **102**, 699 (2014).

[347] https://www.ibm.com/blogs/research/tag/truenorth/

[348] M. Davies, N. Srinivasa, T.-H. Lin, G. Chinya, Y. Cao, S. H. Choday, G. Dimou, P. Joshi, N. Imam, S. Jain, Y. Liao, C.-K. Lin, A. Lines, R. Liu, D. Mathaikutty, S. McCoy, A. Paul, J. Tse, G. Venkataramanan, Y.-H. Weng, A. Wild, Y. Yang and H. Wang, *IEEE Micro* **38**, 82 (2018).

[349] *HBP Neuromorphic Computing Platform Guidebook*, https://electronicvisions.github.io/hbp-sp9-guidebook/ (2019).

[350] S. B. Furber, F. Galluppi, S. Temple and L. A. Plana, *Proc. IEEE* **102**, 652 (2014).

[351] https://gdr-biocomp.fr/en/colloque-biocomp-2019/julie-grollier/

[352] W. A. Borders, H. Akima, S. Fukami, S. Moriya, S. Kurihara, Y. Horio, S. Sato and H. Ohno, *Appl. Phys. Exp.* **10**, 013007 (2016).

[353] S. Tsunegi, T. Taniguchi, R. Lebrun, K. Yakushiji, V. Cros, J. Grollier, A. Fukushima, S. Yuasa and H. Kubota, *Sci. Rep.* **8**, 13475 (2018).

[354] W. A. Borders, A. Z. Pervaiz, S. Fukami, K. Y. Camsari, H. Ohno and S. Datta, *Nature* **573**, 390 (2019).

[355] T. Devolder, D. Rontani, S. Petit-Watelot, K. Bouzehouane, S. Andrieu, J. Létang, M.-W. Yoo, J.-P. Adam, C. Chappert, S. Girod, V. Cros, M. Sciamanna and J.-V. Kim, arxiv.org/pdf/1903.00921

[356] S. S. P. Parkin, “Shiftable magnetic shift register and method of using the same,” *U. S. Patent* 6834005 (IBM, 10 June 2003); “System and method for writing to a magnetic shift register,” *U. S. Patent* 6898132 (IBM, 10 June 2003); “System and method for reading data stored on a magnetic shift register,” *U. S. Patent* 6920062 (IBM, 14 October 2003); “Magnetic shift register with shiftable magnetic domains between two regions, and method of using the same,” *U. S. Patent* 7031178 (IBM, 9 November 2004); “System and method for transfering data to an magnetic shift register with a shiftable data column,” *U. S. Patent* 7236386 (IBM, 4 December 2004).

[357] S. S. P. Parkin, K. P. Roche, M. G. Samant, P. M. Rice, R. B. Beyers, R. E. Scheuerlein, E. J. O’Sullivan, S. L. Brown, J. Bucchigano, D. W. Abraham, Y. Lu, M. Rooks, P. L. Trouillod, R. A. Wanner and W. J. Gallagher, *J. Appl. Phys.* **85**, 5828 (1999).

[358] M. Hayashi, L. Thomas, C. Rettner, R. Moriya, X. Jiang and S. S. P. Parkin, *Phys. Rev. Lett.* **97**, 207205 (2006).

[359] J. Grollier, P. Boulenc, V. Cros, A. Hamzić, A. Vaurès, A. Fert and G. Faini, *Appl. Phys. Lett.* **83**, 509 (2003).

[360] M. Tsoi, R. E. Fontana and S. S. P. Parkin, *Appl. Phys. Lett.* **83**, 2617 (2003).

[361] M. Yamanouchi, D. Chiba, F. Matsukura and H. Ohno, *Nature* **428**, 539 (2004).

[362] D. Chiba, F. Matsukura and H. Ohno, *Phys. Rev. Lett.* **96**, 096602 (2006).

[363] K. Yamada, S. Kasai, Y. Nakatani, K. Kobayashi and T. Ono, *Appl. Phys. Lett.* **93**, 152502 (2008).

[364] S. Kasai, K. Nakano, K. Kondou, N. Ohshima, K. Kobayashi and T. Ono, *Appl. Phys. Exp.* **1**, 091302 (2008).

[365] S. Fukami, T. Suzuki, K. Nagahara, N. Ohshima, Y. Ozaki, S. Saitoh, R. Nebashi, N. Sakimura, H. Hnjo, K. Mori, C. Igarashi, S. Miura, N. Ishiwata and T. Sugibayashi, *Symp. on VLSI Technol.* 12A-2 (Kyoto, Japan, 17 June 2009).

[366] S.-H. Yang, K.-S. Ryu and S. S. P. Parkin, *Nat. Nanotechnol.* **10**, 221 (2015).

[367] L. Thomas, M. Hayashi, X. Jiang, R. Moriya, C. Rettner and S. S. P. Parkin, *Nature* **443**, 197 (2006).

[368] L. Thomas, M. Hayashi, X. Jiang, R. Moriya, C. Rettner and S. S. P. Parkin, *Science* **315**, 1553 (2007).

[369] M. Hayashi, L. Thomas, C. Rettner, R. Moriya and S. S. P. Parkin, *Nat. Phys.* **3**, 21 (2007).

[370] E. R. Lewis, D. Petit, L. O'Brien, A. Fernandez-Pacheco, J. Sampaio, A-V. Jausovec, H. T. Zeng, D. E. Read and R. P. Cowburn, *Nat. Mater.* **9**, 980 (2010).

[371] I. Polenciuc, A. J. Vick, D. A. Allwood, T. J. Hayward, G. Vallejo-Fernandez, K. O'Grady and A. Hirohata, *Appl. Phys. Lett.* **105**, 162406 (2014).

[372] T. L. Jin et al., *Sci. Rep.* **7**, 16208 (2017).

[373] S. Mühlbauer, B. Binz, F. Jonietz, C. Pfleiderer, A. Rosch, A. Neubauer, R. Georgii and P. Böni, *Science* **320**, 915 (2008).

[374] J. Iwasaki, M. Mochizuki and N. Nagaosa, *Nat. Nanotech.* **8**, 742 (2013).

[375] W. Jiang, P. Upadhyaya, W. Zhang, G. Yu, M. B. Jungfleisch, F. Y. Fradin, J. E. Pearson, Y. Tserkovnyak, K. L. Wang, O. Heinonen, S. G. E. te Velthuis and A. Hoffmann, *Science* **349**, 283 (2015).

[376] S. Woo, K. Litzius, B. Krüger, M. Y. Im, L. Caretta, K. Richter, M. Mann, A. Krone, R. M. Reeve, M. Weigand, P. Agrawal, I. Lemesh, M. A. Mawass, P. Fischer, M. Kläui and G. S. Beach, *Nat. Mater.* **15**, 501 (2016).

[377] A. Hrabec, J. Sampaio, M. Belmeguenai, I. Gross, R. Weil, S. M. Chérif, A. Stashkevich, V. Jacques, A. Thiaville and S. Rohart, *Nat. Commun.* **8**, 15765 (2017).

[378] X. Zhang, M. Ezawa and Y. Zhou, *Sci. Rep.* **5**, 9400 (2015).

[379] Y. Nakatani, K. Yamada and A. Hirohata, *Sci. Rep.* **9**, 13475 (2019).

[380] P. A. M. Dirac, *The Principles of Quantum Mechanics* (Clarendon Press, Oxford, 1958).

[381] W. Y. Choi, H.-J. Kim, J. Chang, S. H. Han, H. C. Koo and M. Johnson, *Nat. Nanotechnol.* **10**, 666 (2015).

[382] B. A. Murphy, A. J. Vick, M. Samiepour and A. Hirohata, *Sci. Rep.* **6**, 37398 (2016).

[383] A. Hirohata and J.-Y. Kim, "Optically Induced and Detected Spin Current," in *Spin Current* (Second Edition), S. Maekawa, S. O. Valenzuela, E. Saitoh and T. Kimura (*Eds*) (Oxford University Press, Oxford, 2017), pp. 48-68.

[384] S. Hallstein, J. D. Berger, M. Hilpert, H. C. Schneider, W. W. Rühle, F. Jahnke, S. W. Koch, H. M. Gibbs, G. Khitrova and M. Oestreich, *Phys. Rev. B* **56**, R7076 (1997).

[385] J. Rudolph, S. Döhrmann, D. Hägele and M. Oestreich, *Appl. Phys. Lett.* **87**, 241117 (2005).

[386] C. Gothgen, R. Oszwaldowski, A. Petrou and I. Žutić, *Appl. Phys. Lett.* **93**, 042513 (2008).

[387] J. Lee, R. Oszwaldowski, C. Gøthgen and I. Žutić, *Phys. Rev. B* **85**, 045314 (2012).

[388] G. Boóris, J. Lee, K. Vyborny and I. Žutić, *Appl. Phys. Lett.* **100**, 121111 (2012).

[389] N. C. Gerhardt, M. Y. Li, H. Jähme, H. Höpfner, T. Ackermann and M. R. Hofmann, *Appl. Phys. Lett.* **99**, 151107 (2011).

[390] H. Susanto,1, K. Schires, M. J. Adams, and I. D. Henning, *Phys. Rev. A* **92**, 063838 (2015).

[391] J.-Y. Chen, T.-M. Wong, C.-W. Chang, C.-Y. Dong and Y.-F. Chen, *Nat. Nanotechnol.* **9**, 845 (2014).

The University of York

Atsufumi Hirohata, PhD
Department of Electronic Engineering
Heslington
York YO10 5DD
United Kingdom
Phone: +44 (0)1904 32 3245
Fax: +44 (0)1904 32 2335
Email: atsufumi.hirohata@york.ac.uk

Professor Marcelo Knobel
Editor-in-Chief
Journal of Magnetism and Magnetic Materials
State University of Campinas Institute of Physics
Gleb Wataghin, Rua Sérgio Buarque de Holanda 777
13.083-859 SP, Campinas, Brazil

27 January 2020

Dear Editors,

We wish to submit the original research article, “Review on Spintronics: Principles and Device Applications“ for your consideration for the publication in *Journal of Magnetism and Magnetic Materials*. We confirm that the work is original and has not been published, nor is under review, for publication elsewhere. We have no conflicts of interest to disclose for the submission of this article.

Yours sincerely,

Atsufumi Hirohata
Professor in Nanoelectronics

[392]

- Broad overview on eight major methods for spin generation is given with their physical principles.
- Corresponding device applications are discussed based on their recent development.
- Future perspectives on the spintronic devices are provided at the end of this review.

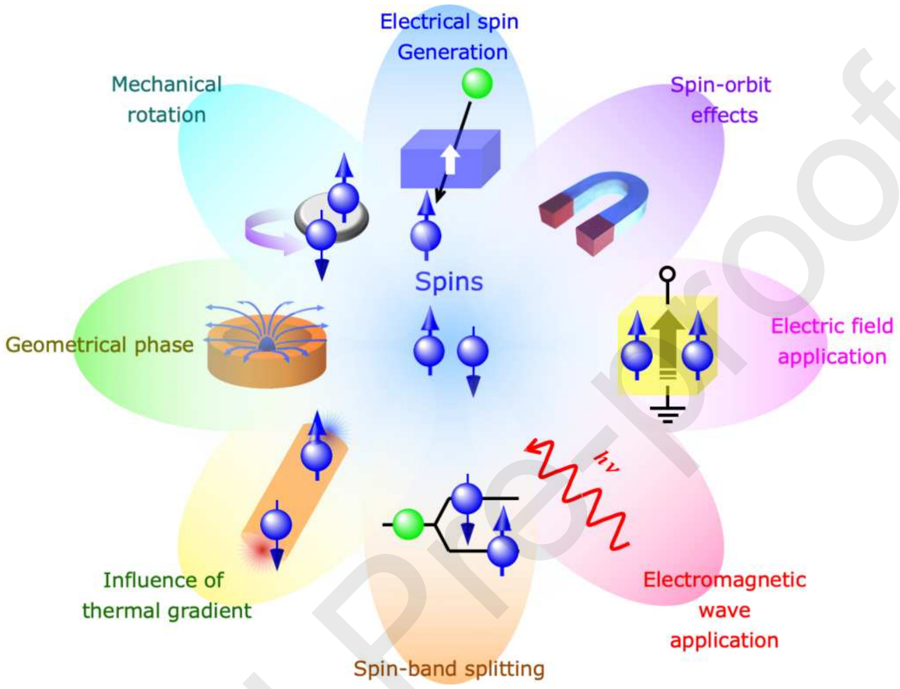

[393]